Charles University

Faculty of Science

Study department: Organic Chemistry

Mbilo Misehe, M.Sc.

Design, synthesis and evaluation of novel inhibitors
of class II PI4Ks and RIPK2/3 kinases

Design, syntéza a biologická aktivita nových inhibitorů
PI4K třídy II a RIPK2/3 kináz

Doctoral thesis

Supervisor: Mgr. Radim Nencka, Ph.D.

Prague, 2023

I hereby swear that I wrote this thesis myself and that it represents the results of my own work, unless otherwise stated in the text. All the literature sources of information employed are properly cited in the references section. This thesis and its contents have not been previously employed for obtaining any academic degree.

Prague, 20.11.2023   …………………………...

                                                                    Mbilo Misehe

Acknowledgements

Finally, tons of gratitude are dedicated to my family, especially to my parents, for their endless and firm support. Special thanks are for Laura, who patiently and valuably stood by me during the preparation of this thesis.

Abstract

Synthetic kinase inhibitors are chemical tools to investigate cellular roles of kinase enzymes and, potentially, find new treatments for various diseases that are connected with their dysregulated expressions and activities. This thesis focuses on two projects that were devoted to design, synthesize and evaluate novel compounds as kinase inhibitors.

In a first project, employing structure-based docking methods, novel 7-aryl- or 7-heteroaryl-substituted 4-aminoquinazoline-6-carboxamide compounds were developed as inhibitors of class II phosphatidylinositol 4-kinases (PI4K2A/2B). A simple synthetic approach enabled the preparation and the functionalization of the 4-aminoquinazoline scaffold in six steps. Enzymatic evaluation for activity and selectivity against PI4Ks (i.e., PI4K2A and class III PI4Ks) highlighted several compounds with low micromolar potency and good selectivity against PI4K2A. Moreover, the binding mode of the new compounds in the conserved ATP-binding sites of class II PI4Ks was corroborated by X-ray crystallography. This suggests the applied rationale of the design can be a strategical option to obtain more potent and selective PI4K class II inhibitors, to conduct additional investigations on these kinases.

In a second project, novel 4,6- and 4,6,7-substituted quinazoline compounds were developed and evaluated as inhibitors of receptor-interacting protein kinases 2 and 3 (RIPK2/3). The design of the molecules was guided by structural analyses of documented RIPK inhibitors. These precedents and new docking studies led to installation of an aminobenzothiazole moiety at position 4 of the quinazoline. In the meantime, multiple diversifications were introduced at positions 6 and 7 of the central scaffold, providing three series of structurally correlated compounds. These were synthesized employing a convergent cyclization methodology and palladium-catalyzed reactions. Enzymatic analyses of the molecules against the RIPK1-4 isoenzymes led to identification of various inhibitors selective for RIPK2, or for both RIPK2/3 kinases. In cell-based assays against RIPK2, most of the compounds exerted nanomolar inhibition of the NOD1/2 pro-inflammatory pathways. Surprisingly, for selected dual RIPK2/3 inhibitors, evaluation against RIPK3-mediated necroptosis showed only a limited cellular efficacy. For several lead compounds, assessments in human and mouse liver microsomes and plasma showed high metabolic stability in both species. Lastly, some of the best compounds also exhibited outstanding RIPK selectivity profiles in evaluations against other 58 human enzymes of the kinome. Thus, diversifying substitutions at positions 6 and 7 of the developed quinazoline derivatives enabled to explore significant differences in potency and specificity against RIPK2 and RIPK3. These discoveries could aid further development of new compounds with increased efficiency against these isoenzymes.

Abstrakt

Syntetické inhibitory kináz jsou chemickými nástroji pro zkoumání buněčných rolí těchto kináz a hledání nových způsobů léčby lidských onemocnění, která souvisejí s poruchami regulace jejich exprese a aktivity. Tato práce se zaměřuje na dva projekty, které byly věnovány návrhu, syntéze a hodnocení nových sloučenin jako inhibitorů kináz.

V prvním projektu byly, s využitím strukturních dokovacích metod, vyvinuty nové 7-aryl nebo 7-heteroaryl-substituované 4-aminochinazolin-6-karboxamidové sloučeniny jako inhibitory fosfatidylinositol 4-kináz třídy II (PI4K2A/2B). Pomocí jednoduchého syntetického přístupu a následné funkcionalizace byl v šesti syntetických krocích připraven žádaný 4-aminochinazolinový skelet. Vyhodnocení biologické aktivity a selektivity vůči PI4K (tj. PI4K2A a PI4K třídy III) odhalilo několik sloučenin s nízkou mikromolární aktivitou a dobrou selektivitou vůči PI4K2A. Způsob vazby nových sloučenin ve vazebném místě pro ATP PI4K třídy II byl potvrzen rentgenovou krystalografií a naznačuje, že použitý postup může vést k ještě účinnějším a selektivnějším inhibitorům PI4K třídy II pro další výzkum těchto kináz.

Ve druhém projektu byly vyvinuty nové 4,6- a 4,6,7-substituované chinazolinové sloučeniny jako inhibitory receptor-interagujících proteinkináz 2 a 3 (RIPK2/3). Návrh molekul byl veden strukturní analýzou zdokumentovaných inhibitorů RIPK. Tyto precedenty a nové dokovací studie vedly k zavedení aminobenzothiazolové skupiny na pozici 4 chinazolinu. Následně bylo zavedeno několik substitucí v polohách 6 a 7 centrálního skeletu, čímž vznikly tři řady strukturně příbuzných sloučenin. Ty byly připraveny pomocí konvergentní metodiky cyklizace a palladiem katalyzovaných reakcí. Vyhodnocení biologické aktivity v enzymatických esejích proti izoenzymům RIPK1-4 vedlo k identifikaci inhibitorů selektivních pro RIPK2, nebo pro obě RIPK2/3 kinázy. V buněčných esejích zaměřených proti RIPK2 většina sloučenin působila inhibici prozánětlivých drah NOD1/2 už v nanomolárních koncentracích. U vybraných duálních inhibitorů RIPK2/3, překvapivě, hodnocení aktivity proti nekroptóze zprostředkované RIPK3 v buněčných esejích odhalilo pouze omezenou účinnost. Byla změřena stabilita několika hlavních sloučenin v lidských a myších jaterních mikrosomech a plazmě. Měření ukázalo vysokou metabolickou stabilitu v obou případech. Tři nejlepší inhibitory vykazovaly vynikající profily selektivity, když byly hodnoceny proti 58 dalším enzymům z lidského kinomu. Diverzifikace substitucí v polohách 6 a 7 vyvinutých chinazolinových derivátů tak umožňuje zkoumat významné rozdíly v účinnosti a specifitě vůči RIPK2 a RIPK3. Tato zjištění by mohla napomoci dalšímu vývoji nových sloučenin se zvýšenou účinností proti těmto isoenzymům.

List of abbreviations

AcOH	acetic acid
ADP	adenosine diphosphate
ALK	anaplastic lymphoma kinase
AMP	adenosine monophosphate
AMPKα	AMP-activated protein kinase alpha
AP-1	adaptor protein-1
ASK1	activator of S-phase kinase 1
ATP	adenosine triphosphate
ATP K_m	enzyme constant of affinity for ATP
Aurora-A	Aurora kinase-A
Bcr-Abl	breakpoint cluster region-Abelson murine leukemia viral oncogene
BTK	Bruton's tyrosine kinase
C14-Tri-LAN-Gly	myristic-alanine-D-iso-glutamine-ε-meso-lanthionine-glycine
CARD	caspase activation and recruitment domain
CaMK	calcium/calmodulin-dependent protein kinase
CDK1/2/6/7/9	cyclin dependent kinase 1/2/6/7/9
CHK1	checkpoint kinase 1
CK1γ1	casein kinase 1 gamma 1
CK2α2	casein kinase 2 alpha 1
c-RAF	raf murine leukemia viral oncogene
cryo-EM	cryo-electron microscopy
CYP450	cytochrome P450
DAMP	damage-associated molecular pattern
DCM	methylene chloride
DMF	*N,N*-dimethylformamide
DMF-DMA	*N,N*-dimethylformamide dimethyl acetal
DMSO	dimethyl sulfoxide
DMSO-d_6	hexadeuterated dimethyl sulfoxide
DPPF	1,1′-bis(diphenylphosphino)ferrocene
DRAK	death-associated protein kinase related
EEF2K	eukaryotic elongation factor-2 kinase
EGFR	epidermal growth factor receptor
EphA5	ephrin receptor type-A 5
EphB4	ephrin receptor type-B 4
eq	equivalent/s
ESI	electrospray ionization

Et$_2$O	diethyl ether
EtOAc	ethyl acetate
EtOH	ethanol
FDA	Food and Drug Administration
Fyn	tyrosyne kinase Fyn
GSK3β	glycogen synthase kinase-3 beta
h	hour
Her-2	human epidermal growth factor receptor-2
hERG	human *ether-à-go-go*-related gene
HRMS	high resolution mass spectrometry
IAP	inhibitor of apoptosis
IC$_{50}$	half-maximal inhibitory concentration
IGF-1R	insulin-like growth factor 1 receptor
IKKα	inhibitory kappa B kinase alfa
IP$_4$	inositol 1,3,4,5-tetrakisphosphate
IRAK4	interleukin-1 receptor-associated kinase 4
JAK2	Janus kinase 2
KDR	kinase insert domain receptor
LC-MS	liquid chromatography-mass spectrometry
LOK	serine/threonine kinase 10
Lyn	tyrosine kinase Lyn
LUBAC	linear ubiquitin chain assembly complex
LPS	lipopolysaccharide
MAPK	mitogen-activated protein kinase
MAPKAP-K2	MAPK-activated protein kinase 2
MAT1	methionine adenosyl transferase´1
MDP	muramyl dipeptide
MEK1	MAPK/extracellular signal-regulated kinase 1
MeOH	methanol
min	minute
MLK1	mixed lineage kinase 1
MLKL	mixed lineage kinase domain-like pseudokinase
Mnk2	MAPK interacting kinase 2
MS	mass spectrometry
MSK2	mitogen and stress-activated kinase 2
MST1	macrophage stimulating 1
mTOR	mammalian target of rapamycin

MW	molecular weight
NEK2	never-in-mitosis-A related kinase 2
NIS	*N*-iodosuccinimide
NF-κB	nuclear factor kappa-light-chain-enhancer of activated B cells
NOD1/2	nucleotide-binding-oligomerization-domain-containing protein 1/2
NMR	nuclear magnetic resonance
p70S6K	ribosomal protein S6 kinase
PAK2	p21-activated kinase 2
PDB	Protein Data Bank
PDA	photodiode array
PDGFRβ	platelet derived growth factor receptor beta
PH	pleckstrin homology
PI	phosphatidylinositol
PI3K	phosphatidylinositol 3-kinase
PI4K2A/2B/A/B	phosphatidylinositol 4-kinase 2A/2B/A/B
PI4P	phosphatidylinositol 4-monophosphate
Pim-1	proviral integration site for Moloney murine leukemia virus 1
PKA	protein kinase A
PKB	protein kinase B
PKCα/θ	protein kinase C alfa/delta
PKG1α	cyclic guanosine monophosphate-dependent protein kinase 1 alpha
Plk3	polo like kinase 3
PRAK	p38 regulated/activated protein kinase
RHIM	receptor homotypic interaction motif
RIPK1/2/3/4/5/6/7	receptor-interacting protein kinase 1/2/3/4/5/6/7
ROCK-I	Ras homolog-associated protein kinase I
Rse	*receptor sectatoris*
Rsk1	p90 ribosomal S6 kinase 1
rt	room temperature
Rt	retention time
SAPK2A	stress-activated protein kinase 2 A
SAR	structure-activity relationship
SPhos	2-dicyclohexylphosphino-2',6'-dimethoxybiphenyl
SRPK1	serine/arginine-rich splicing factor protein kinase 1
TAK1	transforming growth factor beta-activated kinase 1
TCEP	tris(2-carboxyethyl)phosphine
TEV	tobacco etch virus

TGN	trans-Golgi network
TLC	thin-layer chromatography
TLR	toll-like receptor
TNF-α	tumor necrosis factor alpha
UPLC	ultra performance liquid chromatography-mass spectroscopy
UV	ultraviolet
Wnt	wingless-related integration site
XantPhos	4,5-bis(diphenylphosphino)9,9-dimethylxanthene
XIAP	X-linked inhibitor of apoptosis protein

Table of Contents

CHAPTER 1

1.1. Introduction to human kinases

Human kinases represent a network of hundreds of cytosolic and transmembrane enzymes expressed from the genome (kinome), which are interrelated by their encoded genetic sequences, phenotypes and bioactivities.[1] Typically, most kinases can function as highly selective catalysts in phosphoryl group transfer reactions from donor molecules (i.e., nucleoside triphosphates) to other definite molecular substrates. For this reason, these enzymes are also referred to as nucleoside triphosphate-dependent phosphotransferases.[2,3] Nevertheless, kinases can also serve as allosteric modulators (e.g., scaffolding proteins) of biomolecules in fashions that do not depend on their phosphorylating action.[4,5]

Known enzymes of the human kinome can be divided in protein kinases (serine/threonine, tyrosine, tyrosine-kinase-like and dual-specificity kinases), lipid kinases, sugar kinases, and nucleoside kinases, depending on their functional specificities.[1,6–8] Collectively, kinase functions play relevant roles in the regulation of signaling, remodeling of the membranes and molecular trafficking in and out of the cellular environment.[6,9] In addition, kinases control essential steps of the synthesis and metabolism of elaborated carbohydrates and genes.[7,8] Dysregulations of these physiological processes can be detrimental to the cells and can lead towards states that are pathological.[6]

As dysregulated kinase activities have often been correlated with human disorders, these enzymes have been incrementally proposed and explored as attractive therapeutic targets by scientists.[3,10] These research investigations have led to the identification and development of synthetic compounds as kinase inhibitors. These demonstrated to be targeted chemical tools highly valuable to conduct biological and clinical studies on kinases.[11,12]

The synthesis of novel compounds inhibiting kinases has been the central focus of my PhD thesis.

1.2. Synthetic kinase inhibitors as tools for chemical biology and therapeutics

Typical synthetic kinase inhibitors could be described as heterocyclic, lipophilic, low molecular weight (i.e., MW < 900 Daltons) organic molecules of artificial origin.[13,14] These present structures with the specific capability of inducing downregulations of kinase' activities. Inhibitory effects are usually elicited by occupying binding sites (pockets) of their protein targets, interacting with amino acids that are essential for the regulation of their functionality and/or stability.[15]

Up to the year 2022, the drug regulatory agencies worldwide (e.g., the American Food and Drug Administration, FDA) have approved about a hundred inhibitors of kinases for the treatment of specific human disorders, including cancers, autoimmune, infectious, inflammatory, metabolic and cardiovascular diseases.[16,17] Recently, hundreds of small molecules have been reported as being under investigation in various clinical trials against kinases as potential therapeutic treatments.[18]

Kinase inhibitors useful for biological and clinical research often require structural optimization due to similarities in the kinases' constructs that can lead towards poor enzyme selectivity.[19] A lack of adequate specificity, in turn, can hinder a reliable understanding of biological enzymes' functions and regulatory mechanisms. Furthermore, it can lead towards relevant cytotoxic effects.[20] Besides bearing points of similarities, kinase enzymes can also undergo frequent structural mutations, which can have severe impact on their functional protein folds and ligand binding affinities.[20] To overcome selectivity and affinity limitations of compounds, the rational development of targeted kinase inhibitors is usually based on thorough characterization and analysis of structures and conformations of kinases, as these have appeared to be essential determinants of their specific functions and regulations.[20,21]

1.3. Structural and regulatory features of kinases

Currently, tridimensional structural/conformational analyses of kinases as well as their interactions with ligands can be conducted employing various experimental spectroscopy techniques (i.e., X-ray crystallography; nuclear magnetic resonance, NMR; cryo-electron microscopy, cryo-EM).[22–24] In addition, theoretical investigations of enzyme/ligand binding modalities can be conducted employing predictive computational methodologies, as, for instance, molecular docking.[25] Over extensive research studies, a vast majority of kinases exhibited conserved structural features, which are localized predominantly in their kinase domains, also referred to as their catalytic modules.[26,27]

1.3.1. Catalytic domain of kinases

Typical kinase domain constructs contain an N-lobe rich in beta-strands and a C-lobe rich in α-helices, which are interspaced with a flexible connection, known as the hinge. The hinge region of the enzymes interacts physiologically with the scaffold of nucleoside triphosphates, as, for instance, the adenine heterocycle of adenosine triphosphate (ATP **1**, **Figure 1**).[26] The N-lobe also features an αC-helix, which is involved in conformational changes of the kinase domains from states of activity to inactivity.[27,28]
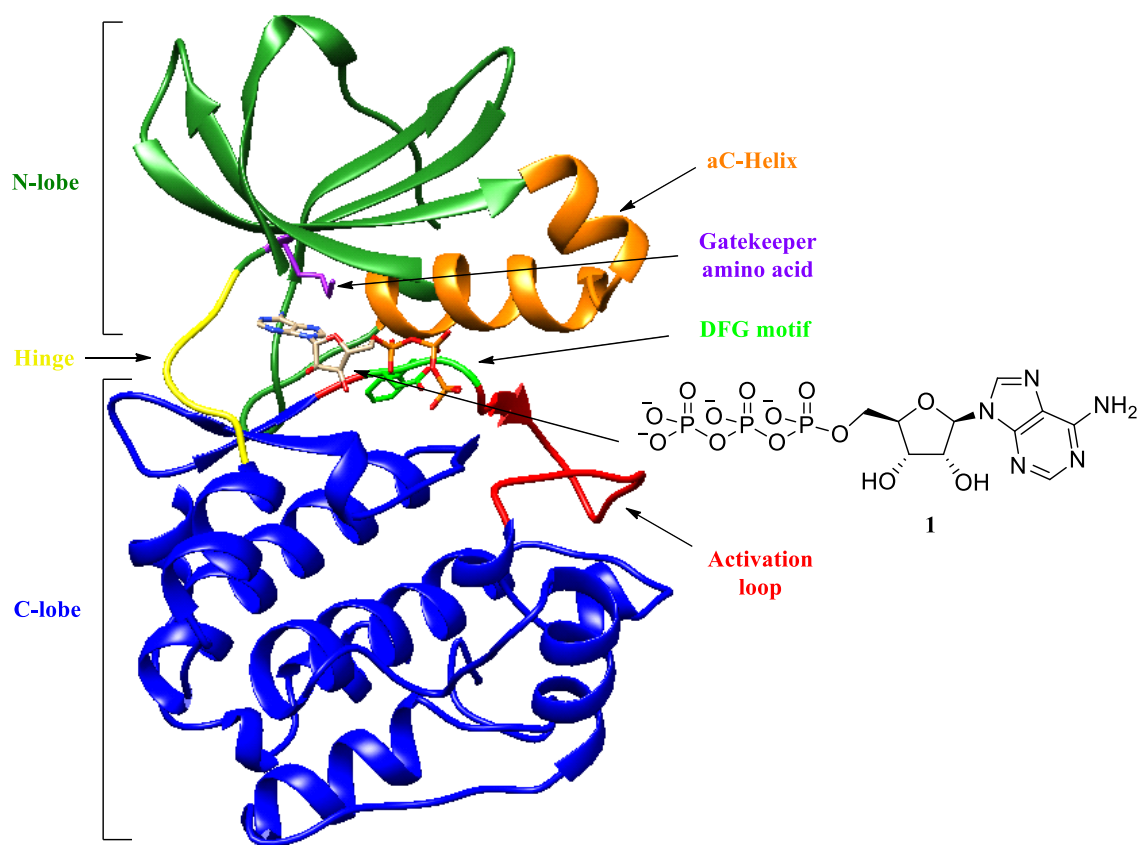
Figure 1. Structure of ATP **1** in complex with the protein kinase A (PKA) catalytic domain (PDB 1ATP[29]). Various conserved structural elements across kinases are highlighted in distinct colors.

Between the N- and C-lobes are centered structural elements that are essential for execution of the phosphorylating function of the enzymes. For example, a specific amino acid, known as the "gatekeeper"[30], establishes an access for the ligand ATP **1** to its binding site. In addition, an exposed peptide chain (activation loop) plays a pivotal role in regulating the phosphoryl group transfer from ATP **1** to other molecular targets of the enzymes.[30] Notably, selective phosphorylations and/or autophosphorylations of amino acids localized in the activation loop can modulate the catalytic activities of kinases.[31,32] Additionally, towards the N-terminal region, this regulatory loop contains a highly conserved sequence of three amino acids (the DFG motif), usually consisting of aspartic acid (Asp, D), phenylalanine (Phe, F) and glycine (Gly, G).[32] The DFG motif can rearrange between two main opposite structural orientations (known as "DFG-in" and "DFG-out").[32,33]

Functionally active kinase domains share a tendency to adopt similar "DFG-in" structural orientations, where the essential Asp (D) residue is oriented towards the inside of the ATP-binding sites, allowing the enzymes to exert ATP-mediated phosphorylations.[34] By contrast, functionally inactive kinase domains can structurally reorganize into less conserved "DFG-out" conformations, bearing generally the Asp (D) residue of the DFG sequence oriented towards the outside of the ATP-binding site. Importantly, in these inactive DFG

conformations the adjacent Phe (F) residue can rotate towards the hinge cleft and open access to allosteric pockets localized beneath the αC-helix of the N-lobe of the kinase domains.[34,35] Statistically, a large majority of synthetic kinase inhibitors have been identified and developed to interact specifically with either the "DFG-in" or the "DFG-out" conformations of the kinase domains to disrupt enzyme activities.[30,36] Representative are the breakpoint cluster region-Abelson tyrosine protein kinase (Bcr-Abl kinase) inhibitors dasatinib **2** and imatinib **3** (**Figure 2**), respectively.[37,38]
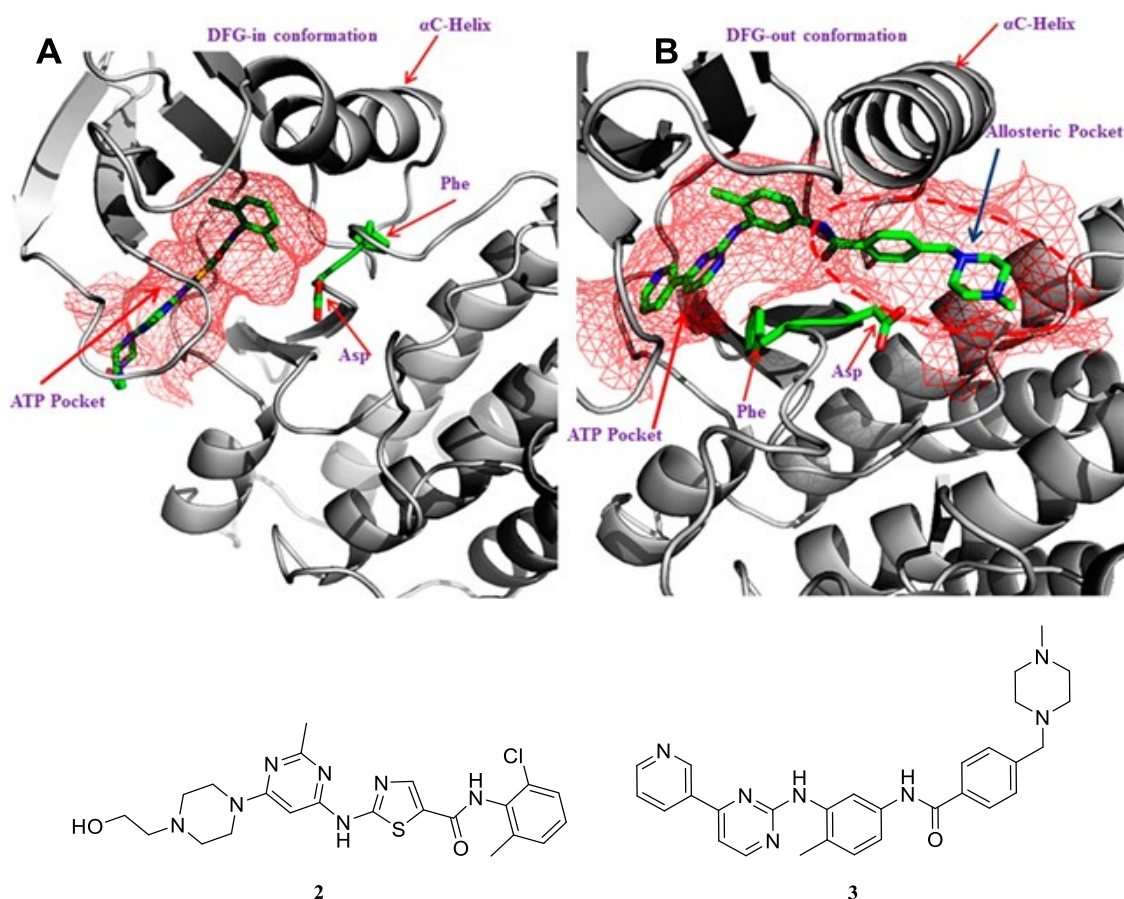
Figure 2. Representation of the DFG-in/active (A) and DFG-out/inactive (B) conformations of the Bcr-Abl kinase domain in complex with inhibitors dasatinib **2** and imatinib **3**, respectively.[35]

1.3.2. Allosteric sites and domains of kinases

Characterizations of the full-length structures of kinases also have led to identification of regulatory allosteric binding sites that are localized out of their ATP-binding pockets, or even out of their phosphorylating modules.[39] Structural/conformational rearrangements of allosteric regions appear to regulate various protein-protein interactions and other functionalities of kinases, including their phosphorylating action.[39] An example of an allosteric kinase module is the N-terminal pleckstrin homology (PH) domain of protein kinase B (PKB), which, on binding to the endogenous phospholipid inositol 1,3,4,5-

tetrakisphosphate (IP$_4$, **4**), displays the ability to rearrange its conformation and to negatively modulate the activity of the PKB kinase domain (**Figure 3**).[40]
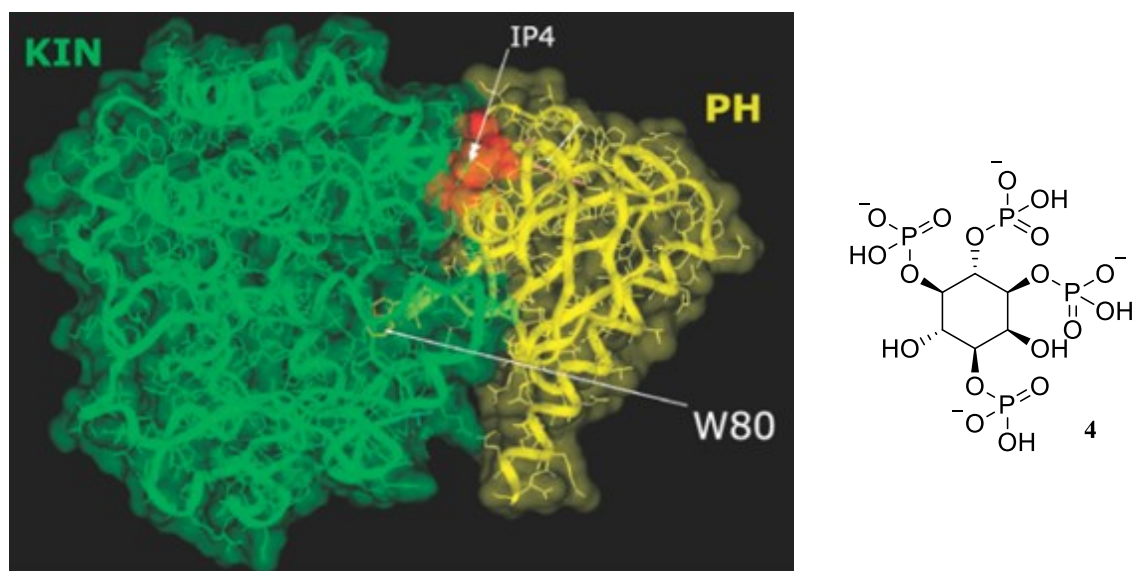
Figure 3. Model of the PKBα PH domain (yellow) and kinase domain (green) in complex with IP$_4$ **4**.[40] In the model, the phospholipid is represented as CPK (Corey-Pauling-Koltun) orange-red spheres.

Importantly, extending the investigations of structural and regulatory features of allosteric regions inside or outside of the kinase domains of kinases has led to the development of small molecule inhibitors which exhibited a remarkable affinity and specificity for their enzyme targets.[39,41] An illustrative example is the selective PKB allosteric inhibitor borussertib **5**, which can disrupt the PKB activity by interacting simultaneously with both the PH and the kinase domains of this protein kinase (**Figure 4**).[42]
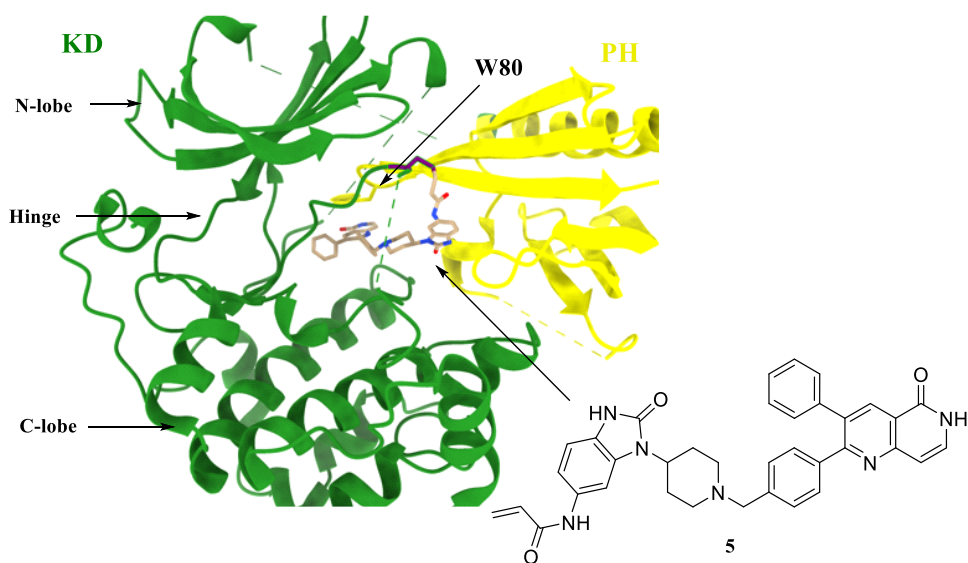
Figure 4. Structure of inhibitor borussertib **5** in complex with PKB (PDB: 6HHF[42]). The kinase domain and PH domain are colored as in the model in **Figure 3**.

1.4. Mechanistic classification of kinase inhibitors

Kinase inhibitors can display distinct molecular structures and binding regions within their kinase targets, which in turn can enable diverse mechanisms of functional inhibition. Based on a mechanistic classification, compounds inhibiting kinases may belong to six main types (type I-VI, **Figure 5**).[15]
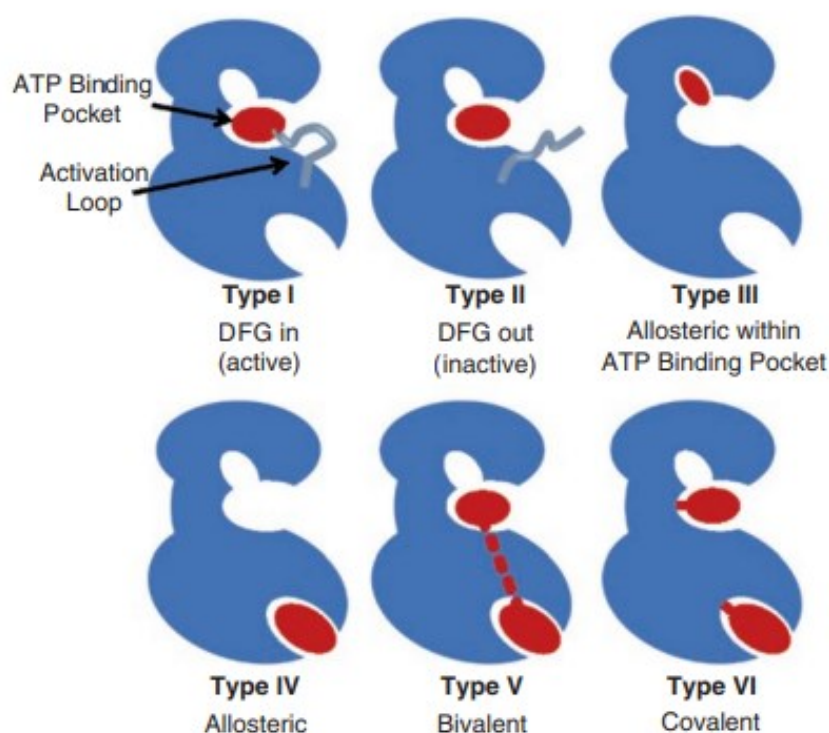
Figure 5. Representation of the summary classification of small molecule kinase inhibitors. Small molecules are depicted as red ovals. Enzyme targets are colored in blue.[43]

1.4.1. Type I inhibitors

Type I inhibitors mainly function by interacting with the ATP-binding sites of kinase domains that are catalytically active ("DFG-in" conformations), precluding ATP **1** from binding to its specific site.[30] Illustrative examples are the epidermal growth factor receptor (EGFR) inhibitors gefitinib **6** and erlotinib **7** (**Figure 6**).[44,45]
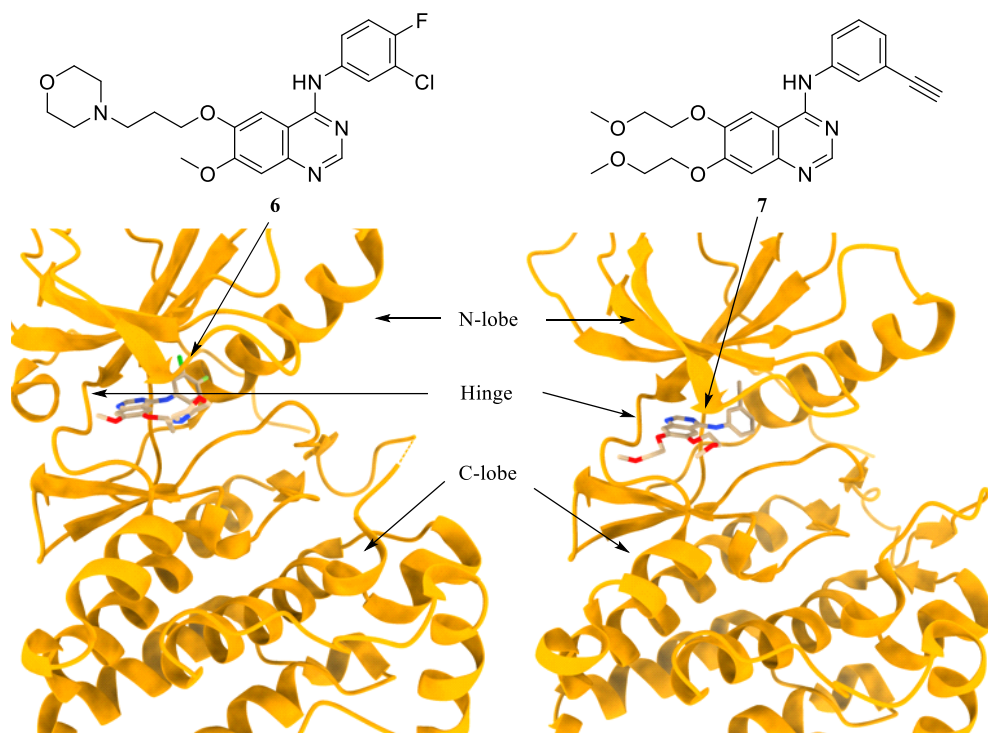
Figure 6. Structures of inhibitors gefitinib **6** and erlotinib **7** in complex with the EGFR kinase domain (PDB: 2ITY[44] and 1M17[45], respectively).

As a conserved structural feature, type I inhibitors share usually heterocyclic central scaffolds (i.e., quinazoline) emulating or strengthening the hydrogen bonding interactions that are formed by the purine scaffold of ATP **1** in the hinge of the kinase domains.[30] The main scaffolds of these molecules are usually decorated with additional functional groups, serving to interact with specific cavities and amino acids of the enzymes that are situated topologically adjacent to the sites getting in contact with the ATP-adenine heterocycle.[46] Exploiting essential structural dissimilarities presented in the catalytic sites of kinases with appropriate decorations of the main scaffolds has been providing highly efficient kinase inhibitors thus far.[46]

1.4.2. Type II inhibitors

Type II ligands also inhibit kinases by competing with physiological ATP **1**. However, these molecules mainly interact with enzymes that are catalytically inactive, stabilizing "DGF-out" conformations of the kinase domains.[36] Illustrative examples are the Bcr-Abl kinase inhibitor nilotinib **8** and the multi-kinase inhibitor sorafenib **9** (**Figure 7**).[47,48]
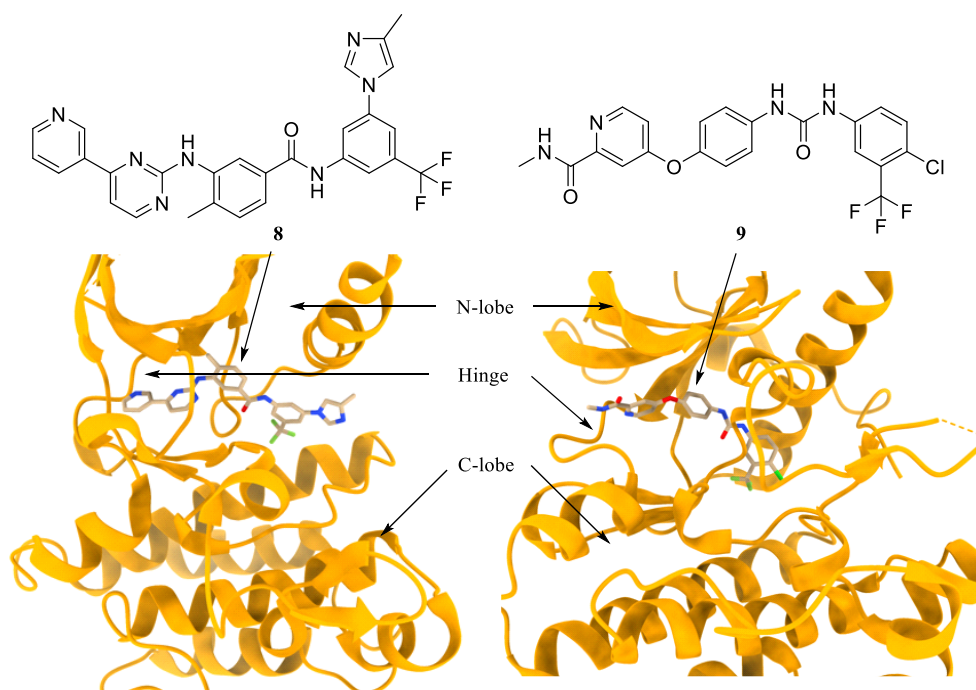
Figure 7. Structures of nilotinib **8** and sorafenib **9** in complex with the Bcr-Abl kinase domain (PDB: 3CS9)[47] and the kinase insert domain receptor (KDR) catalytic domain (PDB: 3WZE)[48], respectively.

Although structurally they may resemble the type I, type II molecules share a tendency not to interact as productively in the hinge site of their enzyme targets, primarily because of a steric bulk generated by the inactive orientations of the DFG amino acids.[35,49] This binding limitation of compounds can be commonly circumvented by introducing additional decorative substituents, serving to fit and interact with lipophilic allosteric pockets that are scarcely conserved across kinases. Notably, these binding sites can be accessed mainly in the inactive DFG-out conformations of the proteins.[35,49]

1.4.3. Type III inhibitors

Type III inhibitors interact with kinases' allosteric binding sites localized in the close vicinity of their ATP-binding regions, usually avoiding contacts with the hinge of the enzymes.[50] Generally, these compounds can obstruct the binding of molecular substrates that are physiologically phosphorylated by kinases and, simultaneously, can stabilize inactive enzyme conformations.[41] The mitogen-activated protein kinase/extracellular signal-regulated kinase (MEK) inhibitors trametinib **10** and cobimetinib **11** (**Figure 8**) are representative examples.[51,52]
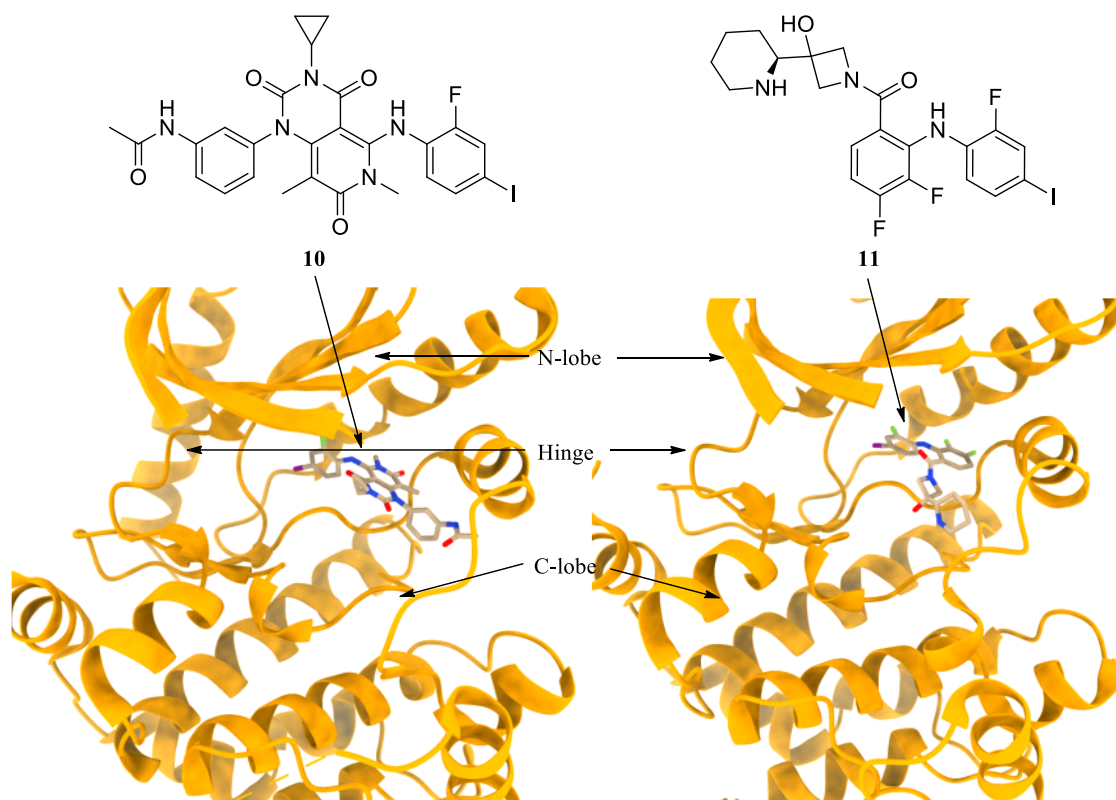
Figure 8. Structures of trametinib **10** and cobimetinib **11** in complex with the MEK1 kinase domain (PDB: 7M0Y[51] and 4AN2[52], respectively).

Notably, type III molecules exhibited high specificities for their targets, since their binding pockets are less conserved than ATP-binding regions across kinase enzymes.[41,50]

1.4.4. Type IV inhibitors

Type IV inhibitors bind into kinases' allosteric regions localized far from the ATP-binding pockets.[50] Thus, intrinsically, these compounds do not compete with ATP **1** for its binding site. On the other hand, type IV ligands can prevent the binding of other regulatory substrates of kinases. In this fashion, they can stabilize inactive enzyme conformations.[50] Representative examples of type IV ligands are the kinase inhibitors asciminib **12** and GNF-2 **13** (**Figure 9**), which both fit the myristoyl pocket that is situated within the C-lobe of the Bcr-Abl kinase domain.[53,54]
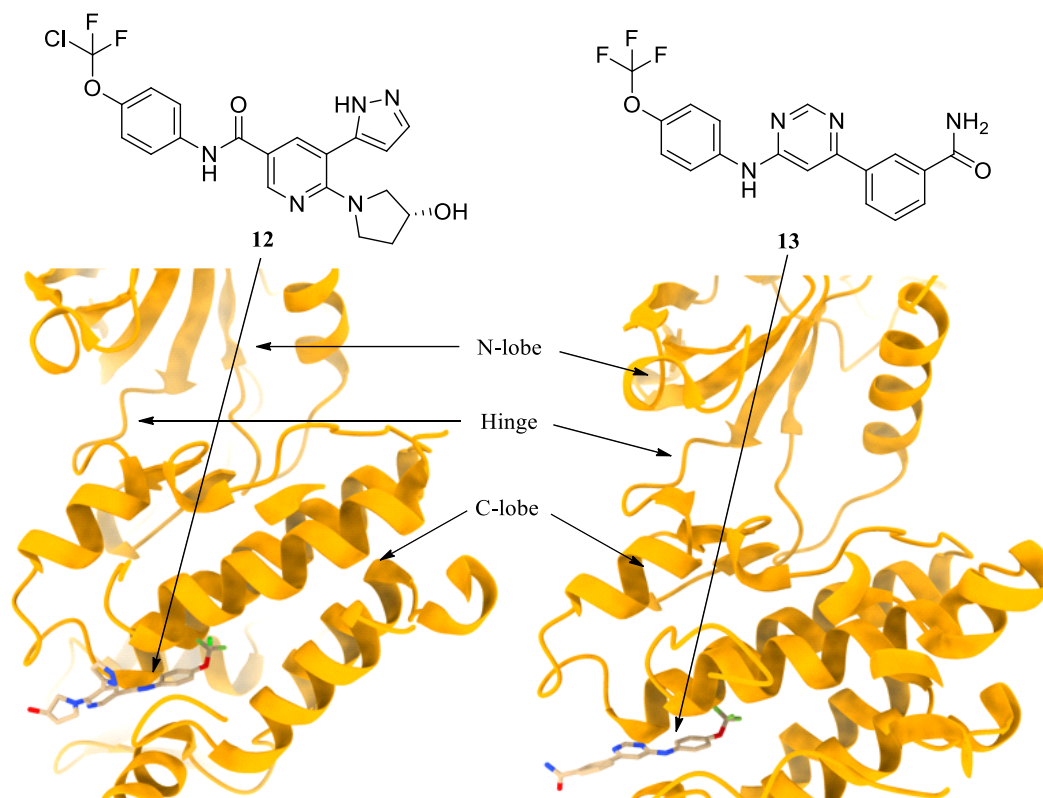
Figure 9. Structures of asciminib **12** and GNF-2 **13** in complex with the Bcr-Abl kinase domain (PDB: 5MO4[53] and 3K5V[54], respectively).

Type IV inhibitors exhibit high selectivity, analogously to the type III, since they interact with allosteric regions commonly presenting structural elements that are peculiar to defined kinases.[50,55]

1.4.5. Type V inhibitors

Type V inhibitors are referred to as bifunctional inhibitors, since these can extend concurrently their interactions with two distinct regions of kinases as, for instance, their ATP-binding sites and other regulatory regions.[15,56] In these cases, type V molecules can bind to the hinge *via* typical ATP-mimetic heterocyclic scaffolds, which are further decorated with peculiar peptide-mimetic fragments. The latter decorations can enable interaction specificity of the molecules also with allosteric regions of the enzymes.[57] A typical example is the adenosine oligo-(D-arginine) conjugate-based molecule ARC-1034 **14**, which selectively inhibits PKA (**Figure 10**).[58]
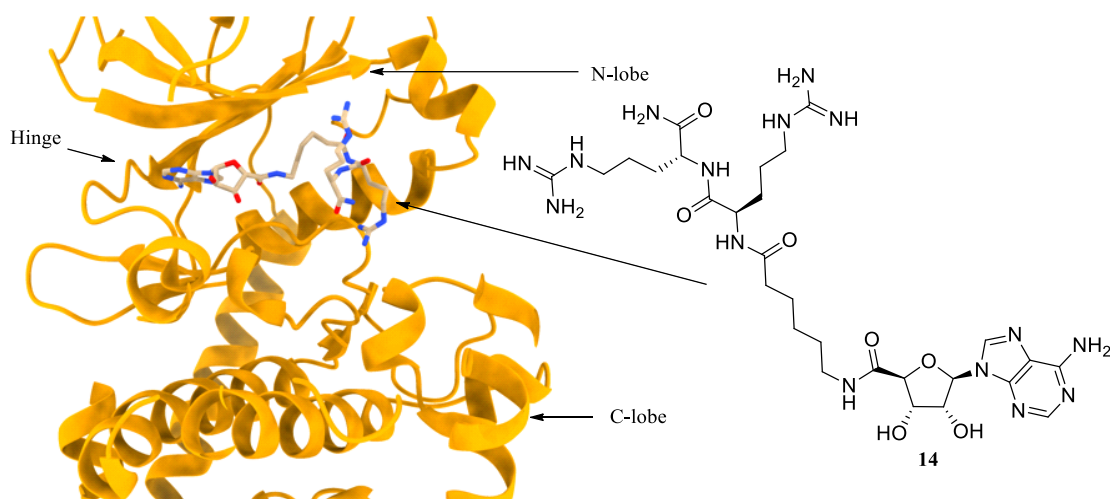
Figure 10. Structure of ARC-1034 **14** in complex with the PKA kinase domain (PDB: 3BWJ[58]).

Bifunctional compounds display high affinity and specificity because of their enhanced ability to form multiple contacts with their enzyme targets. Nevertheless, intrinsic high molecular weights and low stability can often limit both cell permeability and bioavailability of this type of molecules.[56,59]

1.4.6. Type VI covalent inhibitors

Lastly, type VI inhibitors present a capability to interact covalently with kinases to suppress their activities.[15] Representative molecules function by interacting in the hinge region of kinases through heterocyclic scaffolds, preventing ATP **1** from binding to its site. The main scaffolds are commonly linked to α,β-unsaturated carbonyl functionalities (i.e. acrylamides), serving as electrophiles in hetero-conjugate additions with reactive amino acids of the enzymes (e.g., cysteine residues, nucleophiles).[15,60] The covalent interactions between kinases and ligands can lead to the formation of irreversible adducts, as in the cases of the EGFR inhibitor afatinib **15** and the Bruton's tyrosine kinase (BTK) inhibitor ibrutinib **16** (**Figure 13**).[61,62]
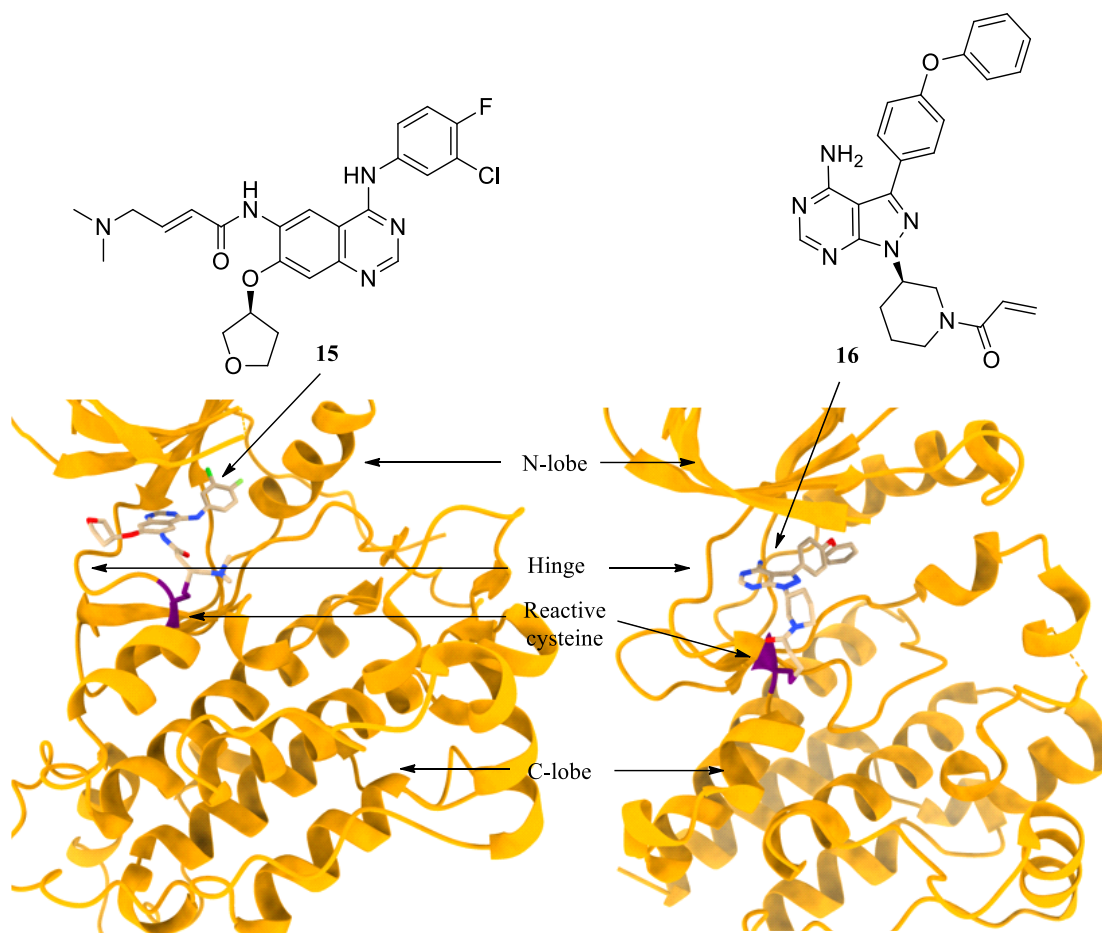
Figure 11. Structures of afatinib **15** and ibrutinib **16** in complex with the EGFR kinase domain (PDB: 4G5J)[61] and BTK kinase domain (PDB: 5P9J)[62], respectively.

Since irreversible ligands have shown relevant limitations, such as off-target cytotoxicity[63], safer covalent inhibitors that can form reversible adducts with enzymes were later developed.[63,64] Typically, reversible covalent inhibitors are characterized by electron withdrawing groups (EWG, e.g., a nitrile group) present at the alpha-position with respect to the acrylamides, enabling the retro-conjugate addition and dissociation of kinase/inhibitor adducts.[64] The BTK inhibitor rilzabrutinib **17** is a representative example of a reversible covalent ligand (**Figure 14**).[65]
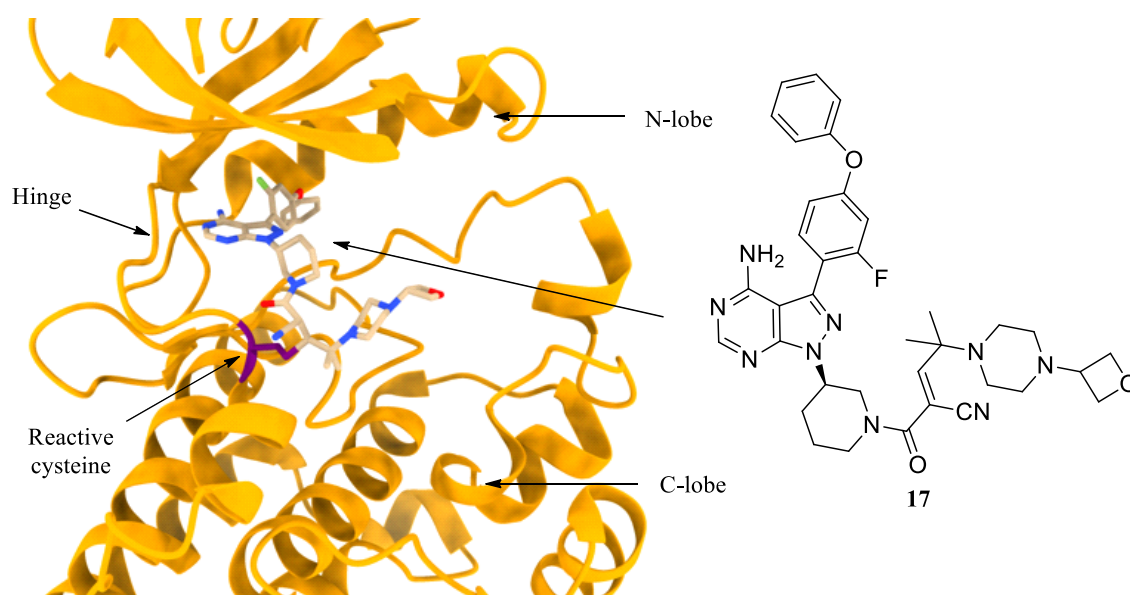
Figure 12. Structure of rilzabrutinib **17** in complex with the BTK kinase domain (PDB: 7L5P[65]).

1.5. General overview of following chapters

The research investigations included in this thesis have focused independently on the design, synthesis and evaluation of novel potential type I inhibitors targeted towards either class II phosphatidylinositol 4-kinases (PI4K2A and PI4K2B), or receptor-interacting protein kinases 2 and 3 (RIPK2 and RIPK3). Being these two distinct subsets of kinases, the projects will be described in two separate chapters (**Chapters 2** and **3**, respectively). In each chapter, concise introductions to the selected kinase targets and to some of their known inhibitors will first be given. Subsequently, for each project, the rationale of the design of the new compounds, the synthetic and biological results and conclusions will be discussed. Following **Chapters 4** and **5** will detail preparative procedures and characterizations of the compounds that are related to **Chapters 2** and **3**, respectively.

CHAPTER 2

2.1. Introduction to PI4Ks

According to observed similarities in their encoded genetic sequences and phenotypes, human PI4Ks can be clustered into a class II (PI4K2A, PI4K2B) and a class III (PI4KA, PI4KB). The two enzyme classes display reciprocal diversities in their sensitivities to substances.[66,67] In addition, while PI4KA and PI4KB share features in their genes and their tridimensional structures with other characterized phosphoinositide lipid kinases, for example phosphatidylinositol 3-kinases (PI3Ks)[68,69], the enzymes PI4K2A and PI4K2B present atypical structural elements, which are exhibited only by a few other known kinases.[70,71] Nevertheless, all the four PI4Ks are identified as lipid kinases that act as selective catalysts in the conversion of phosphatidylinositol (PI **18**) into phosphatidylinositol 4-monophosphate (PI4P **19**, **Figure 13**).[68]

18   **19**
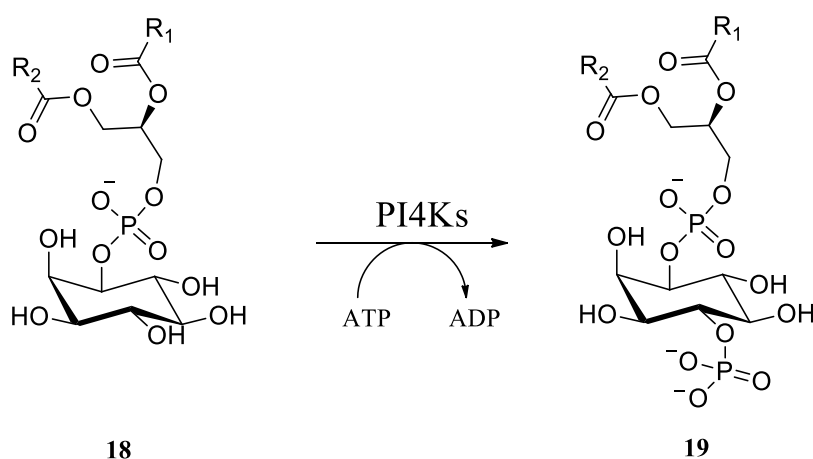
Figure 13. PI4K catalytic transfer reaction of a phosphoryl group onto PI **18** leading to PI4P **19**.

PI4P **19** may serve as an essential lipid substrate for the further elaboration of other phosphoinositides involved in PI3K and receptor-activated phospholipase C (PLC) signaling cascades.[72] Additionally, PI4P **19** may function as a signaling lipid in the regulation of sphingolipid metabolism, reorganization of the cellular framework and trafficking of molecules through the cell membranes.[73,74]

Biological roles of individual PI4Ks exhibit little redundancy and strong dependency on differences in the enzyme distributions at a subcellular level (**Figure 14**).[72,75]
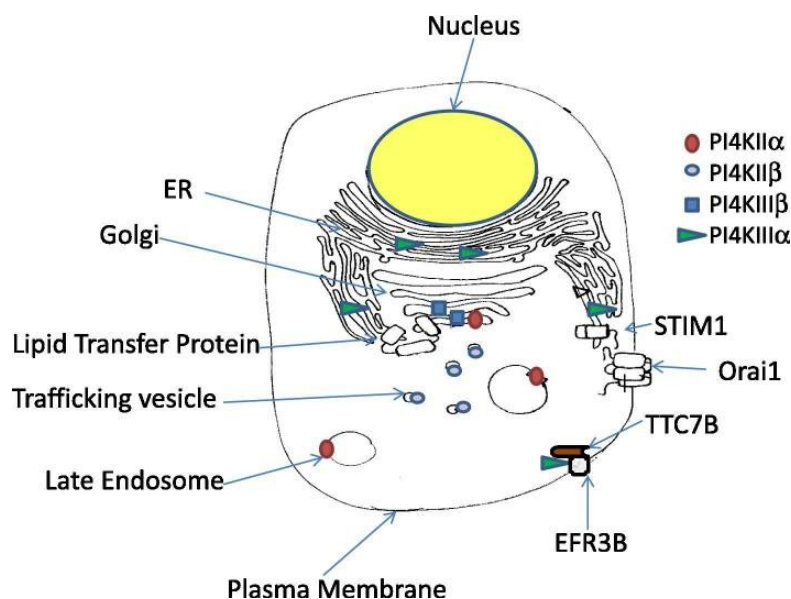
Figure 14. Subcellular compartmentation of PI4Ks.[75] EFR3B, TTC7B, Orai1 and STIM1 represent known protein partners involved in the biosynthesis of PI4P in the membranes.[75]

Class II PI4Ks have been localized primarily in membrane compartments. PI4K2A is mainly detected as active in lysosomes, endosomes and in the trans-Golgi network (TGN), whereas PI4K2B is found as active in trafficking vesicles, or as inactive in the cytosol.[66,76] Class III PI4Ks are instead expressed and functionally active both in the cytosol and in membrane compartments. PI4KA often associates to the plasma membrane and the endoplasmic reticulum, while PI4KB is consistently accumulated in the Golgi apparatus.[67,75]

2.2. Class II PI4Ks and human diseases

PI4K2A and PI4K2B display similar recruiting mechanisms *via* palmitoylation, but uncorrelated cellular expressions, compartmentations, and rates of activity.[77,78] Therefore, their pathophysiological roles and therapeutic potential have been elucidated to diverse extents.

Being mostly an enzyme associated with membranes in an active state, PI4K2A regulates multiple cell signaling pathways that are implicated in the development of carcinomas, including the Wnt, the EGFR and the Her-2 pathways.[79–81] Recent oncological studies have led scientists to associate the imbalance of the PI4K2A activity to angiogenesis and oncogenesis, suggesting that the inhibition of this lipid kinase may be a potential therapeutic strategy against the onset and development of cancer.[81–83] In addition, recent research evaluations have showed that the dysregulated expression and activity of PI4K2A might be linked to encephalopathies and metabolic disorders, including lysosomal storage diseases (i.e., Gaucher's disease) and neurological diseases.[84–86]

The PI4K2B functions and potential as a therapeutic target are currently less thoroughly documented, as this enzyme is poorly expressed in cells with respect to the PI4K2A isoenzyme. Furthermore, PI4K2B is often set as inactive in the cytosol.[66,75] Recently, the PI4K2B enzyme was proposed to be a major contributor to the regulation of the TGN/endosomal trafficking as well as the Wnt signaling pathway.[87] Specifically, this PI4K2B activity has been attributed to protein-protein interactions with the adaptor protein-1 (AP-1).[87] For this reason, the targeted inhibition of PI4K2B has been suggested as a promising strategy for the treatment of oncological disorders.[88]

In addition, it should be mentioned that both PI4K2A and PI4K2B have also been recently identified as implicated in toll-like receptor (TLR) signaling cascades, correlating with the productions of pro-inflammatory cytokines, such as tumor necrosis factor alpha (TNF-α).[89] Thus, further investigations might reveal these enzymes as potential targets for the treatment of inflammatory diseases.[89,90]

2.3. PI4K class II small-molecule inhibitors known in the literature

Reliable insights in the biology and therapeutic potential of class II PI4Ks are challenged by a scarce number of selective inhibitors reported in the literature.[90,91]

Some known natural products exhibited inhibitory activity against class II PI4Ks. Representative examples are the polyphenols epigallocatechin gallate **20**[92] and resveratrol **21**[93] (**Figure 15**).
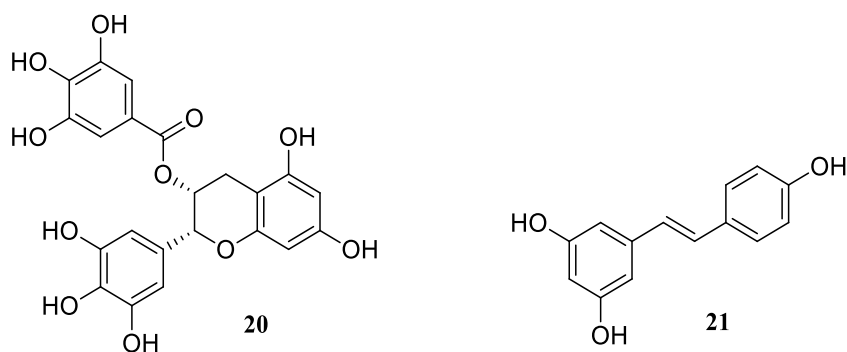
Figure 15. Structures of epigallocatechin gallate **20** and resveratrol **21**.

These molecules displayed additional off-target effects on other enzymes.[94,95] Thus, they did not possess adequate specificity profiles to explore cellular roles of class II PI4Ks.

Endogenous, adenine-based substrates, such as ADP **22**, AMP **23**, and adenosine **24** (**Figure 16**), also are known to exert inhibitory effects on class II PI4Ks.[96] Even so, these compounds are intrinsically devoid of relevant selectivity across kinases.
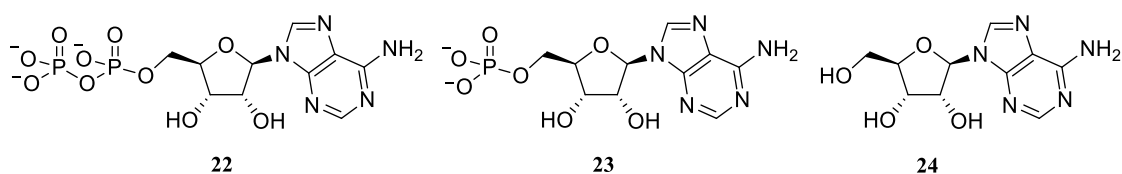
Figure 16. Structures of ADP **22**, AMP **23** and adenosine **24**.

Recent research studies led to the identification of synthetic PI4K class II inhibitors as MD59 **25**[71] and NC02 **26**[97] (**Figure 17**), bearing a purine- and a coumarin-based structures, respectively, which, in biochemical evaluations, showed good affinity and selectivity for PI4K2A over class III PI4Ks.[71,97]
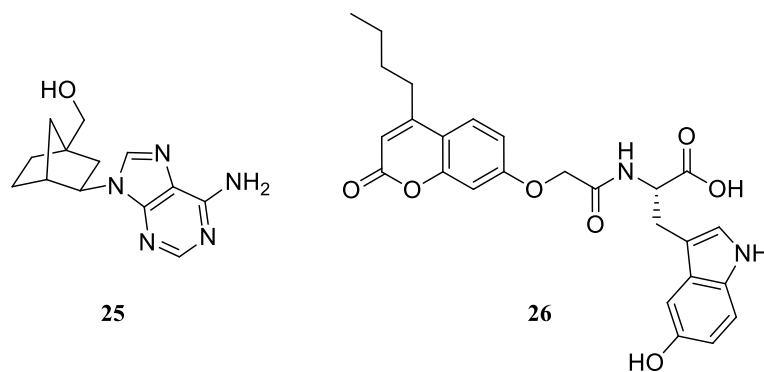
Figure 17. Structure of MD59 **25** and NC02 **26**.

Both MD59 **25** and NC02 **26** displayed a type I mechanism of binding within the kinase domain of PI4K2A, which could suggest a potential inhibitory efficacy also against the homologous PI4K2B isoform.[71,97]

With an alternative design approach, explorations of the PI-binding site of PI4K2A led to development of the allosteric thiourea-based inhibitor PI-273 **27**[98] (**Figure 18**), functioning as a PI-competitive substrate against this PI4K.[98]
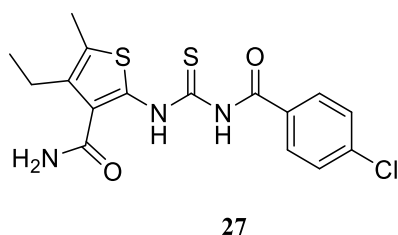
Figure 18. Structure of PI-273 **27**.

Interestingly, due to less conserved structural features present in the PI-binding sites of PI4Ks with respect to their ATP-binding sites, PI-273 **27** showed a marked selectivity for PI4K2A over other PI4Ks, even with respect to the closely related PI4K2B isoenzyme.[98]

As for PI4K2B, no isoform-specific inhibitors have yet been reported in the literature.

2.4. Aim of the PI4K class II inhibitors project

The overall goal of this project was to further previous efforts of Dr. Nencka's team that aimed at the development of novel type I inhibitors of class II PI4Ks (PI4K2A and PI4K2B) bearing selectivity over the class III isoforms.

The key objectives of the project were to:

- Design novel PI4K class II inhibitors based on structural analyses.
- Devise the synthesis of the designed compounds.
- Evaluate the molecules for activity and selectivity against PI4Ks.
- Investigate the binding mode of the molecules in complex with class II PI4Ks.
- Interpret structure/activity trends of the compounds that could enable their optimization.

All these research efforts were conducted in cooperation with various scientists, who I would like to acknowledge:

Dr. H. Mertlíková-Kaiserová's team (Biochemical Pharmacology, Institute of Organic Chemistry and Biochemistry, Czech Academy of Sciences, Prague, Czech Republic) conducted the enzymatic activity assays.

Dr. E. Boura's team (Structural biology, Institute of Organic Chemistry and Biochemistry, Czech Academy of Sciences, Prague, Czech Republic) provided the enzymes for the enzymatic activity assays and conducted the crystallography experiments.

2.5. Rational design of novel 4-aminoquinazoline PI4K class II inhibitors

This work was inspired by earlier structural biology studies that first led to significant insights into the tridimensional structure of PI4K2A in complex with the physiological substrate ATP **1**.[70] Further research endeavors led to confirm several structural/conformational points of similarities present in the class II PI4K isoforms' catalytic domains.[71] In addition, these research investigations led to identify MD59 **25** as a PI4K2A inhibitor featuring an ATP-competitive, type I binding mode and exhibiting good inhibition and selectivity against PI4K2A over the class III isoenzymes (i.e., PI4KB).[71] These insights overall could suggest that employing an adenine-mimicking central scaffold might lead to new inhibitors with appropriate affinity for PI4K2A and PI4K2B, and with good specificity over other PI4Ks.[71]

The rational approach employed to design new molecules began with structural analyses of analogous features of various known adenine-based ligands and their co-crystal structures in

complex with class II PI4Ks. Specifically, two structures of PI4K2A in complex with either the ligand ATP **1** (PDB: 4PLA), or inhibitor MD59 **25** (PDB: 4YC4), were selected and overlaid for comparative analyses (**Figure 19**).[70,71]
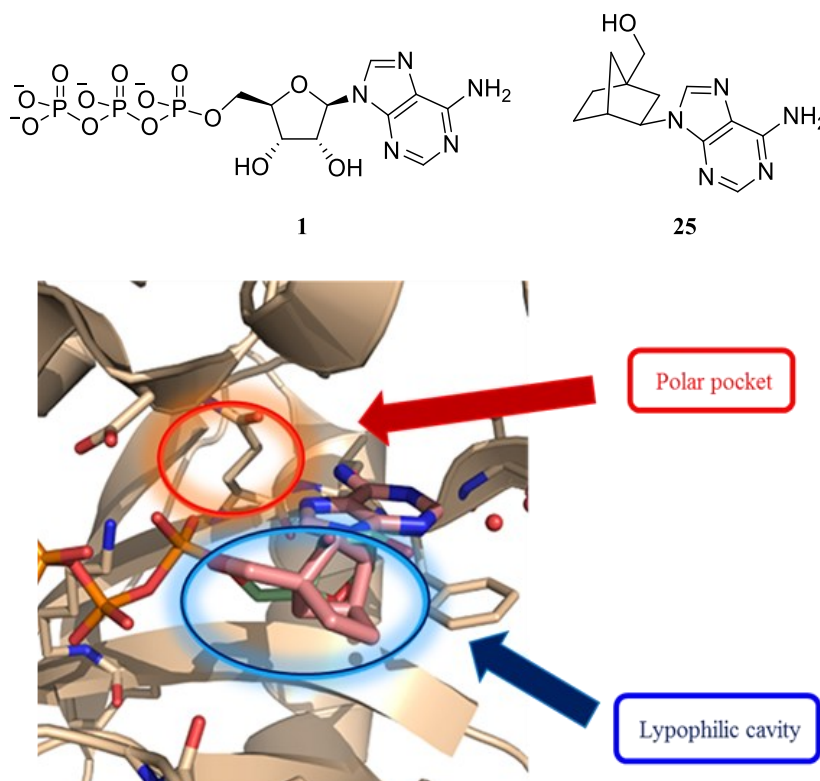
Figure 19. Structure overlay of ATP **1** and MD59 **25** in complex with PI4K2A (protein and ATP are from structure PDB: 4PLA[70], MD59 and water atoms are from structure PDB: 4YC4[71] – protein not shown). Blue circle depicts the region accommodating the norbornane system in MD59 **25**, or the ribose ring in ATP **1**. The red circle depicts an adjacent region that is free of any target/ligand contacts for both the substrates.

According to these evaluations, in the cases of both these adenine substrates, the imidazole of the scaffold lacks in any productive interactions with the ATP-binding site of PI4K2A, although several amino acids are localized near and around the nitrogen at position 7 of the purine (circled in red in **Figure 19**). Contrastingly, the nitrogens at positions 1 and 3 of the adenine, as well as the amino group at position 6, are all fundamental to engage in interactions with key amino acid residues in the hinge region, either through direct contacts, or through molecules of the solvent.[71] In addition, replacing a ribose moiety (in ATP **1**) with a norbornane system (in MD59 **25**) (circled in blue **Figure 19**) does not appear to interfere with the binding of the common adenine scaffold. In fact, the norbornane moiety of MD59 **25** seems to fit the sugar cavity of class II PI4Ks well and, possibly, might even contribute to the selectivity with respect to class III PI4Ks (PI4KA and PI4KB).[71] This may imply that the regions accommodating the ribose of ATP **1** might be intrinsically more lipophilic in class II PI4Ks, than in the class III isoenzymes. Nevertheless, considering the inhibitor MD59 **25**, a

decorative hydroxymethyl group on the norbornane system seems essential, as this might enable to get in contact with hydrophilic amino acid residues of these enzymes (e.g., Asp346 of PI4K2A) that, under physiological conditions, would interact with the triphosphate portion of ATP **1** (**Figure 20**).[70,71]

1 **25**
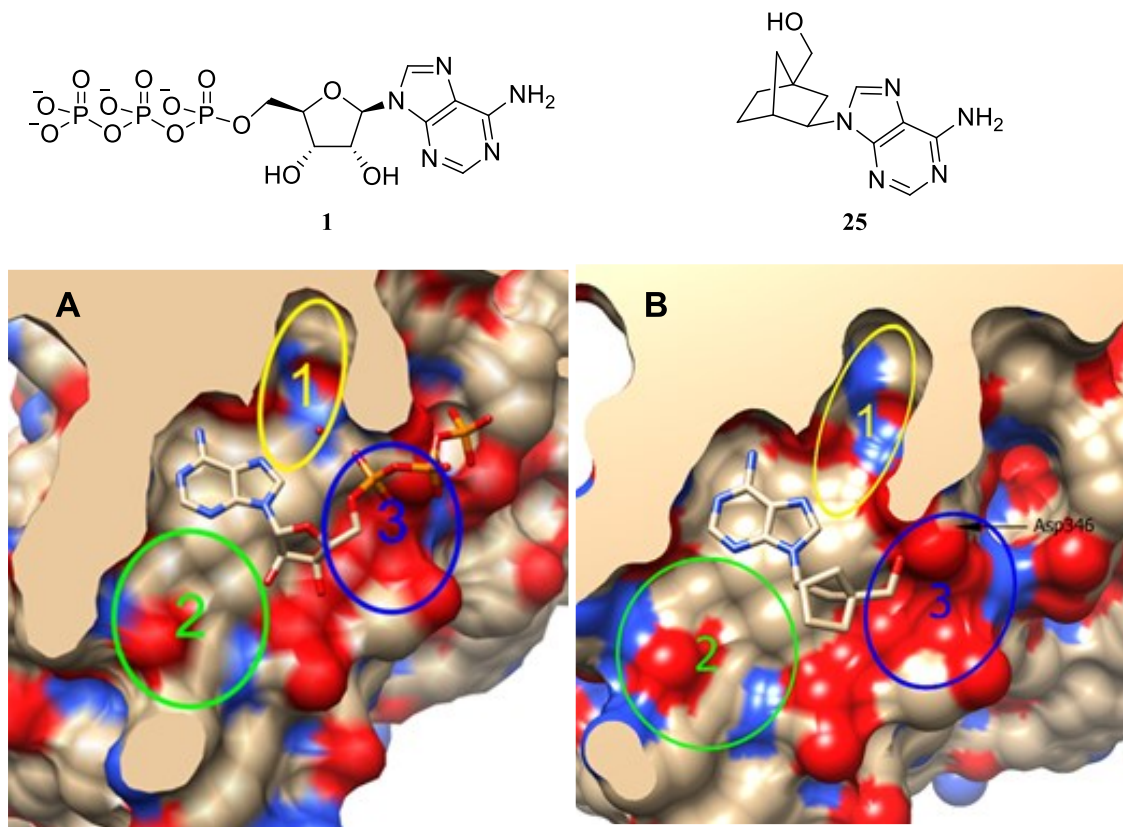
Figure 20. Models of ATP **1** (A) and MD59 **25** (B) in complex with PI4K2A, according to their respective co-crystal structures (PDB: 4PLA and PDB: 4YC4, respectively).[70,71] The authors highlighted three regions (yellow 1, green 2 and blue 3) within the ATP-binding site that could lead to inhibitor optimizations.[70,71]

All these structural observations enabled the elaboration of new molecular modelling experiments, which were conducted by Dr. Nencka employing principally a PI4K2A structure (PDB: 4PLA[70], **Figure 21**).

In the design of novel inhibitors of class II PI4Ks, it was first decided to implement a scaffold hopping strategy from an adenine to a 4-aminoquinazoline bicycle, considering this heterocycle could allow to retain the important interactions that both compounds ATP **1** and MD59 **25** can engage in the hinge region of the PI4K2A enzyme. Subsequently, a primary amide group was introduced at position 6 of the quinazoline, with the intent to extend the hydrogen bond interactions of the new compounds to hydrophilic amino acid residues that are localized proximally to the adenine-binding site of the enzyme, as, for instance, Asp346.[71] In addition, with the goal to find efficient bioisosteric replacements for the norbornane part of MD59 **25**, or the ribose of ATP **1**, extensive structure-activity relationship (SAR)

investigations were pursued to explore the sugar pocket of the PI4K2A ATP-binding site. To this end, modifications of various sizes and polarities were introduced at position 7 of the quinazoline, including monocyclic and bicyclic aryl, or heteroaryl moieties.
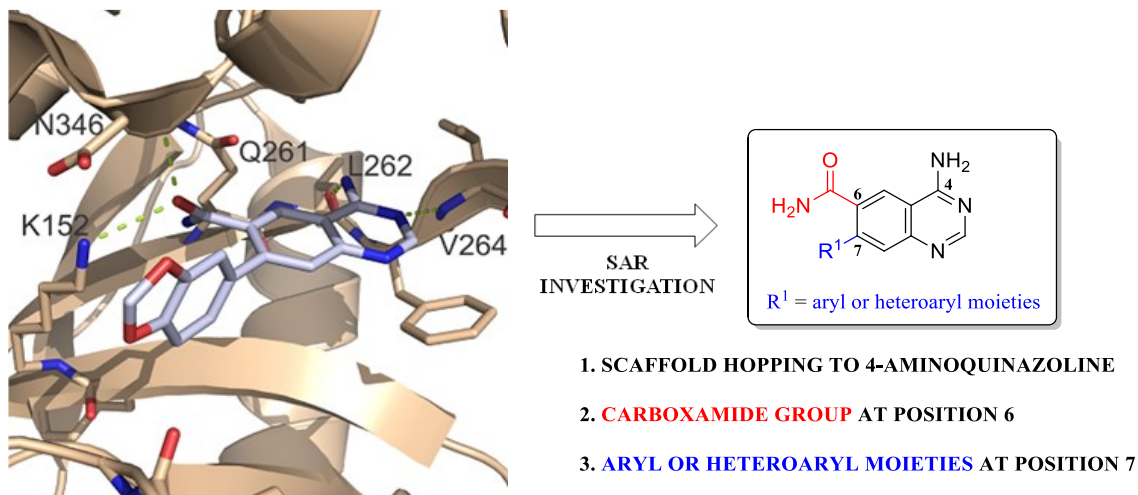
Figure 21. Example of a compound designed by docking in complex with PI4K2A (PDB: 4PLA)[70] and general structure of the new 7-substituted 4-aminoquinazoline-6-carboxamide series.

2.6. Rationale behind the synthesis of the compounds – literature precedents of one-pot cyclization approaches to 4-aminopyrimidine-fused heterocycles

The research program proceeded with a literary exploration of approaches useful for the synthesis of the compounds.

Due to a vast range of biological properties and activities, molecules bearing a 4-aminoquinazoline scaffold have been broadly explored by the scientific community.[99,100] Thus, various synthetic approaches are available in the literature for their preparation.[100,101] Particularly inspirational to this project was the synthetic methodology devised by Rad-Moghadam and Samavi[102], which is among the first ones to report an efficient, one-pot three-component synthesis of quinazoline compounds bearing a primary amino group at position 4 of the scaffold. Specifically, 2-aminobenzonitrile **28**, various triethyl orthoesters and ammonium acetate were combined under microwave-assisted, solventless conditions, affording the intended 2-substituted 4-aminoquinazoline products (general structure **29**) in 82–89 % yields (**Scheme 1**).[102]
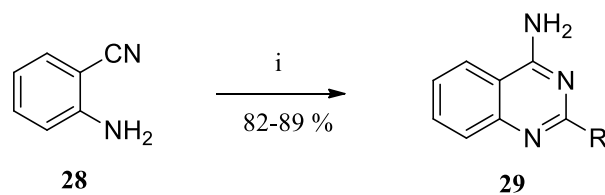
R = H or alkyl substituents

Scheme 1. Synthetic strategy leading to quinazolines bearing a primary amino group at position 4, devised by Rad-Moghadam and Samavi.[102] Reagents and conditions: (i) R-C(OEt)$_3$, ammonium acetate, microwave, 5-7 min.

This study showed for the first time that ammonium acetate can serve as a supplying synthon for the synthesis of 4-aminoquinazolines.[102] According to the mechanism proposed by Rad-Moghadam and Samavi (**Scheme 2**), ammonia, which is produced by decomposition of ammonium acetate under microwave irradiation, might react with 2-aminobenzonitrile **28** and a trialkyl orthoester, yielding amidine intermediate **30**. At this point, an intramolecular nucleophilic attack by the amidine amino group to the nitrile group might allow cyclization and formation of quinazolin-4(3H)-imine intermediate **31**. Lastly, the aromatic 4-aminoquinazoline products (general structure **29**) would be formed by favored tautomerization/aromatization.[102]

R = H or alkyl substituent   R = H or alkyl substituent
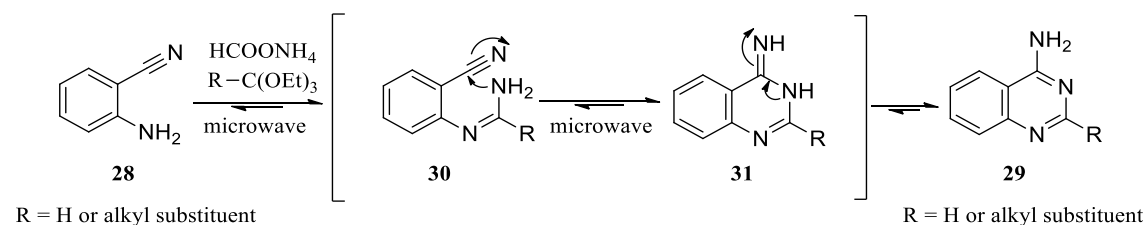
Scheme 2. Cyclization of 2-aminobenzonitrile to primary 4-aminoquinazolines, according to the mechanism proposed by the Rad-Moghadam and Samavi.[102]

Interestingly, in a more recent work, Lacbay et al.[103] demonstrated that the convergent approach employing ammonium acetate and substituted amidine may be pursued also for the synthesis of a 4-aminopyrimidine-fused bicyclic scaffolds other than 4-aminoquinazolines as, for instance, a pyrido[2,3-d]pyrimidin-4-amine heterocycle.[103] In this specific case, the cyclization of the fused-aminopyrimidine core appears to work well under heating and acidic conditions, without a need of microwave assistance. (**Scheme 3**).[103]

34
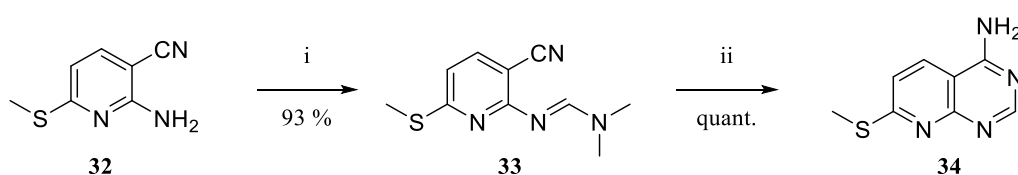
Scheme 3. Example of the Lacbay *et al.* strategy leading to a substituted pyrido[2,3-d]pyrimidin-4-amine core.[103] Reagents and conditions: (i) DMF-DMA, DMF, rt, 8 h; (ii) ammonium acetate, AcOH, 100 °C, 2 h.

The authors employed 2-aminonicotinonitrile **32** as a starting material, which yielded amidine derivative **33**. Preferentially, in alternative to an orthoester, *N,N*-dimethylformamide dimethyl acetal (DMF–DMA) was combined as a synthon in this first step. In the following cyclization step, the amidine intermediate was reacted in a solution of ammonium acetate in acetic acid under heating, which liberated the ammonia required for the formation of the intended product **34**.[103]

2.7. Synthesis of novel 4-aminoquinazoline PI4K class II inhibitors

Taking advantage of the knowledge in the available literature, I devised a modular sequence including six synthetic steps (**Scheme 4**) to prepare the selected 4-aminoquinazoline skeleton, obtaining a broad set of functionalized derivatives. Of note, the employed synthetic strategy offered a versatile opportunity to allow inversion of the order of the two final steps, which turned out to be useful to extend the series of final compounds. The general outline of the approach is depicted in **Scheme 4** and described below (see **Chapter 4**, **Section 4.1.** for the experimental procedures).
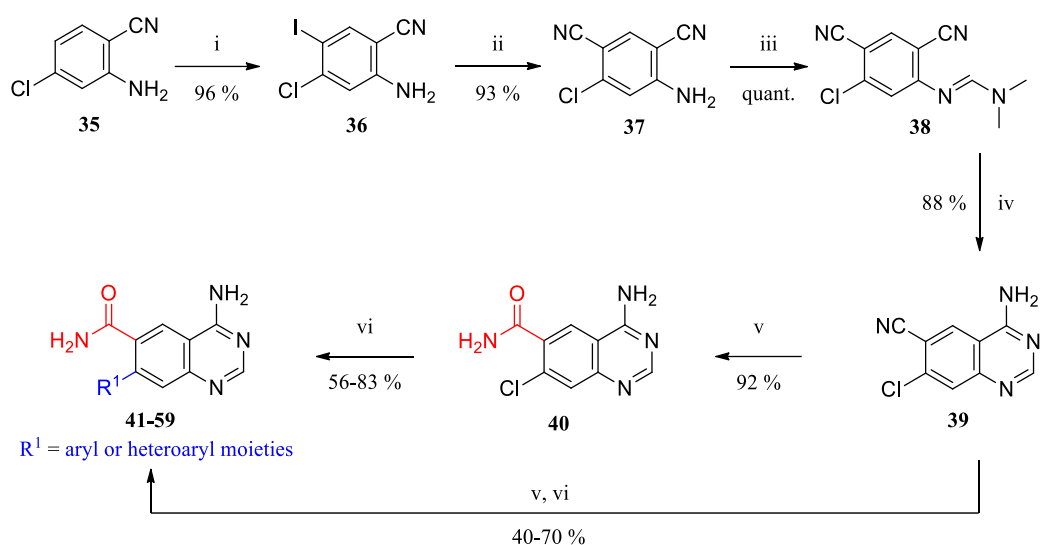
Scheme 4. Preparation of substituted primary 4-aminoquinazoline-6-carboxamide compounds **41–59**. Reagents and conditions: (i) NIS, DMF, rt, 48 h; (ii) CuCN, Pd$_2$(dba)$_3$, XantPhos, dioxane, 85 °C, 3 h; (iii) DMF-DMA, 95 °C, 1 h; (iv) NH$_4$OAc, AcOH, 95 °C, 2.5 h; (v) 1N NaOH, H$_2$O$_2$, EtOH:DMSO, rt, 1 h; (vi) R^1-B(OH)$_2$, K$_3$PO$_4$, Pd$_2$(dba)$_3$, SPhos, dioxane:H$_2$O, 95 °C, 24 h. For compounds **58** and **59**, NaBH$_4$, EtOH, rt, 55 min were included as the reagents and conditions employed in between the steps vi and v.

I selected aryl chloride **35** as a commercially available precursor to begin the synthesis of all the final compounds. In the first synthetic step, an electrophilic regioselective iodination at position 5 of **35** provided aryl halide **36** in 96 % yield. *N*-iodosuccinimide (NIS) in combination with a polar aprotic solvent (i.e., *N,N*-dimethylformamide, DMF) worked well as an iodinating system. Importantly, although NIS was used in excess, the iodine was installed suitably at the *para*-position with respect to the primary amino group of **35**, with only negligible introduction of the iodine at the *ortho*-position. In the second step, taking inspiration from a method developed by Sakamoto *et al.*[104], aryl halide intermediate **36** was subjected to a selective palladium-catalyzed cyanation to replace the iodine by a nitrile group, which provided isophthalonitrile **37** in 93 % yield. With respect to the approach by Sakamoto *et al.,* including tris(dibenzylideneacetone)dipalladium(0) (Pd$_2$(dba)$_3$) as a Pd(0) catalyst and

1,1′-bis(diphenylphosphino)ferrocene (DPPF) as a stabilizing ligand[104], in this reaction, Pd$_2$(dba)$_3$ was preferably combined with the ligand 4,5-bis(diphenylphosphino)-9,9-dimethylxanthene (XantPhos). In comparison with DPPF, employing XantPhos provided a significant improvement of the yield of the product. Copper(I) cyanide served as a cyanating agent. The synthesis proceeded by reacting isophtalonitrile **37** in neat DMF-DMA, which gave *N,N*-dimethylformimidamide **38** in quantitative yield. DMF-DMA was removed by rotary evaporation and no further purification was needed to continue with the next step. Intermediate **38** was treated with ammonium acetate in acetic acid under reflux, leading to cyclization and providing 4-aminoquinazoline **39**. At completion, a solid precipitated from the reaction mixture. The mixture was diluted with water and the product was collected in 88 % yield. I next chose to hydrolyze the carbonitrile of **39** employing common base-catalyzed conditions of sodium hydroxide and hydrogen peroxide, which led to rapid conversion into primary carboxamide **40** in 92 % yield. In the nitrile hydrolysis reaction, a combination of ethanol (EtOH) and dimethyl sulfoxide (DMSO) served to maximize the solubility of the reagents. This process was followed by rapid precipitation of a solid, which was collected and further purified by recrystallization from EtOH.

2.7.1. Synthesis of final compounds 41–50

Carboxamide **40** was reacted in a Suzuki coupling with multiple boronic acids and boronate ester substrates, which provided 4-aminoquinazoline compounds **41–50** (**Scheme 5**). In agreement with procedures suggested in the literature[105], various coupling substrates reacted well using a catalytic system of Pd$_2$(dba)$_3$ and the supporting ligand dicyclohexylphosphino-2′,6′-dimethoxybiphenyl (SPhos), affording the products in 56–83 % yields after purification.

R^1 =

41; 72 %

42; 81 %

43; 56 %

44; 63 %

45; 70 %

46; 75 %

47; 77 %

48; 83 %

49; 66 %

50; 73 %
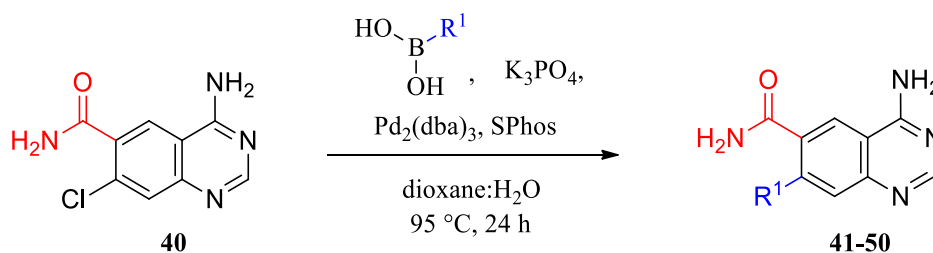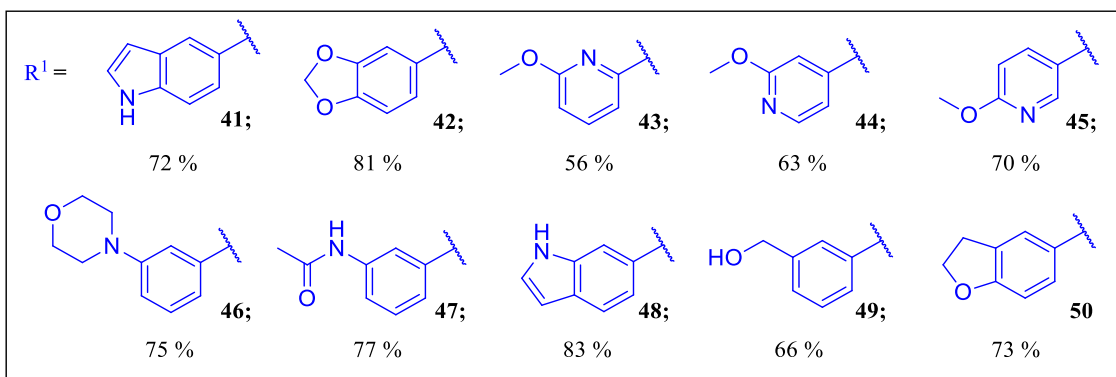
Scheme 5. Suzuki coupling leading to quinazoline compounds **41–50**.

Nevertheless, in the attempt to extend the series of compounds, some boronic acids and boronate esters appeared to react rather negligibly in the Suzuki coupling with carboxamide **40**.

2.7.2. Synthesis of final compounds 51–59

In alternative, the substrates that were unreactive in the Suzuki coupling with **40**, were satisfactorily coupled with carbonitrile **39** utilizing the same reaction conditions. Without a need for any purification, the carbonitrile group of each reaction intermediate was subsequently hydrolyzed to primary carboxamide under basic conditions by sodium hydroxide and hydrogen peroxide, giving 4-aminoquinazoline analogues **51–57** in 40–70 % overall yields (**Scheme 6**). A similar strategy was employed to prepare 4-aminoquinazoline analogues **58** and **59**. For these latter compounds, formylated substrates were employed in the Suzuki couplings; thus, requiring the additional reduction reactions of the formyl groups to hydroxymethyl groups. The reductions were performed before the hydrolysis of the nitrile intermediates, to prevent the oxidation of the formyl groups to carboxylic acids by hydrogen peroxide. Sodium borohydride in ethanol proved to be an efficient reducing system. The subsequent base-catalyzed hydrolysis of the nitrile intermediates led to the products, which were obtained in overall 40 and 52 % yields, respectively.

1) $\text{HO}-\text{B}(\text{OH})-\text{R}_1$, K$_3PO_4$, Pd$_2(dba)_3$, SPhos
dioxane:H$_2$O, 95 °C, 24 h

2) H$_2$O$_2$ 30%, NaOH 1N
EtOH:DMSO, rt, 1 h

39
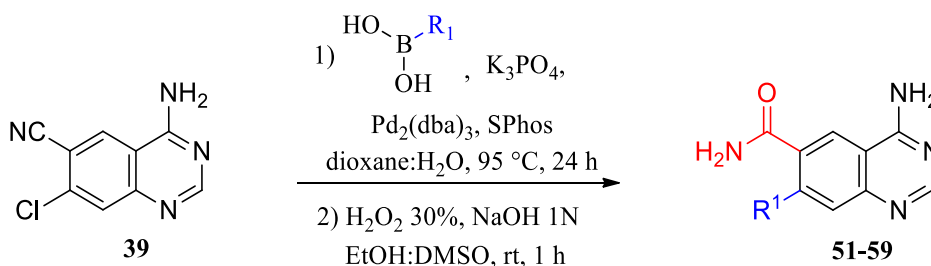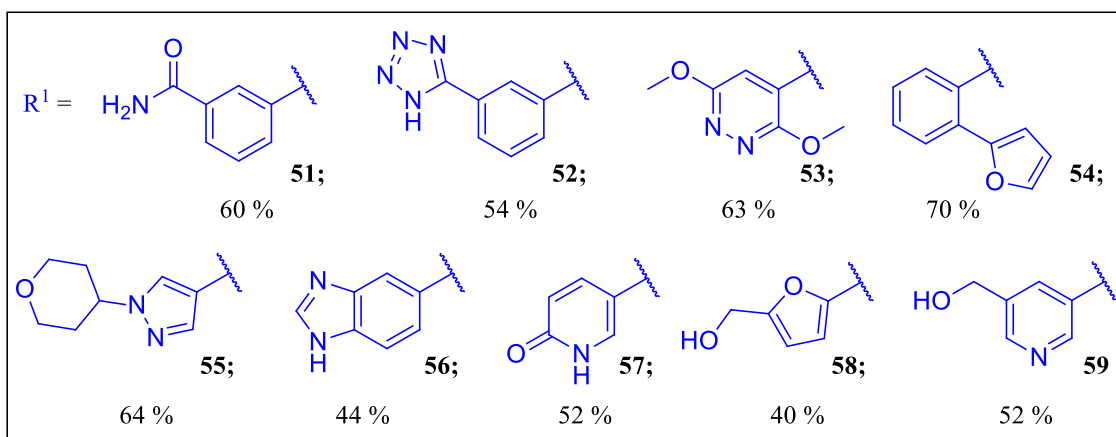
51-59

Scheme 6. Suzuki coupling (1) and hydrolysis of the carbonitrile group (2) leading to quinazoline compounds **51–59**. For **58** and **59**, $NaBH_4$, EtOH, rt, 55 min, were included as the reagents and conditions and employed in between the Suzuki coupling and the carbonitrile hydrolysis.
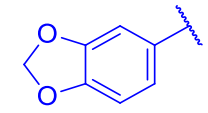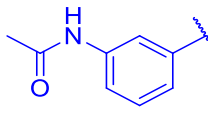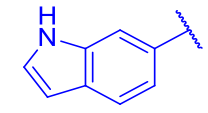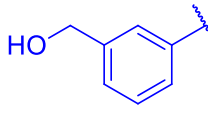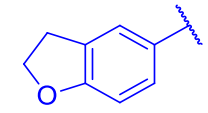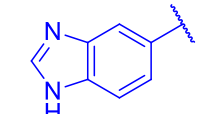
2.8. Biological results on activity and selectivity against the PI4K family

The prepared compounds were examined for activity and selectivity against PI4Ks (i.e., PI4K2A, PI4KA and PI4KB) in enzymatic ADP-Glo^{TM} (Promega) assays, which were previously standardized.[71,106] The enzymes used in these analyses were recombinant human PI4Ks, which were expressed in Sf9 cells. Phosphatidylinositol and phosphatidylserine were used as lipid substrates, whereas known PI4K inhibitors (MD59 **25**, NC02 **26** and wortmannin) served as positive controls.[71,97]

Percentage values of PI4K2A residual activity were first determined at a fixed concentration of the substrates (50 µM, data not shown). Exact half-maximal inhibitory values (IC$_{50}$) were later measured for compounds that inhibited PI4K2A below 50 %, at 50 µM concentration. The selectivity profiles of the compounds were subsequently investigated by measuring and comparing their IC$_{50}$ values against PI4KA and PI4KB. The overall data are reported in **Table 1**. Of note, in this primary evaluation, the activity against the isoenzyme PI4K2B was estimated to be reasonably comparable to the activity observed against PI4K2A, hypothesizing that the prepared molecules could bind to the homologous ATP-binding sites of class II PI4Ks with a traditional type I binding mode.[71]

Table 1. IC$_{50}$ values of selected compounds against PI4K2A, PI4KA and PI4KB *in vitro*.

Compound	R^1	PI4K2A IC$_{50}$ (µM)[a]	PI4KA IC$_{50}$ (µM)[a]	PI4KB IC$_{50}$ (µM)[a]
41		28.4 ± 5.1	>50	>50

42	benzo[d][1,3]dioxol-5-yl structure	20.8 ± 4.5	>50	>50
47	N-phenylacetamide structure	40.9 ± 5.6	>50	>50
48	1H-indol-6-yl structure	45.4 ± 6.4	>50	>50
49	(hydroxymethyl)phenyl structure	24.79 ± 7.8	>50	>50
50	2,3-dihydrobenzofuran-5-yl structure	44.2 ± 8.2	>50	>50
56	1H-benzo[d]imidazol-6-yl structure	12.2 ± 2.3	>50	38.6 ± 0.5
MD59 **25**	--	37.7 ± 7.6	>50	>50
NC02 **26**	--	1.46 ± 0.33	>50	>50
Wortmannin	--	>30	0.28 ± 0.06	0.44 ± 0.03

[a]Values are the mean of three experiments (± standard deviations).

Collectively, seven derivatives (**41**, **42**, **47–50** and **56**) exhibited IC_{50} values lower than 50 μM. Among these, compound **56** (IC_{50} = 12 μM) was identified as the lead inhibitor, exerting a threefold higher activity than inhibitor MD59 **25** (IC_{50} = 38 μM), which was previously selected as a structural model. Importantly, all the prepared molecules displayed a reasonable specificity for PI4K2A with respect to both PI4KA and PI4KB.

The empirical results might indicate that installing appropriate lipophilic moieties at position 7 (R^1) of the quinazoline core can positively modulate the potency and selectivity of the designed PI4K class II inhibitors. Interpreting the SAR of the molecules, those bearing fused bicyclic substituents at R^1 displayed higher potency than others of the series. Specifically, the presence of two heteroatoms in the decorative moieties conferred the highest affinities against PI4K2A. For instance, the derivative bearing a benzo[d][1,3]dioxol-5-yl (**42**) was found to be more active than its respective analogue bearing a 2,3-dihydrobenzofuran-5-yl substituent (**50**). Similarly, the compound bearing a 1*H*-benzo[d]imidazol-6-yl substituent (**56**) displayed higher activity than both the 1*H*-indolyl substituted derivatives (**41** and **48**). Presumably, the presence of two heteroatoms in the moieties of compounds **42** and **56** could enable to engage in more efficient contacts with amino acids that are localized in the sugar cavity of the PI4K2A ATP-binding site. In addition, replacing oxygen heteroatoms with nitrogens (NH) in the substituents at R^1 appeared to improve the potency of the molecules. For instance, compounds **42** and **50** were found to be weaker inhibitors than their analogues **56** and **41**,

respectively. This may indicate that amino groups may lead the molecules towards stronger binding affinities for PI4K2A, with respect to ethers. Furthermore, an appropriate distance of the amine nitrogen in the moieties at R^1 from the quinazoline scaffold seems to be relevant for activity, since the derivative **41** exhibited twofold higher potency than its constitutional isomer **48**, bearing only a distinct orientation of the indole substituent at R^1.

Interestingly, the SAR investigations also showed that, among compounds bearing at R^1 monocyclic aryl or heteroaryl moieties, only the 3-acetamidophenyl and the 3-hydroxymethylphenyl derivatives (**47** and **49**, respectively) were able to exert IC_{50} lower than 50 μM against PI4K2A. Compared with compound **49** ($IC_{50} = 25$ μM), direct analogues as **58** and **59**, bearing at R^1 decorated heterocyclic moieties that are more polar, both exerted a considerably weaker PI4K2A inhibition ($IC_{50} \geq 50$ μM). This could further indicate that the class II PI4K cavities interacting physiologically with the ribose of ATP **1** might inherently favor the binding of hydrophobic moieties that are appropriately decorated, as it can be observed in the case of the norbornane system of inhibitor MD59 **25**.[71]

2.9. Experimental validation of the binding mode of the novel PI4K class II inhibitors

The binding modality adopted by the molecules within the selected PI4K targets was investigated by X-ray crystallography employing some of the lead compounds (**56**, **42** and **49**). Co-crystallization experiments were conducted with both the human PI4K2A and PI4K2B isoenzymes, providing a structure of the target/ligand complex PI4K2B/**49** (see **Chapter 4**, **Section 4.2.** for the experimental procedures).

The structure of the complex enabled to empirically verify the binding mode of **49** within the ATP pocket of PI4K2B. Importantly, this highly resembles the pose of its docking model, which was designed through calculations employing a PI4K2A structure (**Figure 22**).
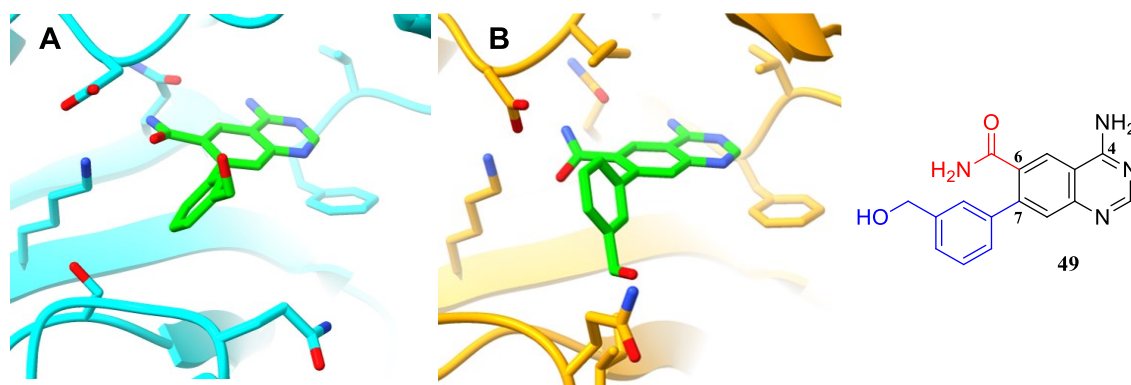
Figure 22. Docking model (A) and co-crystal structure (B) of **49** in complex with PI4K2A and PI4K2B, respectively. PI4K2A is from PDB: 4PLA.[70]

The structural elements shared between the kinase domains of class II PI4Ks are put well in evidence by superposition of the PI4K2B/**49** complex and the PI4K2A structure utilized for the docking (**Figure 23**). In a focused view of the superposed ATP-binding sites of the two proteins, a great majority of the key amino acid residues are appropriately aligned.
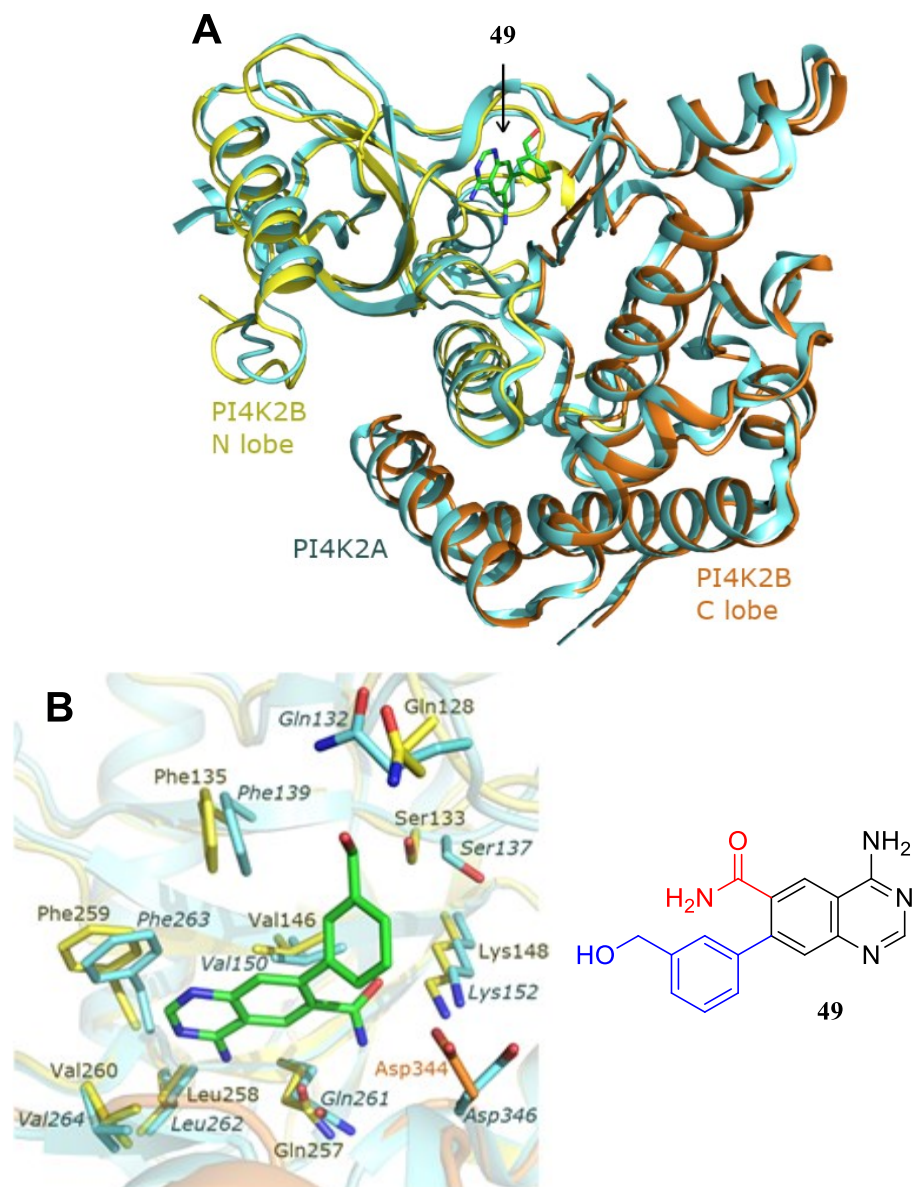
Figure 23. Structural superposition of the PI4K2B/**49** complex and PI4K2A (PDB: 4PLA[70]). (A) Full view of the kinase domains of the proteins (PI4K2B is colored in yellow and orange while PI4K2A is colored in light blue); (B) Focused view of the ATP binding sites of the proteins depicted with the previous color assignment.

This analysis therefore demonstrated that **49** can interact with class II PI4Ks by adopting the expected ATP-competitive, type I binding mode. In line with the docking predictions, the aminopyrimidine moiety of the quinazoline core mimics the interactions of the adenine scaffold of ATP **1** and MD59 **25** with the enzyme targets. Specifically, the 4-

aminoquinazoline scaffold forms at least three hydrogen bonds in the ATP-binding site of PI4K2B (**Figure 24**).
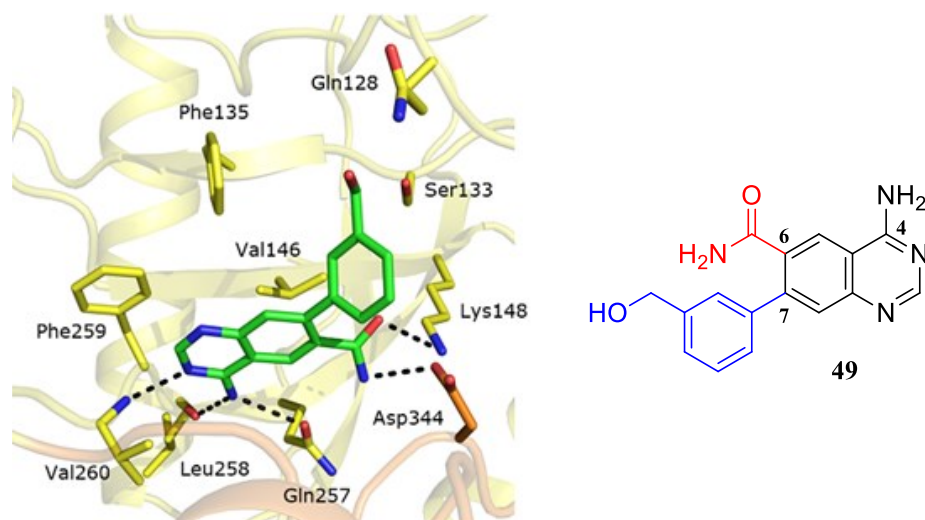
Figure 24. Focused view of **49** in complex with the PI4K2B kinase domain. The target/ligand hydrogen bond contacts are highlighted as black dashed lines.

The nitrogen at position 3 of the quinazoline interacts with the backbone amino group of Val260, while the primary amino group at position 4 can engage in two interactions with the backbone oxygen of Leu258 and the oxygen of the sidechain amide group of Gln257. In addition, the primary carboxamide group at position 6 of the quinazoline enables to engage in hydrogen bonds with the carboxylate and the primary amino groups on the side chains of the residues Asp344 and Lys148, respectively. Lastly, the decorated aryl moiety at position 7 of the quinazoline is projected towards the sugar cavity of the ATP-binding site of PI4K2B, which, in the case of ATP **1** and MD59 **25**, might be similarly occupied by either the ribose or the norbornane moiety, respectively.

These structural data fully support the logic behind designing the new compounds.

2.10. Summary and conclusions

The study detailed above was aimed to discover novel potential inhibitors of class II PI4Ks (PI4K2A and PI4K2B), evaluating their inhibitory efficiency with respect to class III PI4Ks (PI4KA and PI4KB). The structure-based approach applied to obtain new compounds, initially focused on structural analyses of the conserved binding modes of known adenine-based ligands (i.e., ATP **1**, or inhibitor MD59 **25**) in complex with PI4K2A. Secondly, docking and modelling experiments were performed with a PI4K2A crystal structure in complex with a 4-aminoquinazoline scaffold. This was intended as a suitable bioisosteric replacement for the adenine core of the above mentioned PI4K substrates. Subsequently, a primary carboxamide group was installed at position 6 of the quinazoline, while a broad SAR exploration of aryl and heteroaryl moieties of variable sizes and polarities was conducted at position 7. A devised six-step modular synthetic methodology enabled an easy access to the 4-aminoquinazoline skeleton and its diversifications. The new molecules were evaluated for inhibitory activity and selectivity across human PI4Ks (i.e., PI4K2A, PI4KA and PI4KB). Several compounds (**41**, **42**, **47–50** and **56**) exhibited good potency against PI4K2A. These also showed the desired selectivity profiles over class III PI4Ks. The lead compound **56** markedly outperformed the inhibitor MD59 **25** (IC_{50} = 12 *vs* 38 μM). Ultimately, **49**, selected among the best compounds, was successfully co-crystallized in complex with PI4K2B, showing that the functional binding mode of the molecules within the highly conserved kinase domains of class II PI4Ks fits well with the pose that was envisioned by docking experiments. Thus, the results of this work show that modifying position 7 of the designed 4-aminoquinazoline-6-carboxamide scaffold can result in an efficient starting strategy to obtain inhibitors of class II PI4Ks. Future optimizations and investigations of such chemical tools might be helpful to get detailed insight on the roles of these lipid kinases in cellular systems.

CHAPTER 3

3.1. Introduction to RIPKs

Based on analogies in their sequence, constructs, and functional target-specificities, human RIPKs have been classified as a subset of seven interrelated enzymes (RIPK1-7) acting as serine/threonine and/or tyrosine kinase-like kinases (**Figure 25**).[107,108]

L-serine   ATP   ADP   **phosphorylated L-serine**
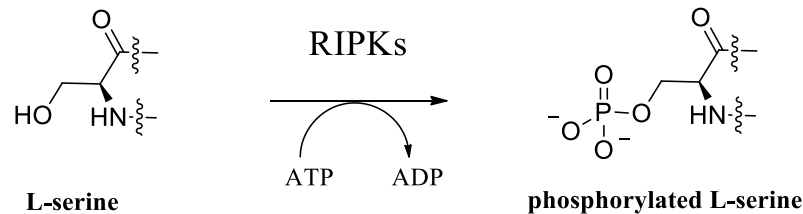
Figure 25. RIPK catalytic transfer of a phosphoryl group on the side chain of the amino acid L-serine. The same reaction may be performed with the amino acids L-threonine and L-tyrosine.

RIPKs are widely expressed and distributed at a subcellular level, where they function primarily as key protein regulators of innate immunity, programmed death and pro-inflammatory signaling processes.[109–111] According to genetic and structural characterizations, these kinases are known to share conserved elements in their catalytic domains. Nevertheless, their C- and N-terminal parts can bear dissimilar allosteric regions, enabling individual mechanisms of activation and functionalities that can be isoform-specific (**Figure 26**).[107,112]
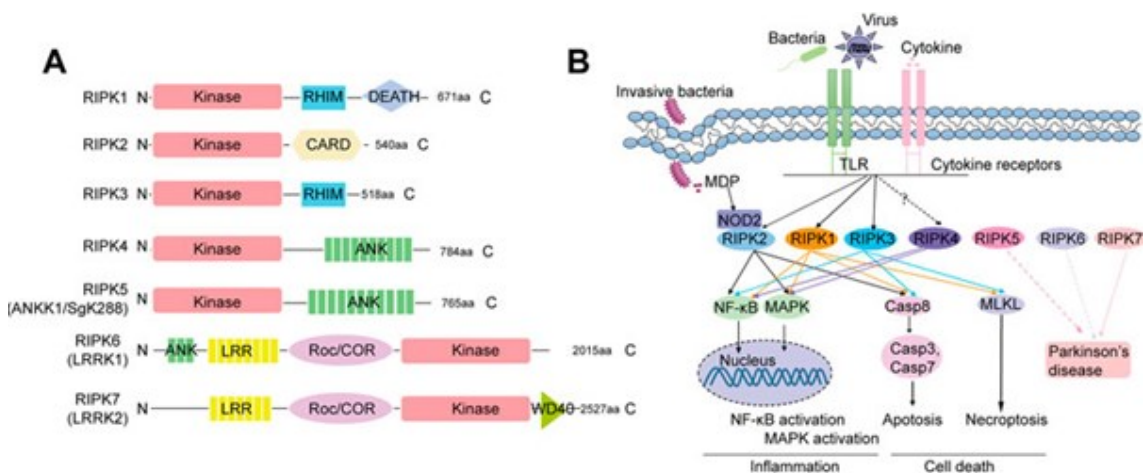
Figure 26. Structure organization (A) and signaling pathways (B) of human RIPKs.[112]

RIPK1 is featured by both a death domain and a receptor homotypic interaction motif (RHIM). These protein regions enable the modulation of cell death pathways, as apoptosis and necroptosis, as well as mitogen-activated protein kinase (MAPK) and nuclear factor kappa-light-chain-enhancer of activated B cells (NF-κB) pro-inflammatory cascades.[113,114]

RIPK2 bears a distinctive caspase activation and recruitment domain (CARD), which allows contacts with, and transduction of signals from, the upstream nucleotide-binding oligomerization domain-containing proteins 1/2 (NOD1 and NOD2, NOD1/2). In this way, RIPK2 can contribute to the regulation of the downstream MAPK and NF-κB pathways.[115] Recent studies have showed that RIPK2 is also implicated in apoptosis, whereas a direct correlation with necroptosis was not reported for this enzyme.[116]

RIPK3 contains a RHIM, as RIPK1, which links it primarily to necroptosis and apoptosis.[117] RIPK4 and RIPK5 are featured specifically by ankyrin-rich repeats in their encoded genes and seem to be implicated mainly in the NF-κB, MAPK and correlated apoptotic pathways.[118,119]

Lastly, RIPK6 and RIPK7, which share specific leucine-rich repeats and Ras of complex proteins/C-terminus of Roc domains, also appear to be involved in inflammation and host-immunity.[120] Both these latter enzymes exhibit some degree of dissimilarity from RIPK1-5 and their mechanisms of function have been less investigated thus far.[112]

3.2. RIPK2 and RIPK3 as potential therapeutic targets

In recent research studies, dysregulated expressions and activities of RIPK2 and RIPK3 have been proposed to be implicated in infectious, neurological, inflammatory, oncological, and immunological disorders.[109,121,122]

RIPK2 is prominently involved in host-immunity and inflammatory events correlated with infections by bacteria as well as by other pathogens (**Figure 27**).[115,123]
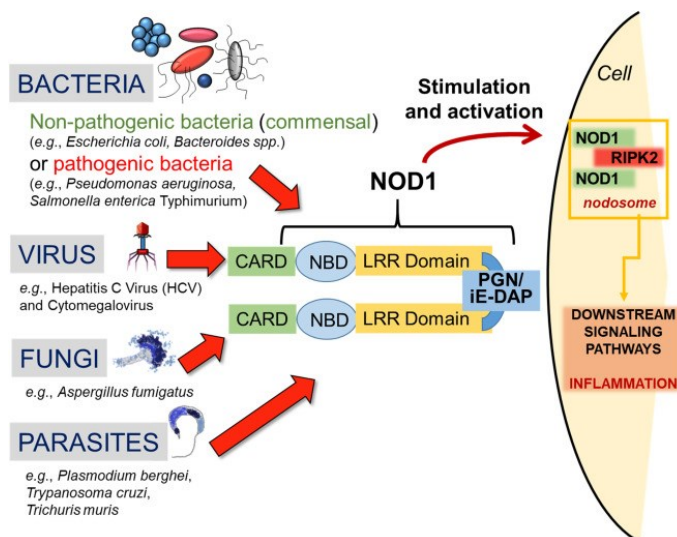

Figure 27. Schematic representation of pathogen activators of the NOD1-RIPK2 pro-inflammatory pathway.[123]

Its recruitment is known to be primarily mediated by formation of complexes with CARD-containing proteins, such as NOD1/2, which are cytosolic receptors responsible for the recognition of the invading microbes.[116,123–125]

Upon stimulation by NOD1/2, RIPK2 can perform auto-phosphorylation, which is followed by ubiquitination by E3 ubiquitin-conjugating enzymes, including X-linked inhibitor of apoptosis protein (XIAP), c-IAPs and the linear ubiquitin chain assembly complex (LUBAC).[124,125] In turn, RIPK2 can mediate the downstream bioactivities of transcription factors and protein kinases (i.e., NF-κB and MAPKs, respectively), which are involved in enzymatic processes contributing to production of pro-inflammatory agents (i.e., chemokines and cytokines).[124,126]

The RIPK3 activity has been predominantly associated to cell death events as necroptosis and apoptosis, which ultimately link it to inflammation and cancer.[117,127] RIPK3 is involved in the response to inflammatory stimuli elicited by cellular stress, pathogen infections, and tissue damage.[128,129]

Notably, in the process of necroptosis, RIPK3 can be recruited by its interrelated kinase RIPK1 through homotypic RHIM-RHIM interactions.[130] Under stimulation of tumor necrosis factor receptors (TNFRs) by TNF-α, RIPK1 and RIPK3 can reciprocally phosphorylate one another to form a death-promoting adduct. The RIPK1/RIPK3 adduct can induce the activation by phosphorylation of the molecular substrate - mixed lineage kinase domain-like pseudokinase (MLKL, **Figure 28**).[131,132]
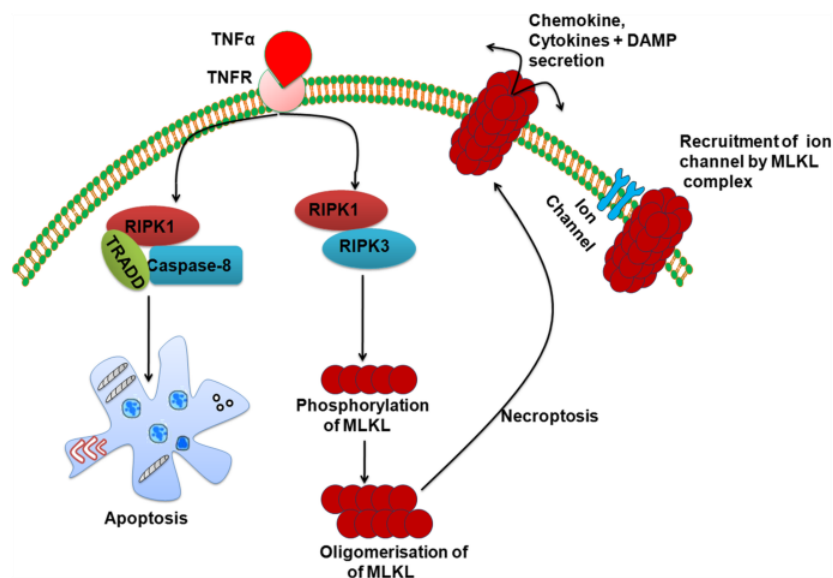
Figure 28. Schematic representation of the RIPK1/RIPK3-mediated molecular mechanisms of apoptosis and necroptosis.[132]

The following oligomerization of MLKL can lead towards the decomposition of the plasma membrane; therefore, cell death.[132] Necroptotic cells can finally spread pro-inflammatory signals over healthy cells by releasing toxic species, including chemokines, cytokines, and damage-associated molecular patterns (DAMPs).[133]

3.3. RIPK2 and RIPK3 inhibitors known in the literature

Exploring RIPK2 and RIPK3 as potential kinase targets for the treatment of human diseases has led to a discovery of an increasing variety of compounds as potent inhibitors of these RIPKs, both in enzymatic and in cellular assays.[134,135]

3.3.1. RIPK2 inhibitors

Small macrocyclic compounds such as OD36 **60** and OD38 **61**[136] (**Figure 29**), bearing a functionalized pyrazolo[1,5-*a*]pyrimidine or a imidazo[1,2-*b*]pyridazine heterocyclic structure, respectively, were identified among the pioneering RIPK2 selective inhibitors.
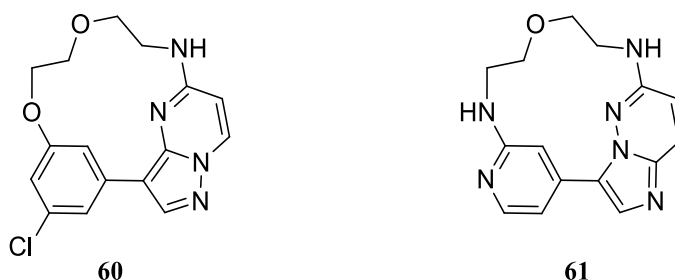
Figure 29. Structures of OD36 **60** and OD38 **61**.

Subsequently, inhibitor WEHI-345 **62**[137] was developed employing an adenine mimetic pyrazolo[3,4-*d*]pyrimidine central core (**Figure 30**). This molecule exhibited good cellular activity but poor pharmacokinetic properties, which disfavored a thorough evaluation for its safety profile.[137]
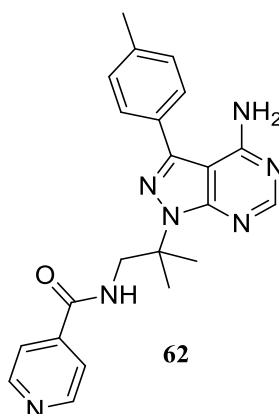
Figure 30. Structure of WEHI-345 **62**.

Quinoline-based inhibitor GSK583 **63**[138] and quinazoline-based inhibitor GSK2983559 **64**[139] (**Figure 31**), both designed and later developed by the GlaxoSmithKline company, displayed higher stability, as well as activity and kinome-wide specificity against RIPK2, compared to WEHI-345 **62**.[134,138,139]
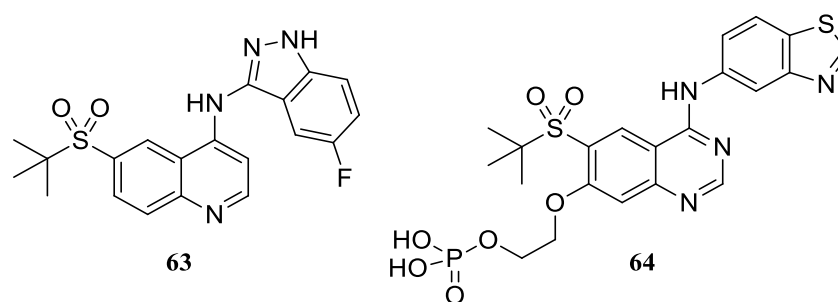
Figure 31. Structures of GSK583 **63** and GSK2983559 **64**.

As for GSK583 **63**, in preclinical evaluations for its safety, this compound exerted off-target inhibition of the potassium channel encoded by human *ether-à-go-go*-related gene (hERG), which disfavored it in further progressing as a drug candidate.[138] In contrast, GSK2983559 **64** reached a phase 1 clinical trial in humans (NCT03358407) for the treatment of inflammatory bowel disease (IBD).[139] Lastly, non-clinical results in toxicology studies showed a potential lack of safety required to proceed with this trial (NCT03358407).

Over the years, other potent and selective RIPK2 inhibitors were developed[140–144]; nevertheless, investigations on their clinical safety have not yet been reported in the literature.

3.3.2. RIPK3 inhibitors

Among the RIPK3 selective inhibitors discovered, illustrative examples are the inhibitors GSK843 **65**, GSK872 **66** and GSK840 **67**[145,146] (**Figure 32**), bearing a benzimidazole, a quinoline and a thieno[3,2-*c*]pyridine scaffold, respectively.
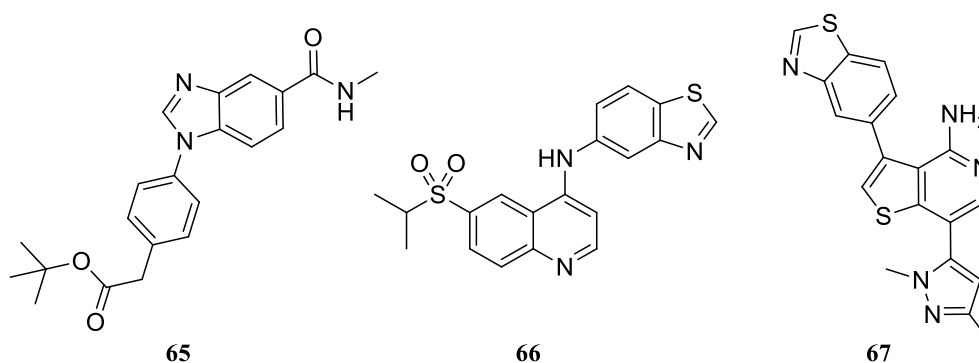
Figure 32. Structures of GSK843 **65**, GSK872 **66** and GSK840 **67**.

Inhibitor GSK872 **66** displayed striking potency against RIPK3 as well as selectivity over other kinases.[145] However, poor cell viability was exhibited over an exposure to increasing concentrations of this compound. These findings hindered its clinical evaluations against necroptosis related pathologies.[146] RIPK3 inhibitors as GW'39B **68**[147] and HS-1371 **69**[148]

(**Figure 33**), which are also based on a quinoline central scaffold, were later identified. Nevertheless, evaluations of the safety of these molecules were not disclosed.
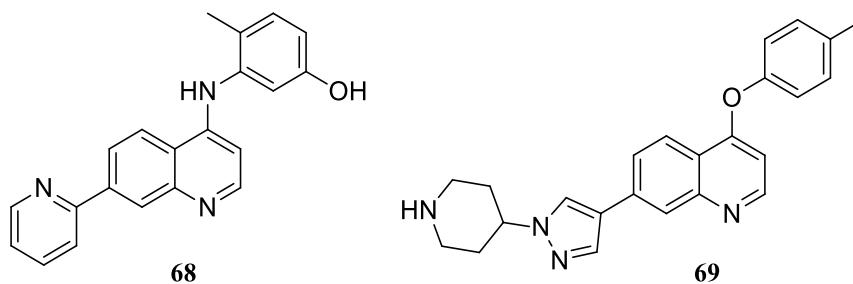
Figure 33. Structures of GW'39B **68** and HS-1371 **69**.

In more recent studies, several other RIPK3 inhibitors based on a tricyclic thieno[2,3-*g*]quinoline 1,1-dioxide scaffold, as represented by Zharp-99 **70**[149] (**Figure 34**) and other interrelated compounds[150], were reported. However, these molecules were not subjected to any clinical evaluation.

Currently, no RIPK3 inhibitors have been fully assessed for their safety in the clinics.
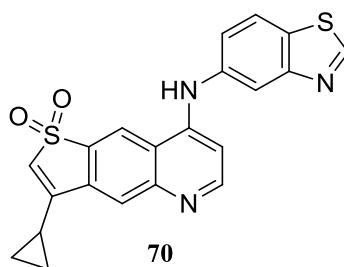
Figure 34. Structure of Zharp-99 **70**.

3.3.3. Multi-RIPK inhibitors

Employing drug repurposing approaches, some FDA approved kinase inhibitors, for instance the Bcr-Abl kinase inhibitor ponatinib **71**[151] (**Figure 35**), were also identified to exert inhibitory effects against RIPKs (i.e., RIPK1-3).
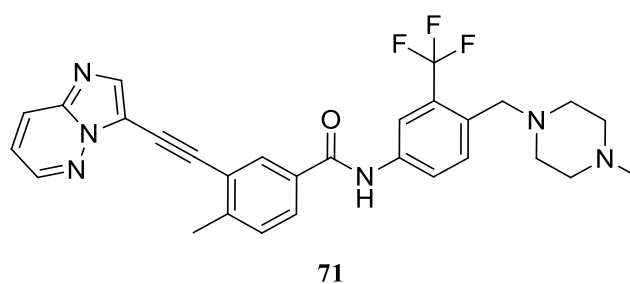
Figure 35. Structure of ponatinib **71**.

These findings led to the identification and development of new inhibitors and potential therapeutic strategies in targeting RIPKs. Recently, compound GSK074 **72**[152] (**Figure 36**) was developed as a selective dual-target inhibitor against both RIPK1 and RIPK3. This compound exhibited a limited cytotoxicity and was proposed as a potential treatment for necroptosis related diseases.[152]
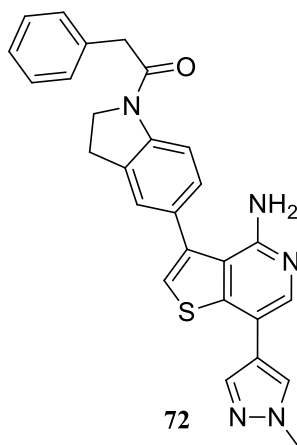
Figure 36. Structure of GSK074 **72**.

Similarly, the development of dual target RIPK2/3 specific inhibitors could provide promising therapeutic strategies against pathologies that are linked with both programmed cell death and NOD-dependent inflammation.[153] Nevertheless, these compounds have yet to be identified and explored for their efficiency and safety.

3.4. Aim of the RIPK2/3 kinase inhibitors project

The primary goal of this project was to design and prepare novel compounds employing a quinazoline scaffold, to explore their inhibitory activity and selectivity towards RIPK2/3 kinases over other interrelated RIPKs (i.e., RIPK1 and RIPK4). The plan included the introduction of extensive diversifications of positions 6 and 7 of the scaffold, assessing any potential modulations in the bioactivity of the new molecules against individual RIPKs.

The key objectives of the project were to:

- Design novel inhibitors of RIPK2/3 kinases based on structural analyses.
- Devise the synthesis of the designed compounds.
- Evaluate the molecules for activity and selectivity against a subset of selected RIPKs.
- Evaluate the metabolic stability of the molecules in various environments.
- Evaluate the selectivity of the lead compounds in a broad panel of kinases.
- Understand structure/activity trends of the new compounds that could enable their further optimization.

All these research efforts were conducted in cooperation with various scientists, who I would like to acknowledge:

Dr. H. Mertlíková-Kaiserová's team (Biochemical Pharmacology, Institute of Organic Chemistry and Biochemistry, Czech Academy of Sciences, Prague, Czech Republic) conducted the enzymatic and cellular activity assays, as well as the assessments of cytotoxicity and metabolic stability.

Dr. E. Boura's team (Structural biology, Institute of Organic Chemistry and Biochemistry, Czech Academy of Sciences, Prague, Czech Republic) conducted the expressions and purifications of the enzymes that were employed in the above-mentioned activity assays.

Eurofins lab scientists (CEREP SA laboratories, Celle-Lévescault, France) conducted the selectivity assays in a diversified kinase panel.

3.5. Rational design of novel quinazoline-based inhibitors of RIPK2/3 kinases

The rational strategy to design novel compounds began by analyzing structural similarities among previously investigated RIPK2 and RIPK3 inhibitors (i.e., GSK583 **63**, GSK2983559 **64** and GSK872 **66**).[138,139,145] These molecules all bear analogous quinoline and quinazoline scaffolds that enable a common ATP-competitive binding mode in complex with the kinase domains of RIPK2 and RIPK3.

On this basis, new docking experiments were conducted selecting a quinazoline scaffold and crystal structures of these two RIPKs (RIPK2 PDB: 6RNA[139] and RIPK3 PDB: 7MX3[154]).

To ensure data consistency, the modelling analyses were conducted in parallel by both K. Skach (colleague from Dr. Nencka's team) and Dr. Nencka, employing distinct software packages (see **Chapter 5**, **Section 5.2.** for the experimental procedures).

Taking inspiration from previous studies on RIPK inhibitors (i.e., GSK2983559 **64**, or GSK872 **66**)[139,145], an aminobenzothiazole substituent was first installed at position 4 of the quinazoline scaffold. According to the theoretical experiments that were conducted, this moiety could enable optimal interactions of the new molecules with amino acids of the ATP-binding pockets of both RIPK2 and RIPK3. This can partly suggest its contribution to the efficiency of the above-mentioned inhibitors and other related molecules against these RIPK isoenzymes.[139,143,145,149] As for position 6 of the quinazoline (R^1), various aryl or heteroaryl moieties were introduced as promising replacements for the alkyl sulfones of GSK2983559 **64** and GSK872 **66**. The docking suggested this specific position of the scaffold can be projected towards wide solvent-exposed cavities, enabling potential contacts of the new molecules with a variety of amino acids that can be situated within both RIPK2 and RIPK3. In parallel, position 7 of the quinazoline heterocycle was also diversified, considering that this might similarly provide further contacts with amino acids in the cavities of the enzymes. Specifically, a series of compounds that are chlorinated at this latter position of the scaffold (General structure A) was first devised, to probe their ability to interact with non-polar amino acids likely present in the ATP binding sites of the RIPKs examined. Subsequently, a reductive hydrodechlorination was planned to yield simplified molecules that do not display substitution at position 7 (General structure B). Alternatively, installing substituents of varying steric bulks and polarities at this position could provide an opportunity to explore other, more complex compounds (General structure C). To this end, aromatic, heteroaromatic and partially saturated heterocyclic moieties were further selected as diversifications of position 7 of the quinazoline (R^2), since, according to the docking analyses, both RIPK2 and RIPK3 seemed to tolerate wide changes in the size of the substituents that are added at this site of the compounds.

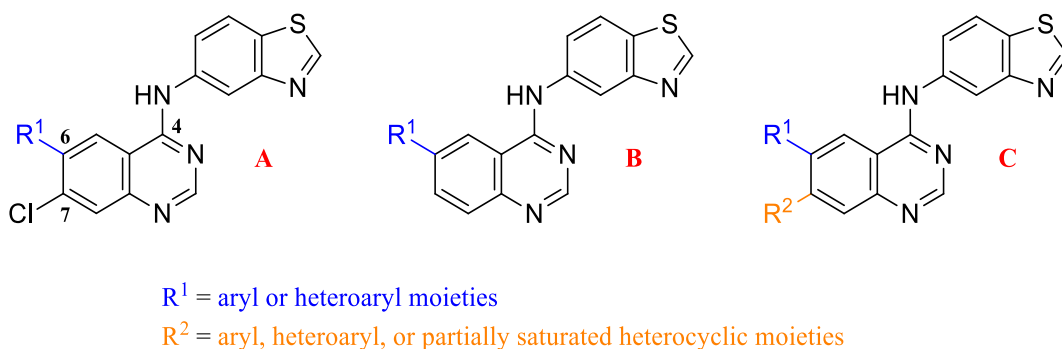The three compound series that were designed are illustrated in **Figure 37**.

R^1 = aryl or heteroaryl moieties
R^2 = aryl, heteroaryl, or partially saturated heterocyclic moieties

Figure 37. General structures of the series of quinazoline compounds designed in this study.

3.6. Rationale behind the synthesis of the compounds – literature precedents of one-pot convergent cyclization towards 4-*N*-substituted aminoquinazolines

The research program proceeded with a literary exploration of approaches useful for the synthesis of the compounds.

Historically, small molecules bearing 4-*N*-substituted aminoquinazoline scaffolds have displayed remarkable efficacy as inhibitors of the transmembrane kinase EGFR as well as other kinases; thus, they have been extensively synthesized.[100,155] My attention was drawn by the research work of Tsou *et al.*[156], who were among the first to report an efficient one-pot, two-step construction of 4-*N*-anilinoquinazoline derivatives. Their synthesis began with nitro-substituted 2-aminobenzonitrile **73**, which was initially reacted with DMF–DMA, giving substituted *N,N*-dimethyl formamidine **74** in 98 % yield. Intermediate **74**, in turn, was reacted with a substituted aniline under reflux in acidic conditions, leading to cyclization and providing the intended 4-*N*-anilinoquinazoline product **75** in 89 % yield (**Scheme 7**).[156]
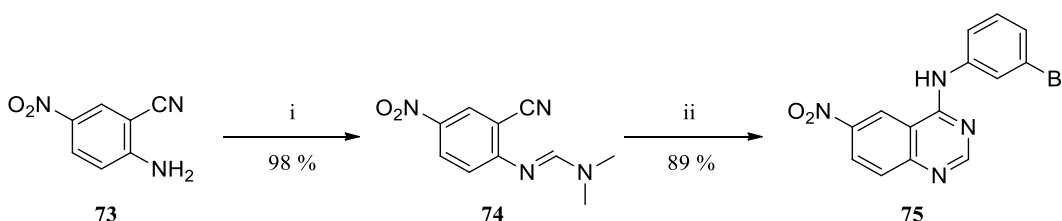
Scheme 7. Synthetic strategy leading to *N*-aryl substituted quinazoline by Tsou *et al.*[156] Reagents and conditions: (i) DMF-DMA, 100 °C, 1.5 h; (ii) 3-bromoaniline, AcOH, reflux, 1 h.

Yoon *et al.*[157] later employed an analogous convergent methodology to obtain diverse 4-*N*-substituted aminoquinazolines. The authors employed *N,N*-dimethyl formamidine **76** as a starting material. This was reacted with substituted amine substrates under microwave-assisted conditions obtaining products such as **77–79** in 92–94 % yields (**Scheme 8**).[157]

Considering that the starting *N,N*-dimethyl formamidine **76** was combined with various aryl- and alkyl-substituted amines, the Yoon *et al.* research work showed a wider scope of the cyclization reactions leading to 4-*N*-substituted aminoquinazolines.[157]
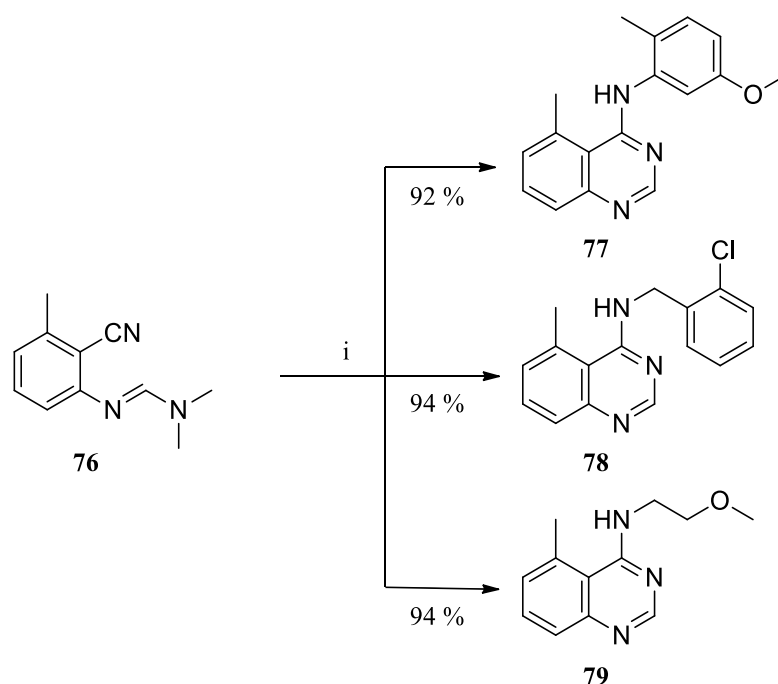
Scheme 8. Synthetic strategy leading to 4-*N*-substituted aminoquinazolines by Yoon *et al.*[157] Reagents and conditions: (i) aryl or alkyl substituted amines, acetonitrile:AcOH, microwave, 160 °C, 10 min.

Cyclization reactions from substituted amidines (general structure **80**) to 4-*N*-substituted aminoquinazolines were later employed also by Chandregowda *et al.*[158] to devise a cost-effective, multigram-scale approach for the preparation of the EGFR inhibitors gefitinib **6** and erlotinib **7** (**Scheme 9**).
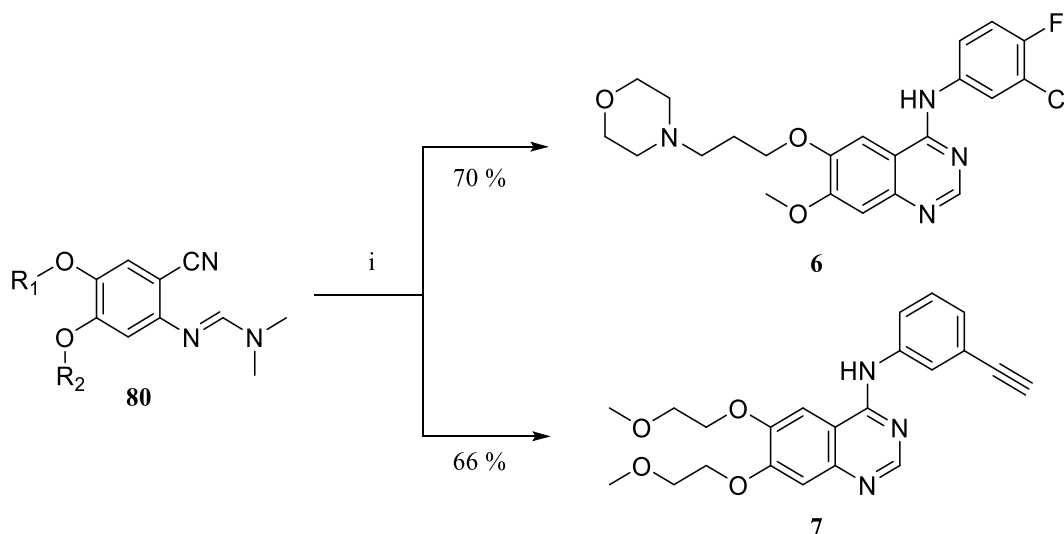
Scheme 9. Synthetic strategy leading to gefitinib **6** and erlotinib **7** by Chandregowda *et al.*[158] Reagents and conditions: (i) substituted aryl amines, AcOH, 130 °C, 3 h.

According to Chandregowda *et al.*, who proposed a general mechanism of the cyclization reaction, the formation of the 4-*N*-substituted aminoquinazoline scaffold could involve a Dimroth rearrangement, with a relocation of endocyclic and exocyclic nitrogen heteroatoms of the fused pyrimidine ring, achieved by its opening and reclosure.[158,159] The overall proposed mechanism of the cyclization reactions is schematically illustrated in **Scheme 10**.
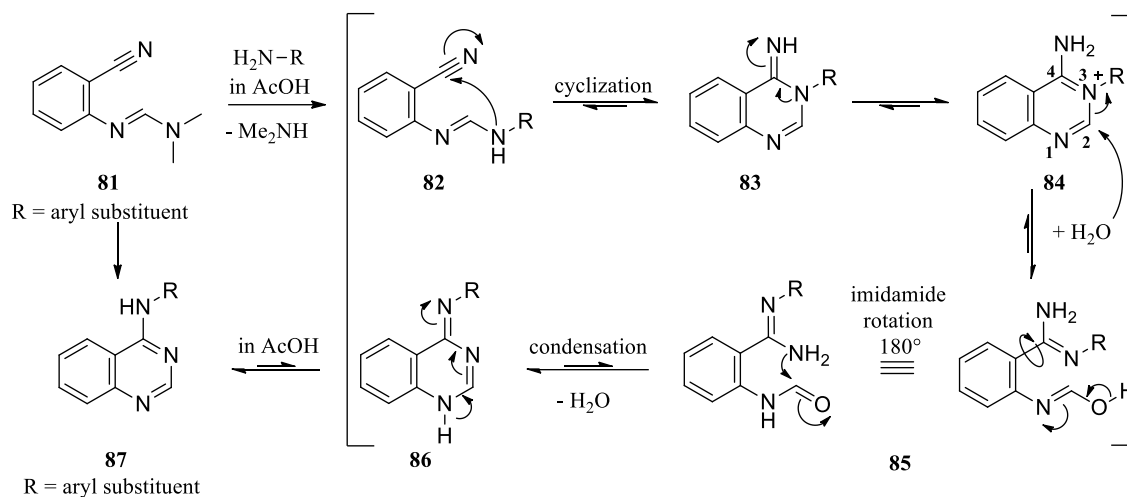
Scheme 10. Cyclization of *N,N*-dimethyl formamidine to quinazoline *via* the Dimroth rearrangement, according to the mechanism proposed by Chandregowda *et al.*[158]

Under acidic conditions, the tertiary dimethelylamino group of a *N,N*-dimethyl formamidine precursor, such as **81**, is likely replaced for a secondary amino group in an initial addition-elimination reaction with a primary amine substrate, giving amidine intermediate **82**. In turn, amidine intermediate **82** can undergo a favored, intramolecular ring closure into substituted quinazolin-4(3*H*)-imine intermediate **83**, which can be protonated and converted into **84**. A subsequent nucleophilic attack by water, generally added during the reaction work-up, may hydrolyze intermediate **84** in between the carbon at position 2 and the nitrogen at position 3 of the scaffold, giving intermediate **85** after ring opening. The rotation of the resulting imidamide group by 180° can enable the condensation with the unsubstituted nitrogen, providing intermediate **86**. Lastly, tautomerization/aromatization would lead to the more stable quinazoline product **87**.[158]

3.7. Synthesis of quinazoline-based inhibitors of RIPK2/3 kinases

Encouraged by the simplicity and efficiency of the synthetic approaches illustrated above, I devised a similar convergent synthetic strategy, *via* a Dimroth rearrangement, to construct quinazoline analogues bearing a 5-aminobenzothiazole moiety at position 4 of the scaffold. Diversifications of positions 6 and 7 of the quinazoline core were performed employing palladium-catalyzed methods, including the Stille coupling[160], the Suzuki coupling[105] and the reductive hydrodechlorination reactions.[161]

The overall approaches employed to obtain the molecules are depicted in **Scheme 11** and **Scheme 12**, which are discussed below in detail (see **Chapter 5**, **Section 5.1.** for the experimental procedures). Of note, following a synthetic method established during the preparation of the previously described quinazoline PI4K class II inhibitors, I decided to begin the synthesis of all the compounds by reacting commercially available aryl halide **35** with NIS, obtaining intermediate aryl halide **36** in high yield.
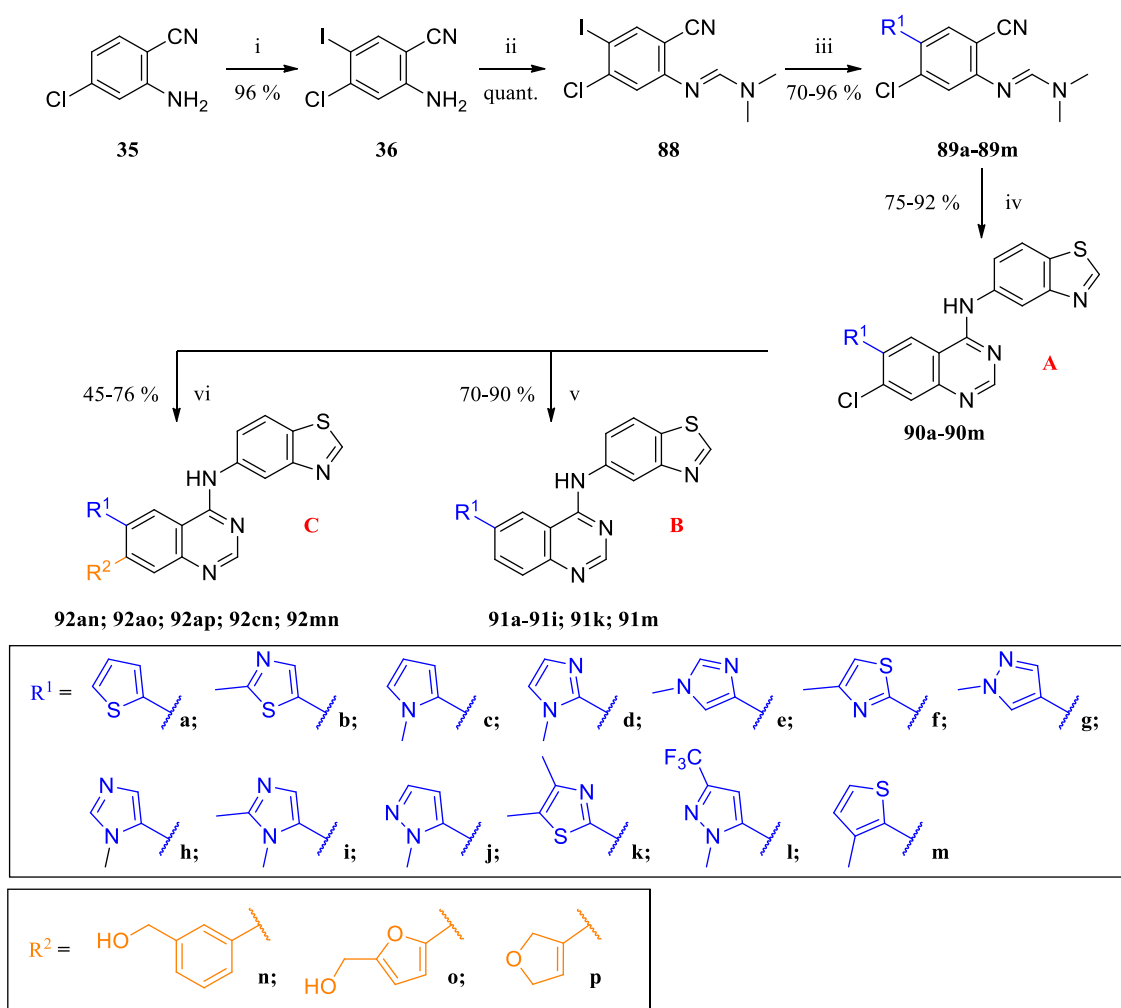
Scheme 11. Synthesis of the series of compounds with the general structures **A**, **B** and **C**. Reagents and conditions: (i) NIS, DMF, rt, 48 h; (ii) DMF-DMA, 95 °C, 1 h; (iii) R^1-Sn(Bu)$_3$, PdCl$_2$(PPh$_3$)$_2$, LiCl, anhydrous dioxane, 95 °C, 24 h; (iv) 5-aminobentzothiazole, AcOH, 95 °C, 1 h; (v)

HCOONH$_4$, Pd$_2$(dba)$_3$, SPhos, dioxane:H$_2$O, 95 °C, 24 h; (vi) R^2-B(OH)$_2$, K$_3$PO$_4$, Pd$_2$(dba)$_3$, SPhos, dioxane:H$_2$O, 95 °C, 24 h.
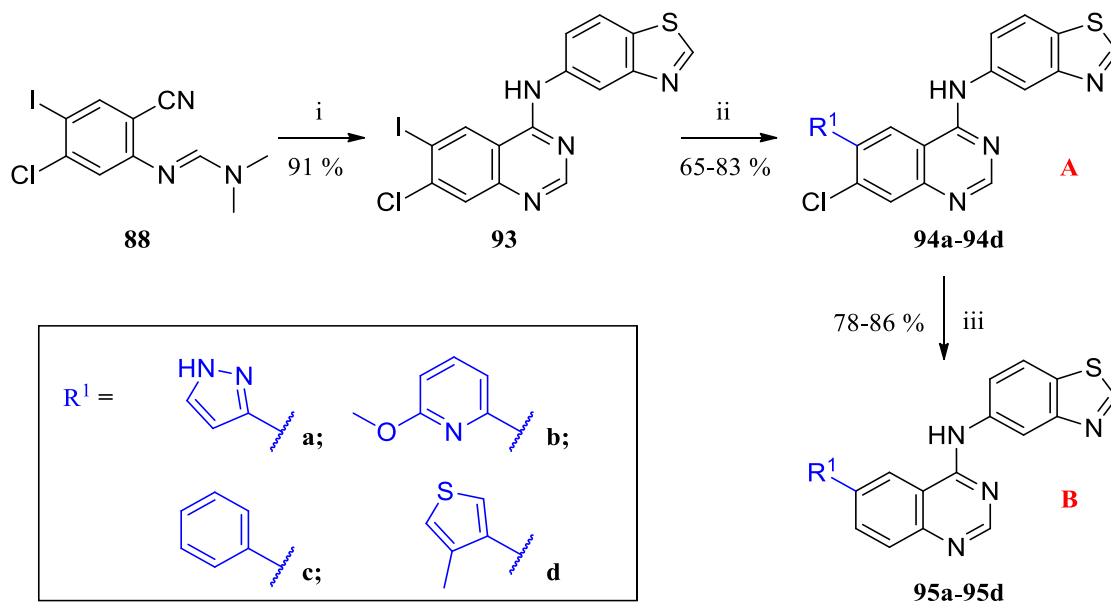
Scheme 12. Alternative synthesis of the series of compounds with the general structures **A** and **B**. Reagents and conditions: (i) 5-aminobentzothiazole, AcOH, 95 °C, 1 h; (ii) R^1-B(OH)$_2$, K$_2$CO$_3$, Pd(dppf)Cl$_2$ · DCM, dioxane:H$_2$O, 95 °C, 20 h; (iii) HCOONH$_4$, Pd$_2$(dba)$_3$, SPhos, dioxane:H$_2$O, 95 °C, 24 h.

In the second step, aryl halide **36** was reacted in neat DMF-DMA under heating, providing *N,N*-dimethylformimidamide (amidine) **88** in a quantitative yield. DMF-DMA was later removed by rotary evaporation and further purification was not necessary to proceed with the next synthetic step. A regioselective palladium-catalyzed Stille coupling was then employed to install various tributylstannyl substrates at position 4 of amidine **88**, which gave 4-heteroaryl-substituted amidine analogues **89a–89m** in 70–96 % yields. Bis(triphenylphosphine)palladium(II) dichloride served as a catalyst for the required oxidative addition, while excess lithium chloride (LiCl) was used as an additive serving to facilitate the transmetalation process.[160] Of note, the Stille coupling reaction was also attempted at a later synthetic stage; however, surprisingly, providing unsatisfactory conversion into the products.

3.7.1. Synthesis of final compounds 90a–90m

Amidine intermediates **89a–89m** were combined with 5-aminobenzothiazole in refluxing acetic acid, affording 4-*N*-heteroaryl aminoquinazoline analogues **90a–90m** in 75–92 % yields (**Scheme 13**). The products were generally precipitating from the mixture, collected and further purified by column chromatography and/or recrystallization.
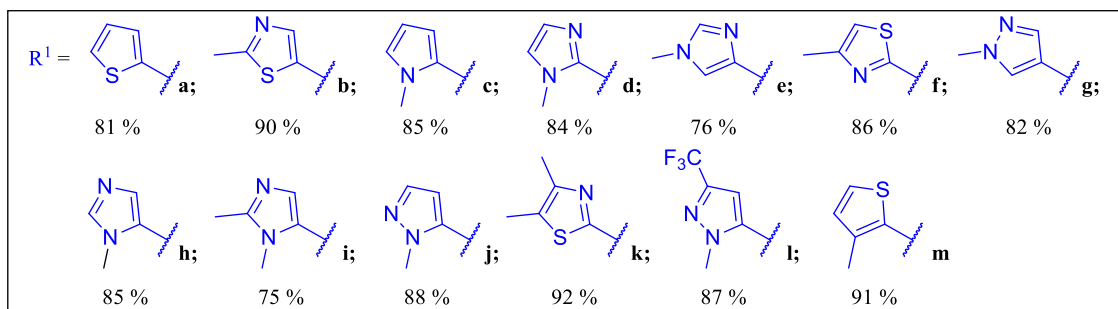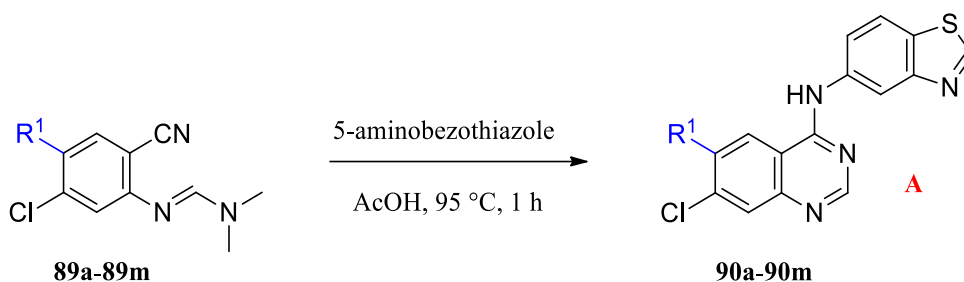
Scheme 13. Cyclization leading to quinazoline compounds **90a–90m**.

3.7.2. Synthesis of final compounds 91a–91i, 91k and 91m

Quinazoline compounds **90a–90i**, **90k** and **90m** were further reacted in a palladium-catalyzed reductive hydrochlorination, obtaining analogues **91a–91i**, **91k**, and **91m** in 70–90 % yields (**Scheme 14**). Of note, in the first attempts at this reaction, I combined ammonium formate with 10 % palladium adsorbed on a carbon powder, which turned out to be a rather inefficient catalyst. In alternative, inspired by methodologies described in the literature[161], ammonium formate was combined with a homogeneous catalytic system of $Pd_2(dba)_3$ and the Buchwald ligand SPhos, which provided excellent conversion into the products.
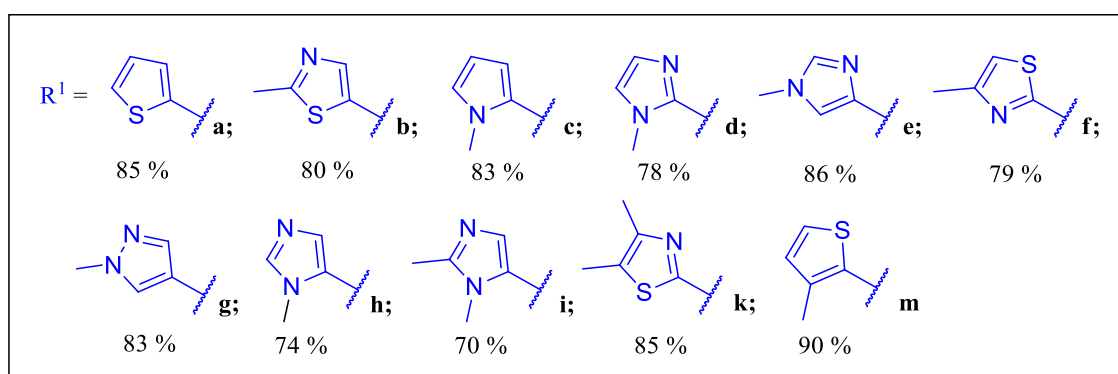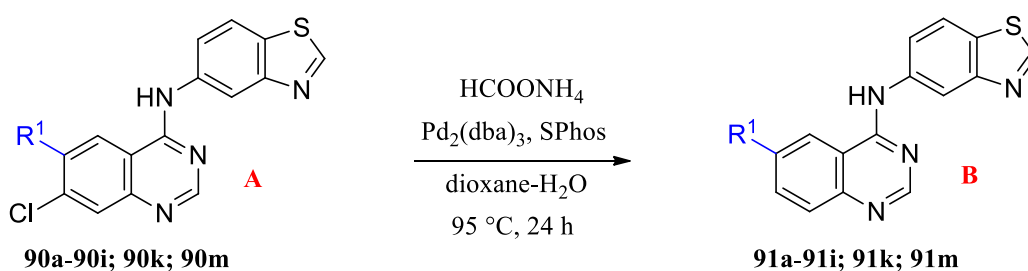
Scheme 14. Palladium-catalyzed reductive hydrodechlorination leading to quinazoline compounds **91a-91i, 91k** and **91m**.

3.7.3. Synthesis of final compounds 92an, 92ao, 92ap, 92cn and 92mn

Homogeneous $Pd_2(dba)_3$/SPhos catalytic conditions were also employed in Suzuki coupling reactions of **90a**, **90c** and **90m** with commercially available boronic acids and boronate esters, providing quinazoline analogues **92an**, **92ao**, **92ap**, **92cn** and **92mn** (**Scheme 16**). These were obtained in 45–76 % after purifications.
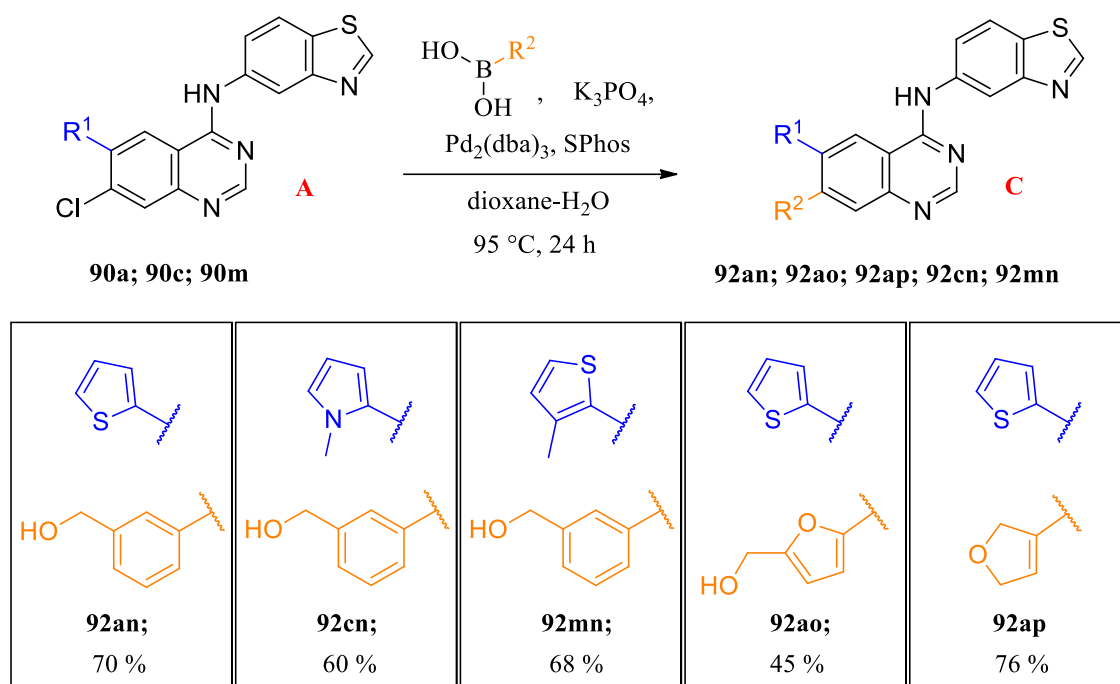
Scheme 16. Suzuki coupling leading to quinazoline compounds **92an**, **92ao**, **92ap**, **92cn** and **92mn**.

3.7.4. Synthesis of final compounds 94a–94d

As previously illustrated in **Scheme 12**, the Suzuki coupling reaction served also as an alternative method to regioselectively introduce heteroaryl and aryl moieties at position 6 of the quinazoline scaffold. In this approach, *N,N*-dimethylformimidamide derivative **88** was employed as a starting precursor and reacted with 5-aminobenzothiazole in acetic acid under reflux, which provided quinazoline intermediate **93** in 91 % yield. In contrast with the Stille coupling with tributylstannyl substrates, generally not satisfactory, the Suzuki coupling of quinazoline intermediate **93** with various boronic acids and boronate ester substrates worked well, providing 6-aryl and 6-heteroayl substituted quinazoline analogues **94a–94d** in 65–83 % yields (**Scheme 17**). Bis(diphenylphosphino)ferrocene]dichloropalladium(II) complex with DCM (Pd(dppf)Cl$_2$ · DCM) was employed as a catalyst in this methodology.
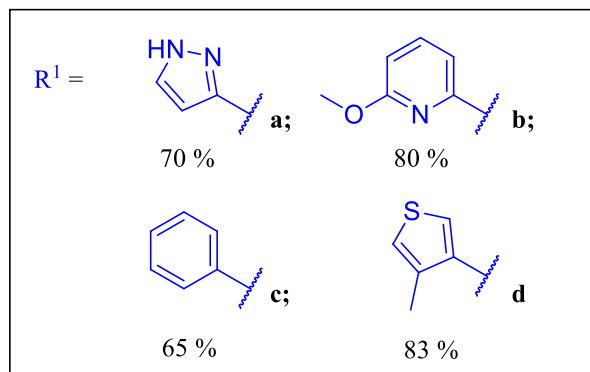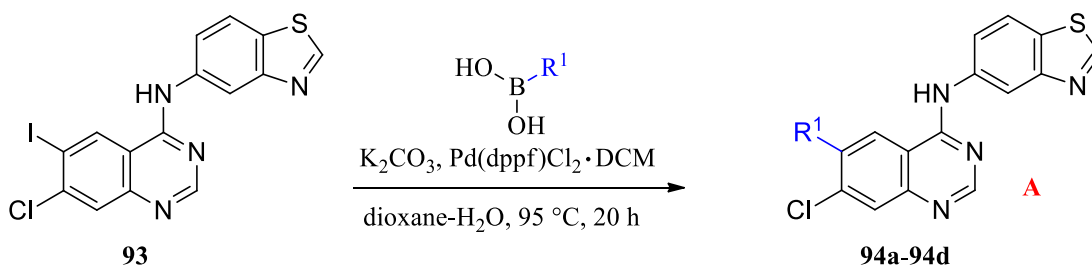
Scheme 17. Suzuki coupling leading to quinazoline compounds **94a–94d**.

3.7.5. Synthesis of final compounds 95a–95d

Lastly, employing the same reaction conditions that were previously established to obtain **91a–91i, 91k,** and **91m** (**Section 3.7.2.**), a palladium-catalyzed reductive hydrodechlorination of quinazoline analogues **94a–94d** afforded compounds **95a–95d** in 78–86 % yields (**Scheme 18**).
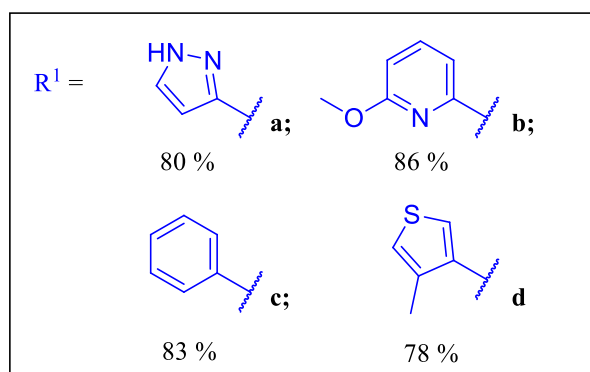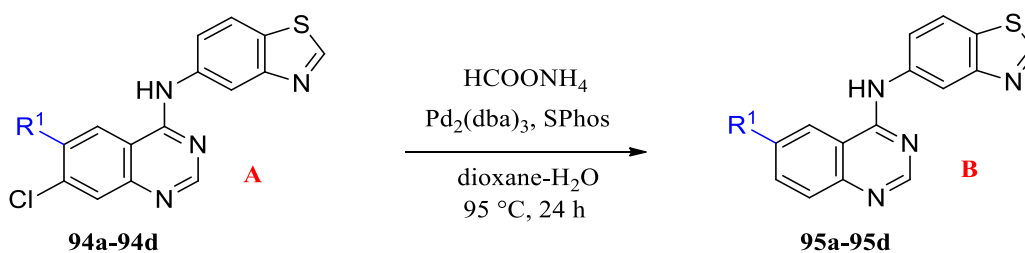
Scheme 18. Palladium-catalyzed reductive hydrodechlorination leading to quinazoline compounds **95a–95d**.
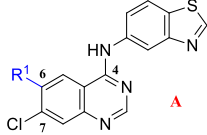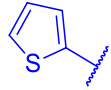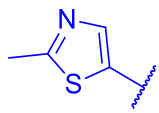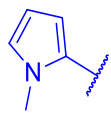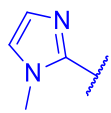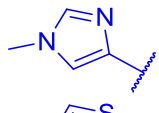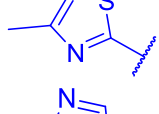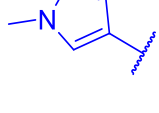
3.8. Biological results on activity and selectivity

3.8.1. Biochemical assays against RIPK1-4

The efficiency of the new molecules was initially evaluated by *in vitro* ADP-Glo assays over the human RIPK1-4 kinases, which were in-house produced and isolated (see **Chapter 5**, **Sections 5.3.** and **5.4.** for the experimental procedures).

Collectively, the compounds exhibited remarkable inhibitory efficiency against RIPK2, showing, for various cases, an extended dual-target selectivity towards both RIPK2 and RIPK3. The IC_{50} values of the three compound series (general structures A, B and C) against these RIPK isoenzymes are illustrated in **Table 2**, **Table 3** and **Table 4**, respectively. Compounds GSK2983559 **64** and GSK872 **66** were employed as positive controls.[139,145] Of note, for all the molecules, the inhibitory values exhibited against RIPK1 and RIPK4 were higher than 50 μM (data not shown). This selectivity was in agreement with documented diversities in the kinase domain structures of RIPK1 and RIPK4 that seem to hinder an appropriate binding of ATP-competitive inhibitors to these two proteins, with respect to RIPK2 and RIPK3.[108,162]

Table 2. Activity of the compound series A against RIPK2 and RIPK3 *in vitro*.

Compound	R^1	RIPK2 IC_{50} (nM)[a]	RIPK3 IC_{50} (nM)[a]
90a		14 ± 2	NA
90b		5 ± 1	NA
90c		8 ± 3	NA
90d		3 ± 0.4	NA
90e		10 ± 2	NA
90f		NA	NA
90g		4 ± 0.4	NA
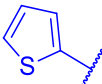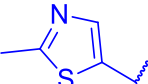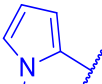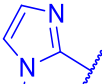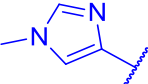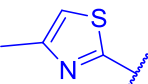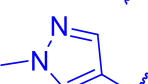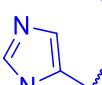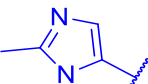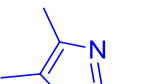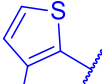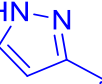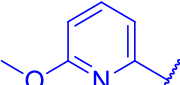
Compound	Structure		
90h		7 ± 1	NA
90i		10 ± 3	NA
90j		18 ± 1	1600
90k		NA	NA
90l		324 ± 15	2600
90m		52 ± 8	NA
94a		10 ± 0.1	NA
94b		3900	NA
94c		NA	NA
94d		104 ± 21	NA
GSK2983559 64	–	4 ± 0.9	NA
GSK872 66	–	2 ± 0.1	77 ± 4
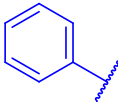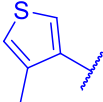
[a]Values are the mean of three experiments ± standard deviations; NA: not active up to 10 μM.

The SAR results showed that the 7-chlorinated compounds (general structure A) with heteroaryl or aryl substitutions at R^1 of the quinazoline heterocycle were mostly inactive against RIPK3 (IC_{50} > 10 μM), even though compounds 90j and 90l displayed IC_{50} values of 1.6 and 2.6 μM, respectively. In net contrast, this series of compounds exhibited outstanding potency and selectivity against RIPK2. Compounds 90a–90e, 90g–90j, 90l, 90m, 94a and 94d, bearing thiophene, pyrrole, imidazole, pyrazole, and thiazole moieties at R^1, showed generally outstanding RIPK2 inhibitory values (IC_{50} = 3–324 nM). For example, compound 90d (IC_{50} = 3 nM), bearing at R^1 a decorated imidazole-2-yl, or compound 90g (IC_{50} = 4 nM), bearing a decorated pyrazol-2-yl substituent, were equivalently potent to GSK2983559 64 (IC_{50} = 4 nM). Interestingly, only the analogues substituted at R^1 with a 4-methylthiazol-2-yl

(**90f**), or a 4,5-dimethylthiazol-2-yl (**90k**), or a 6-methoxypyridin-2-yl (**94b**), or a phenyl (**94c**), were inactive against RIPK2 (IC$_{50}$ = 4 or IC$_{50}$ > 10 µM).

Table 3. Activity of the compound series B against RIPK2 and RIPK3 *in vitro*.

Compound	R^1	RIPK2 IC$_{50}$ (nM)[a]	RIPK3 IC$_{50}$ (nM)[a]
91a		4 ± 0.4	398 ± 67
91b		4 ± 1	6000
91c		22 ± 3	2900
91d		12 ± 2	NA
91e		11 ± 1	NA
91f		5 ± 1	382 ± 87
91g		4 ± 0.4	1500
91h		4 ± 1	NA
91i		9 ± 0.2	NA
91k		14 ± 2	NA
91m		6 ± 1	388 ± 10
95a		6 ± 1	2100
95b		49 ± 3.4	NA

65

Compound	Structure	RIPK2 IC$_{50}$ (nM)[a]	RIPK3 IC$_{50}$ (nM)[a]
95c		18 ± 1	3600
95d		29 ± 4	1900
GSK2983559 **64**	–	4 ± 0.9	NA
GSK872 **66**	–	2 ± 0.1	77 ± 4

[a]Values are the mean of three experiments ± standard deviations; NA: not active up to 10 μM.
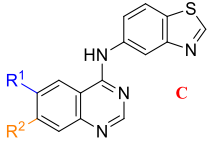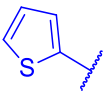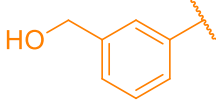
As for the series with the general structure B, these compounds exhibited great IC$_{50}$ values against RIPK2 (IC$_{50}$ = 4–49 nM). For various molecules, the potency against this enzyme increased considerably, when compared with reciprocal analogues bearing a chlorine in the scaffold. Compounds bearing 5-membered rings (**91a-91m**, **91a** and **91d**) at R^1 retained high potency against RIPK2 (IC$_{50}$ = 4–28.8 nM). In addition, with the reductive hydrodechlorination of compounds **90f**, **90k**, **94b** and **94c**, the respective resulting analogues **91f**, **91k**, **95b** and **95c** were remarkably efficient RIPK2 inhibitors (IC$_{50}$ = 5, 14, 49 and 18 nM, respectively).
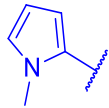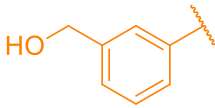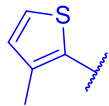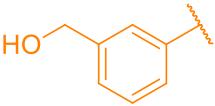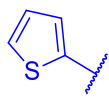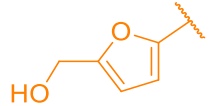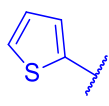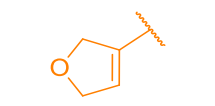
As for the selectivity, various compounds lacking the chlorine (**91d**, **91e**, **91h**, **91i**, **91k** and **95b**) were specific for the enzyme RIPK2, while other molecules of this series (**91b**, **91c**, **91g**, **95a**, **95c**, and **95d**) exhibited additional inhibitory effects on the enzyme RIPK3 (IC$_{50}$ = 1.5–6 μM). Interestingly, the dechlorinated thiophen-2-yl (**91a**), 3-methylthiophen-2-yl (**91m**), or 4-methylthiazol-2-yl (**91f**) compounds even showed an IC$_{50}$ range of 382–397 nM against RIPK3, which was only five-fold lower than GSK872 **66** (IC$_{50}$ 77 nM).

These results appeared to suggest that the absence of a chlorine atom at position 7 of the quinazoline core can correlate with changes in the efficiency of the molecules against the examined RIPKs.

The chlorine at position 7 of quinazoline compounds **90a**, **90c** and **90m** was later replaced with moieties bearing dissimilar steric bulks and lipophilic properties, such as a 3-hydroxymethylphenyl, a 5-hydroxymethylfuranyl, or a 2,5-dihydrofuranyl substituent (R^2).

Table 4. Activity of the compound series C against RIPK2 and RIPK3 *in vitro*.

Compound	R^1	R^2	RIPK2 IC$_{50}$ (nM)[a]	RIPK3 IC$_{50}$ (nM)[a]
92an			5 ± 1	551 ± 15

Compound	R^1	R^2	RIPK2 IC$_{50}$	RIPK3 IC$_{50}$
92cn	1-methyl-1H-pyrrol-2-yl	3-hydroxymethylphenyl	5 ± 0.1	141 ± 38
92mn	3-methylthiophen-2-yl	3-hydroxymethylphenyl	4 ± 1	122 ± 5
92ao	thiophen-2-yl	5-hydroxymethylfuranyl	3 ± 0.1	117 ± 19
92ap	thiophen-2-yl	2,5-dihydrofuranyl	5 ± 0.3	464 ± 64
GSK2983559 **64**	–	–	4 ± 0.9	NA
GSK872 **66**	–	–	2 ± 0.1	77 ± 4

[a]Values are the mean of three experiments ± standard deviations; NA: not active up to 10 μM.

The compounds bearing the general structure C appeared to be dual-target inhibitors against both RIPK2 and RIPK3, with low IC$_{50}$ values especially against RIPK2 (IC$_{50}$ = 3–5 nM). The potency of the molecules against RIPK3 seemed to depend on the substituents at R^1 and R^2. For instance, a combination of a 3-hydroxymethylphenyl at R^2 with a simple thiophen-2-yl at R^1 (**92an**) provided IC$_{50}$ of 551 nM against RIPK3. In comparison, combining a 3-hydroxymethylphenyl at R^2, with a 3-methylthiophen-2-yl (**92mn**), or a 1-methyl-1H-pyrrol-2-yl (**92cn**) at R^1, enabled to reach lower IC$_{50}$ values against this enzyme (IC$_{50}$ = 141 and 122 nM, respectively). Compounds **92mn** and **92cn** were almost as potent as the inhibitor GSK872 **66**. In addition, a combination of a thiophen-2-yl at R^1 with a small 5-hydroxymethylfuranyl at R^2 (**92ao**) provided outstanding dual RIPK2/3 activity (IC$_{50}$ = 3 and 117 nM, respectively). With respect to **92ao**, combining the same thiophen-2-yl at R^1 with a 2,5-dihydrofuranyl at R^2 (**92ap**), enabled to achieve comparable potency against RIPK2 (IC$_{50}$ = 5 nM), although the inhibition of RIPK3 turned out to be about four-fold lower (IC$_{50}$ = 464 nM).

3.8.2. Comparative SAR analysis of enzymatic activity and docking experiments

The docking analyses of some lead compounds (i.e., **90d**, **91h** and **92ao**, **Figure 38**), which were selected from the three series developed, can provide theoretical explanations for some general trends displayed by the new molecules in their RIPK efficacy.
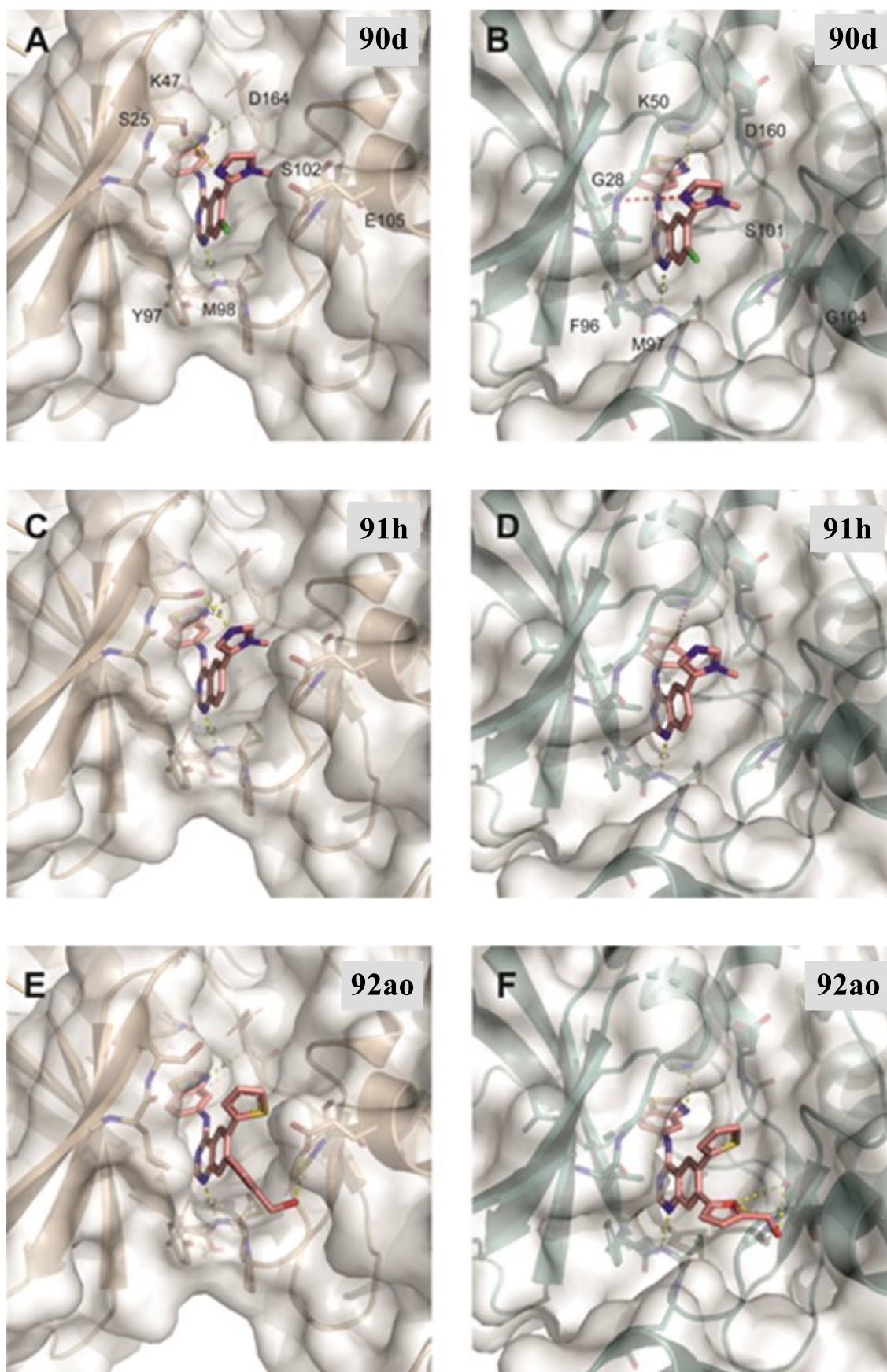
Figure 38. Docking models of selected compounds in complex with RIPK2 (PDB: 6RNA)[139] and RIPK3 (PDB: 7MX3)[154]. Structures of the selected compounds are shown in **Table 2**, **Table 3** and **Table 4**, respectively. Panels A, C, and E depict RIPK2 while panels B, D, and F depict

RIPK3. Hydrogen bond contacts are illustrated by dashed yellow lines. Distances that do not correspond to hydrogen bond contacts are shown as dashed red lines.

Even though conclusive explanations on the pronounced selectivity of the derivatives of the series A towards RIPK2 cannot be reliably drawn by the docking analyses, the three compound series exhibited target/ligand affinities which are greater for this RIPK enzyme than for RIPK3. This can suggest that the prepared compounds should engage in stronger hydrogen bond interactions with RIPK2, which is consistent with the observed enzymatic activity data. Beyond showing the target/ligand interactions of the quinazoline scaffold and the aminobenzothiazole moiety, the docking showed that heteroaryl substituents at R^1 of the quinazoline might enable the formation of hydrogen bond contacts between the molecules and the amino acid Ser25 of RIPK2 (i.e., **Figure 38A** and **C**). These interactions are described as crucial for activity against this RIPK target.[138,139] Instead, weaker molecular contacts are likely engaged in the corresponding site with RIPK3, since this enzyme contains the residue Gly28 (i.e., **Figure 38B** and **D**). In addition, as shown for **92ao**, the docking may suggest that the higher potency against RIPK3 displayed by quinazoline compounds of the series C, with respect to the other compound series, could be attributed to the hydrogen bond interactions between polar amino acids of this enzyme, such as Ser101, and the decorated moieties at R^2 (**Figure 38F**). In comparison, these substituents seem to enable less productive hydrogen bonds with the residues present in the corresponding region of RIPK2 (i.e., Ser102 and Glu105, **Figure 38E**).

In an interpretation of these overall SAR data, it may be hypothesized that the efficacy against RIPKs of the prepared molecules might be attributed to appropriate steric bulk, lipophilicity, and ability to form hydrogen bonds of the substituents at R^1 and R^2 of the quinazoline. Indeed, the activity of the compounds against RIPK3 appeared to be highly dependent on the substituents at these specified positions. On the other hand, the potent activity against RIPK2 was retained in all the three series that were explored.

3.8.3. NOD/RIPK2/NF-κB cell signaling assays

All the molecules were subsequently evaluated for efficacy against RIPK2 in living cells employing NF-κB reporter monocytes (THP-1-Lucia™). These experiments served to explore the ability of the compounds to disrupt the receptors NOD1/2 pro-inflammatory cell signaling pathways that, through the activity of RIPK2, can contribute to the mediation of downstream NF-κB activation.[151] Research studies have demonstrated that the NOD1 and NOD2 signaling can be selectively upregulated by stimulants as myristic-alanine-D-iso-

glutamine-ε-meso-lanthionine-glycine (C14-Tri-LAN-Gly)[163], or muramyl dipeptide (MDP)[164], respectively.

The compounds were therefore subjected to incubation with the monocytes and either C14-Tri-LAN-Gly, or MDP, over 24 hours (see **Chapter 5**, **Section 5.5.** for the experimental procedures). For each NOD signaling pathway, the activity of the examined substrates was determined as their corresponding IC_{50} values, which are reported in **Table 5**. In these experiments, compounds GSK2983559 **64** and GSK872 **66** were employed as positive controls.[139,145]

Table 5. Cellular activity against NOD/RIPK2/NF-κB signaling. The structures are listed in **Tables 2**, **3** and **4**.

Cpd	NOD1 THP-1 cells IC_{50} (nM)[a]	NOD2 THP-1 cells IC_{50} (nM)[a]	Cpd	NOD1 THP-1 cells IC_{50} (nM)[a]	NOD2 THP-1 cells IC_{50} (nM)[a]
90a	NA	NA	**91g**	47 ± 4	38 ± 9
90b	156 ± 44	103 ± 0.4	**91h**	119 ± 19	115 ± 12
90c	NA	NA	**91i**	143 ± 3	240 ± 32
90d	183 ± 13	58 ± 4	**91k**	NA	NA
90e	208 ± 2	140 ± 24	**91m**	438 ± 73	362 ± 150
90f	NA	NA	**92an**	432 ± 74	396 ± 189
90g	67 ± 11	63 ± 22	**92cn**	119 ± 33	95 ± 8
90h	146 ± 6	54 ± 10	**92mn**	225 ± 15	229 ± 125
90i	189 ± 34	96 ± 52	**92ao**	14 ± 4	27 ± 10
90j	313 ± 87	318 ± 150	**92ap**	51 ± 17	36 ± 4
90k	NA	NA	**94a**	155 ± 25	NA
90l	4565	3357	**94b**	NA	NA
90m	NA	NA	**94c**	NA	NA
91a	106 ± 27	120 ± 46	**94d**	NA	2084
91b	136 ± 6	108 ± 46	**95a**	114 ± 19	68 ± 13
91c	726 ± 157	523 ± 147	**95b**	NA	NA
91d	239 ± 87	273 ± 40	**95c**	4358	2129
91e	209 ± 34	95 ± 44	**95d**	4426	1533

91f	2754	NA	GSK2983559 **64**	92 ± 22	38 ± 5
			GSK872 **66**	9 ± 1	4 ± 0.05

[a]Values are reported as the mean of three experiments ± standard deviations; NA: not active up to 10 μM.

In this cellular evaluation, some compounds exerted RIPK2 activity that was not consistent with the high potency showed in the previous ADP-Glo assays. For example, among the prepared derivatives bearing a chlorine at position 7 of the quinazoline, the analogues **90a**, **90c**, **90l**, **90m** and **94d** displayed a dramatic decrement in efficacy, or a loss of activity, in the cellular setting (NOD1 IC_{50} = 4.5–10 μM and NOD2 IC_{50} = 2.1–10 μM). On the other hand, compounds **90b**, **90d**, **90e** and **90g–90j** exhibited striking inhibition against the RIPK2-mediated NOD1 and NOD2 signaling pathways (NOD1 IC_{50} = 67–313 nM and NOD2 = 54–118 nM), displaying IC_{50} values equivalent to, or even stronger than, compound GSK2983559 **64** (NOD1 IC_{50} = 92 nM and NOD2 IC_{50} = 40 μM). Remarkably, the derivative **94a** exerted potent inhibition of the NOD1 pathway (IC_{50} = 155 nM) but displayed no activity against the NOD2 pathway (IC_{50} > 10 μM).

Considering the analogues that do not bear a chlorine at position 7 of the quinazoline, **91a–91e**, **91g–91i**, **91m** and **95a** displayed excellent potency against both the NOD1/2 pathways (IC_{50} = 47–726 nM and IC_{50} = 38–523 nM, respectively). In contrast, **91f**, **91k**, **95b**, **95c** and **95d** were either weak inhibitors, or they showed no activity (NOD1 IC_{50} = 4.5–10 μM and NOD2 IC_{50} = 2.1–10 μM).

As for compounds with aryl, heteroaryl and partially saturated heterocyclic moieties at both R^1 and R^2 (**92an**, **92cn**, **92mn**, **92ao** and **92ap**), these were potent inhibitors of the NOD1/2 pathways (NOD1 IC_{50} = 14–432 nM and NOD2 IC_{50} = 27–396 nM), with the analogues **92ao** and **92ap** showing efficacy significantly greater than GSK2983559 **64**. It should be mentioned that, surprisingly, compound GSK872 **66** exhibited the highest RIPK2 inhibition in both the enzymatic and cellular activity assays that were conducted, even if it is documented in the literature as a RIPK3 selective inhibitor.[145,146]

The monocyte-based evaluation also served to determine whether the analyzed compounds were inhibiting the NF-κB recruitment induced by lipopolysaccharide (LPS), which can promote the NF-κB inflammatory signaling in fashions that are not mediated by RIPK2.[140,151] Importantly, none of the compounds did inhibit the NF-κB signaling stimulated by LPS above 33 %, even at a concentration of 10 μM (data not shown), indicating their efficiency against inflammation might depend on the selective inhibitory activity against RIPK2.

These overall results could suggest majority of the new inhibitors as promising anti-inflammatory agents, showing their favorable propensity to permeate through cellular membranes and inactivate RIPK2.

3.8.4. RIPK3-mediated necroptosis cell signaling assays

Compounds **91f**, **91m**, **92ao**, **92cn** and **92mn**, which showed potent inhibition of RIPK3 in the enzymatic evaluation, were also explored for potential cellular efficacy as anti-necroptotic agents. Following methodologies that were previously documented[146], the compounds were subjected to incubation with the human colon cancer HT-29 cells, the IAP inhibitor BV-6, the pan-caspase inhibitor z-VAD-FMK and TNF-α, to induce a necroptotic type of cell death (see **Chapter 5**, **Section 5.6.** for the experimental procedures). Inhibitor GSK872 **66** was employed as a positive control.[145,146] The data of anti-nectroptotic activity of the compounds are reported in the graph in **Figure 39**. In parallel, these analyses included the evaluation of cell viability after an exposure to incremental concentrations of the molecules (see **Chapter 5**, **Section 5.7.** for the experimental procedures), considering the reference compound was previously reported to exert cytotoxic effects correlating with its functional RIPK3 inhibition, at concentrations around 10 μM.[146] The data on cell viability were expressed as percentage values, which are reported in **Table 6**.

In contrast with the previous ADP-Glo experiments, these assessments shed light on a rather limited potency of the prepared molecules in suppressing necroptosis, in comparison with GSK872 **66** (**Figure 39**). As for the HT29 cell viability, the analyzed compounds did not exhibit negative effects until reaching concentrations up to 5 μM. However, certain derivatives (i.e., **92cn** and **92mn**) seemed to elicit some mild cytotoxicity at concentrations reaching 10 μM (**Table 6**).
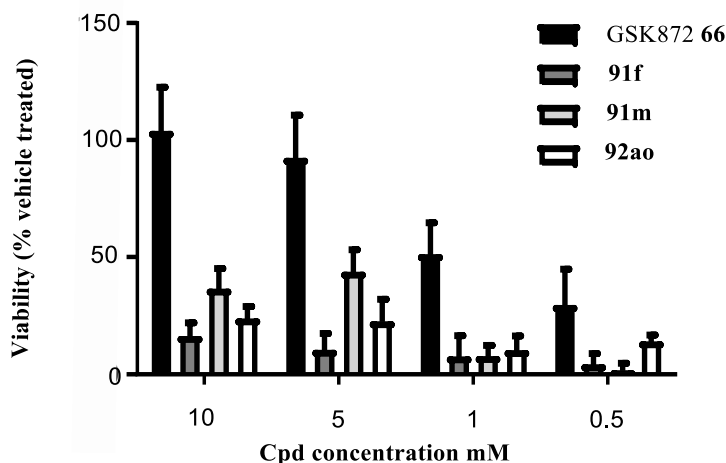
Figure 39. Activity against RIPK3-mediated necroptosis in HT-29 cells of selected compounds.

Table 6. Cytotoxicity of selected compounds in HT-29 cells.

Compound	Cell viability (% of untreated ctrl)		
	10 (μM)[a]	5 (μM)[a]	1 (μM)[a]
GSK872 **66**	103 ± 5	103 ± 5	102 ± 5
91f	104 ± 4	101 ± 5	103 ± 2
91m	95 ± 4	98 ± 5	100 ± 5
92ao	88 ± 3	95 ± 5	103 ± 8
92cn	79 ± 4	92 ± 6	104 ± 5
92mn	77 ± 4	86 ± 5	105 ± 3

[a]Values of cell viability are reported as the mean of three experiments ± standard deviations

3.8.5. Metabolic stability assays

Compounds **90d**, **90h**, **91h**, **92ao**, **92ap**, **92cn** and **92mn** were further investigated for their metabolic stability in liver microsomes and plasma, both mouse and human. Depending on the environment, separate analyses were conducted (see **Chapter 5**, **Section 5.8.** for the experimental procedures).

Initially, employing verapamil as a positive control, stability was determined as the remaining percentage values (amounts) of the molecules according to their corresponding time-dependent metabolism by human and mouse liver microsomal enzymes (i.e., CYP450 isoforms, or hydrolases) after 45 minutes of exposure. Secondly, using propantheline as a reference compound, stability was determined as the percentage values of the molecules according to their corresponding time-dependent decrement after 2 h of exposure to human and mouse plasma enzymes (i.e., esterases). The overall results are reported in **Table 7**.

All the examined compounds showed favorable trends of stability to metabolism either in plasma, or in microsomes, both in mouse and human.

Table 7. Metabolic stability of selected compounds in human and mouse microsomes and plasma.

Compound	Microsomal stability % remaining after 45 min		Plasmatic stability % remaining after 2 h	
	Human[a]	Mouse[a]	Human[a]	Mouse[a]
90d	105 ± 16	115 ± 15	141 ± 12	135 ± 21
90h	94 ± 3	105 ± 24	122 ± 8	102 ± 16
91h	108 ± 23	118 ± 18	121 ± 2	79 ± 6
92ao	124 ± 6	114 ± 11	108 ± 2	107 ± 2
92ap	108 ± 7	94 ± 5	107 ± 1	111 ± 2
92cn	124 ± 4	93 ± 9	112 ± 2	119 ± 2
92mn	123 ± 9	118 ± 6	113 ± 1	108 ± 1
Verapamil	39 ± 1	9.0 ± 0.1	–	–
Propantheline	–	–	2 ± 1	11 ± 2

3.8.6. Kinase selectivity assays

The kinase specificities of compounds **90d**, **90h**, **91a**, **91h**, **92ao**, **92cn** and **92mn** were further evaluated by radiometric analyses in a screening panel of 58 enzymes of the human kinome other than RIPKs. The experiments were conducted at a uniform concentration of the substrates (1 μM), at ATP K_m of each purified kinase, to determine inhibitory effects. These are reported as percentage values of residual activity of the kinases that were examined (**Table 8**).

Table 8. Percentage values of residual activity of human kinases exposed to selected compounds.

Human kinase	90d[a]	90h[a]	91a[a]	91h[a]	92ao[a]	92cn[a]	92mn[a]
Abl	95	95	56	94	30	88	96
ALK	94	92	99	97	73	100	107
AMPKα1	106	104	87	92	108	101	106
ASK1	107	108	103	101	98	98	89
Aurora-A	103	106	90	85	97	105	113
CaMKI	96	91	104	98	94	94	98
CDK1	102	97	95	92	92	95	85
CDK2	97	91	101	101	87	87	81
CDK6	115	107	94	99	77	75	87
CDK7	94	95	92	88	87	92	98
CDK9	84	89	97	85	105	101	93
CHK1	112	105	105	99	85	83	91
CK1γ1	89	89	112	77	87	86	94
CK2α2	99	101	98	92	110	118	110
c-RAF	101	101	96	98	84	95	103
DRAK1	109	103	93	106	99	99	101
EEF-2K	127	110	91	107	71	73	86
EGFR	90	97	46	32	17	100	92
EphA5	96	98	99	103	89	105	105
EphB4	99	109	96	109	89	99	89
Fyn	87	97	29	73	6	56	70
GSK3β	104	97	103	93	62	88	75
IGF-1R	84	77	103	84	112	119	130
IKKα	95	95	116	104	103	82	81
IRAK4	98	92	98	90	95	99	100
JAK2	99	101	94	102	87	98	103
KDR	91	86	31	34	4	26	15
LOK	82	95	50	60	21	73	66
Lyn	85	101	59	63	4	65	63
MAPKAP-K2	89	82	102	88	100	85	83
MEK1	96	103	99	94	105	101	96
MLK1	97	112	82	85	81	86	93
Mnk2	79	98	46	79	51	95	92
MSK2	105	95	102	94	95	102	107
MST1	124	120	91	105	90	94	104
mTOR	90	96	99	86	103	99	97

74

NEK2	107	103	108	98	89	96	97
p70S6K	91	88	107	93	98	101	110
PAK2	121	119	95	107	86	102	87
PDGFRβ	101	101	114	90	90	88	102
Pim-1	102	99	90	94	102	92	95
PKA	99	99	100	101	97	93	93
PKBa	100	99	98	97	75	73	82
PKCalfa	95	97	96	95	88	90	96
PKCθ	89	90	126	90	98	97	97
PKG1α	116	104	104	90	104	96	87
Plk3	102	112	102	109	102	100	102
PRAK	111	101	98	103	96	99	96
ROCK-I	107	100	104	98	88	92	102
Rse	120	115	103	110	104	107	101
Rsk1	75	82	106	85	107	96	99
SAPK2A	102	104	131	104	93	93	101
SRPK1	98	90	88	90	93	95	98
TAK1	110	107	115	105	84	90	99
PI3K(p110β/p85α)	98	95	93	93	84	93	85
PI3K(p120γ)	98	95	95	91	71	79	73
PI3K(p110δ/p85α)	96	95	92	92	79	100	90
PI3K(p110α/p85α)	93	91	88	81	99	101	100

[a]Percentage values of kinases' activities at their ATP K_ms, at 1 µM concentration of the molecules. Values in green are higher than 50 %, values in yellow are between 50 and 35 %, and values in red are below 35 %.

Compounds **90d** and **90h**, which are both chlorinated at position 7 of the quinazoline heterocycle, displayed excellent selectivity, given that no enzyme in the panel was inhibited by more than 25 % by these molecules.

Compound **91a**, which is unsubstituted at position 7 of the quinazoline, was less selective, exerting 54 % inhibition of the enzymes EGFR and Mnk2, as well as 71 % inhibition of Fyn, 69 % inhibition of KDR and 50 % inhibition of LOK. As for its direct analogue **91h**, this inhibited only the enzymes EGFR and KDR (68 % or 66 % inhibition, respectively).

Considering the structurally more complex compounds **92ao**, **92cn** and **92mn**, these exhibited dissimilar specificities. The analogues **92cn** and **92mn** were found to be remarkably selective, inhibiting only the enzyme KDR to a significant extent (74 and 85 % inhibition, respectively). In contrast, **92ao** inhibited considerably six enzymes out of the panel. The enzymes Fyn, KDR and Lyn were inhibited by 94–96 %, while LOK, EGFR and Abl were inhibited by 83 %, 79 % and 70 %, respectively.

Importantly, these data can indicate that diversifying the substitutions at positions 6 and 7 of the quinazoline scaffold of the prepared compounds can strongly affect their specificity among RIPKs as well as other kinases.

3.9. Summary and conclusions

In this body of research, novel quinazoline compounds were developed and evaluated as potential inhibitors against RIPK2 and RIPK3.

Analyzing some known quinoline and quinazoline RIPK inhibitors (i.e., GSK2983559 **64**, or GSK872 **66**) in complex with these kinase targets, new molecular modeling experiments were conducted with documented crystal structures of RIPK2 and RIPK3 and a quinazoline scaffold, leading to the design of three interrelated series of compounds. An aminobezothiazole moiety was incorporated at position 4 of the quinazoline scaffold, while positions 6 and 7 were extensively modified. Several aromatic and heteroaromatic ring moieties were introduced at position 6. A chlorine, a hydrogen, as well as decorated aryl, heteroaryl and partially saturated heterocyclic moieties, were explored at position 7. The synthesis of the final molecules included an efficient convergent cyclization approach, leading to the installation of the aminobenzothiazole at position 4 of the quinazoline central core. Appropriate palladium-catalyzed methodologies led to diversifications of positions 6 and 7 of the quinazoline. Primary bioactivity assays against the human RIPK1-4 kinases highlighted a number of selective and potent RIPK2 and dual-target RIPK2/3 inhibitors. Various derivatives displayed RIPK2 inhibitory values analogous to the reference inhibitor GSK2983559 **64**. Moreover, in cellular assays evaluating activity against the NOD/RIPK2/NF-KB signaling pathways, several compounds outweighed GSK2983559 **64** in potency. Curiously, both in enzymatic and in cellular settings, all the examined compounds exhibited weaker RIPK2 inhibition than the reference inhibitor GSK872 **66**, even though this was previously reported as isoform-selective towards RIPK3.[145] Some of the identified dual-target RIPK2/3 inhibitors were subjected to a cell-based assessment against RIPK3-mediated necroptosis, where their activity was not as high as GSK872 **66**. Selected lead compounds were evaluated for stability to enzymatic degradation in mouse or human liver microsomes and plasma, exhibiting overall excellent profiles. Lastly, some of the best compounds were investigated for selectivity over 58 human kinases not belonging to the RIPK family, where desirable enzyme specificities were observed. The SAR data therefore show that apt modifications of positions 6 and 7 of the quinazoline scaffold of the developed derivatives can translate in relevant potency and selectivity shifts towards RIPK2 and RIPK3. Consequently, structural insights achieved in this work could serve to prepare new molecules, which might be useful to further research investigations on these protein kinases.

List of publications related with the topics in the thesis

(1)   <u>Misehe, M.</u>; Klima, M.; Matoušová, M.; Chalupská, D.; Dejmek, M.; Šála, M.; Mertlíková-Kaiserová, H.; Boura, E.; Nencka, R. Structure-Based Design and Modular Synthesis of Novel PI4K Class II Inhibitors Bearing a 4-Aminoquinazoline Scaffold. *Bioorg Med Chem Lett* **2022**, *76*, 129010.

(2)   <u>Misehe, M.</u>; Matoušová, M.; Dvořáková, A.; Hercík, K.; Škach, K.; Chalupská, D.; Dejmek, M.; Šála, M.; Hájek, M.; Boura, E.; Mertlíková-Kaiserová, H.; Nencka, R. Exploring Positions 6 and 7 of a Quinazoline-Based Scaffold Leads to Changes in Selectivity and Potency towards RIPK2/3 Kinases. *Eur J Med Chem* **2023**, *260*, 115717.

(3)   <u>Misehe, M.</u>; Šála, M.; Matoušová, M.; Hercík, K.; Kocek, H.; Chalupská, D.; Chaloupecká, E.; Hájek, M.; Boura, E.; Mertlíková-Kaiserová, H.; Nencka, R. Design, synthesis and evaluation of novel thieno[2,3*d*]pyrimidine derivatives as potent and specific RIPK2 inhibitors, *Bioorg Med Chem Lett* **2023** (recently submitted, currently under peer revisions)

CHAPTER 4 – Experimental part of the PI4K class II project

4.1. Chemistry – Material, procedures and NMR characterizations

Starting precursors, reagents and anhydrous solvents were purchased and employed as received from commercial suppliers. The reactions were monitored by thin layer chromatography (TLC) using Silica gel pre-coated aluminium foils (Merck 60 F254). Samples were also monitored by liquid chromatography-mass spectrometry (LC-MS) on Waters UPLC H-Class core system, (column Waters Acquity UPLC BEH C18 1.7 mm, 2.1 x 100 mm), Waters Acquity UPLC PDA detector, Mass spectrometer Waters SQD2 and MassLynx Mass Spectrometry Software with mass detector range 100–1250 Da, set into both positive/negative switching mode, cone voltage of 15 V). For all the LC-MS analyses, it was used a gradient of H_2O/acetonitrile (containing 0.1 % formic acid), running from 0 % to 100 % over 7 minutes, with a UV absorption detection at $\lambda = 254$ nm. The purity was assessed by UV to be above 95 %. For all the final compounds, high-resolution mass data (HRMS) were acquired on a LTQ Orbitrap XL (Thermo Fisher Scientific) employing electrospray ionization (ESI). Purifications by regular column chromatography were conducted on Silica gel 60 (Fluka). C18 HP RediSep Rf columns, which were combined to a Teledyne ISCO Rf + MPLC automated system, were utilized for purifications by reverse-phase flash column chromatography. Evaporation of solvents was conducted at 2 kPa, at 30–60 °C (bath temperature). All the compounds were dried at 13 Pa, at 50 °C. NMR spectra (δ, ppm; J, Hz) were measured on either a Bruker Avance II-400 or Bruker Avance II-500 instrument (401 MHz and 500 MHz for ^{1}H, 101 MHz and 126 MHz for ^{13}C) employing hexadeuterated dimethyl sulfoxide (DMSO-d_6) as the solvent of the samples. NMR measurements were referenced to the solvent signals (δ 2.50 and 39.70, respectively for ^{1}H and for ^{13}C).

2-Amino-4-chloro-5-iodobenzonitrile (36)
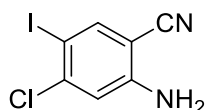
A solution of 2-amino-4-chlorobenzonitrile **35** (4 g, 26.2 mmol) in anhydrous DMF (40 ml) was treated with NIS (8.85 g, 39.3 mmol, 1.5 eq), which was added in a portionwise fashion. The mixture was stirred at room temperature for 24 h. At this point, NIS (8.85 g, 39.3 mmol, 1.5 eq) was additionally incorporated and the reaction mixture was stirred at room temperature for other 24 h. The mixture was diluted with DCM (600 ml) and washed with brine/$Na_2S_2O_3$ saturated aqueous solution (400 ml). The organic portion was dried with

anhydrous Na_2SO_4 and evaporated under reduced pressure. Purification by column chromatography (toluene/DCM, 1:1) gave compound **36** (7 g, 96 % yield) as a yellow solid. ^1H NMR (401 MHz, DMSO-d_6) δ 7.92 (s, 1H), 7.01 (s, 1H), 6.47 (s, 2H). ^{13}C NMR (101 MHz, DMSO-d_6) δ 152.66, 143.22, 143.07, 116.43, 115.66, 95.32, 79.51. LC-MS m/z: 276.7 (M-H)$^-$. Rt = 4.46 minutes.

4-Amino-6-chloroisophthalonitrile (37)
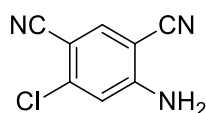
A solid mixture of compound **36** (6 g, 21.5 mmol), CuCN (3.85 g, 43 mmol, 2 eq), $Pd_2(dba)_3$ (984 mg, 1.075 mmol, 5 mol%) and XantPhos (1.244 g, 2.15 mmol, 10 mol%) was purged with argon and suspended in anhydrous 1,4-dioxane (120 ml). The resulting suspension was heated with stirring at 85 °C for 3 h. The reaction mixture was cooled to room temperature, diluted with EtOAc, filtered through Celite to remove solid impurities and evaporated to dryness. Purification of the residue by column chromatography (toluene/DCM/EtOAc, 9:2:1) provided compound **37** (3.55 g, 93 % yield) as a white solid. ^1H NMR (401 MHz, DMSO-d_6) δ 8.17 (s, 1H), 7.35 (s, 2H), 6.97 (s, 1H). ^{13}C NMR (101 MHz, DMSO-d_6) δ 155.30, 140.85, 140.22, 116.41, 116.03, 115.56, 98.11, 93.48. LC-MS m/z: 175.9 (M-H)$^-$. Rt = 3.82 minutes.

(E)-N′-(5-Chloro-2,4-dicyanophenyl)-N,N-dimethylformimidamide (38)
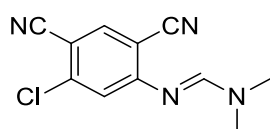
A solution of compound **37** (3.55 g, 20 mmol) in DMF-DMA (61 ml) was heated at 95 °C with stirring for 1 h. The solution was cooled to room temperature. Removal of DMF-DMA under reduced pressure provided compound **38** (4.65 g, quantitative yield) as a yellow solid. ^1H NMR (401 MHz, DMSO-d_6) δ 8.40 – 8.18 (m, 2H), 7.61 (s, 1H), 3.16 (s, 3H), 3.07 (s, 3H). ^{13}C NMR (101 MHz, DMSO-d_6) δ 159.70, 157.60, 140.46, 139.84, 119.64, 116.83, 116.17, 106.02, 103.47, 40.86, 34.87. LC-MS m/z: 233.1 (M+H)$^+$. Rt = 3.53 minutes.

4-Amino-7-chloroquinazoline-6-carbonitrile (39)
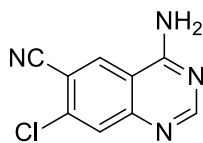
A suspension of compound **38** (4.65 g, 20 mmol) and ammonium acetate (2.78 g, 36 mmol, 1.8 eq) in AcOH (48 ml) was heated at 95 °C with stirring for 2.5 h. The mixture was cooled to room temperature, leading to a precipitation of a solid. The mixture was diluted with distilled H_2O (200 ml) and the solid was collected on a sintered funnel. Washing of the solid with distilled H_2O (15 ml) provided compound **39** (3.6 g, 88 % yield) as a yellow solid. ^{1}H NMR (401 MHz, DMSO-d_6) δ 8.94 (s, 1H), 8.50 (s, 1H), 8.29 (s, 2H), 7.92 (s, 1H). ^{13}C NMR (101 MHz, DMSO-d_6) δ 161.94, 159.70, 153.12, 137.22, 133.47, 128.40, 116.45, 113.35, 108.69. LC-MS m/z: 205.1 (M+H)[+]. Rt = 2.86 minutes.

4-Amino-7-chloroquinazoline-6-carboxamide (40)
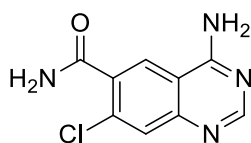
A suspension of compound **39** (600 mg, 2.9 mmol) in EtOH (26 ml) and DMSO (6.4 ml) was treated with 1N aqueous NaOH (6.4 ml) and H_2O_2 (30% aqueous solution, 6.4 ml). The mixture was stirred at room temperature for 1 h, leading to a precipitation of a solid. The mixture was diluted with EtOH (5 ml) and the solid was collected on a sintered funnel. Further recrystallization of the solid from EtOH (5 ml) gave compound **40** (600 mg, 92 % yield) as a white solid. ^{1}H NMR (401 MHz, DMSO-d_6) δ 8.41 (s, 1H), 8.39 (s, 1H), 8.13 – 7.85 (m, 3H), 7.76 – 7.71 (m, 2H). ^{13}C NMR (101 MHz, DMSO-d_6) δ 168.71, 162.13, 157.34, 150.25, 135.07, 134.43, 127.39, 124.73, 112.76. LC-MS m/z: 223.1 (M+H)[+]. Rt = 0.58 minutes.

Suzuki coupling leading to 41–50

A solid mixture of compound **40** (95 mg, 0.4 mmol), a boronic acid or a boronate ester (4 eq), K_3PO_4 (453 mg, 2.1 mmol, 5 eq), $Pd_2(dba)_3$ (16 mg, 4 mol%) and SPhos (21 mg, 12 mol%) was purged with argon and suspended in 1,4-dioxane (5.8 ml) and distilled H_2O (2.9 ml). The resulting suspension was heated with stirring at 95 °C for 24 h. The mixture was cooled to room temperature, diluted with EtOAc, filtered to remove solid impurities, and evaporated to dryness. The residue was purified as specified below.

4-Amino-7-(1*H***-indol-5-yl)quinazoline-6-carboxamide (41)**
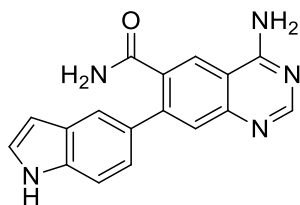
Purified by column chromatography (DCM/EtOH, 6:2), followed by recrystallization from MeOH. Off-white solid, 72 % yield. ^{1}H NMR (401 MHz, DMSO-d_6) δ 11.20 (s, 1H), 8.41 (s, 1H), 8.35 (s, 1H), 7.86 (s, 2H), 7.72 (s, 1H), 7.70 (s, 1H), 7.60 (s, 1H), 7.45 (d, J = 8.4 Hz, 1H), 7.42 (s, 1H), 7.40 (t, J = 2.8 Hz, 1H), 7.28 (dd, J = 8.4, 1.8 Hz, 1H), 6.49 (t, J = 2.7 Hz, 1H). ^{13}C NMR (101 MHz, DMSO-d_6) δ 171.98, 162.14, 156.52, 149.43, 146.15, 135.98, 135.71, 130.56, 128.10, 127.82, 126.61, 123.45, 122.31, 120.43, 112.30, 111.88, 102.21. HRMS calcd for $C_{17}H_{14}N_5O$ m/z: 304.11929 (M+H)+, found 304.11923.

4-Amino-7-(benzo[*d***][1,3]dioxol-5-yl)quinazoline-6-carboxamide (42)**
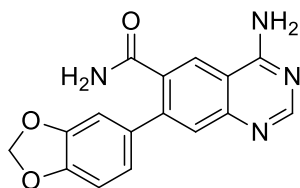
Purified by column chromatography (EtOAc/DCM/EtOH, 8:0.5:1.5), followed by recrystallization from EtOAc. White solid, 81 % yield. ^{1}H NMR (401 MHz, DMSO-d_6) δ 8.41 (s, 1H), 8.33 (s, 1H), 7.88 (s, 2H), 7.81 (s, 1H), 7.55 (s, 1H), 7.48 (s, 1H), 7.07 (t, J = 1.1 Hz, 1H), 7.00 (d, J = 1.2 Hz, 2H), 6.08 (s, 2H). ^{13}C NMR (101 MHz, DMSO-d_6) δ 171.03, 162.13, 156.92, 150.15, 147.65, 147.55, 143.43, 135.70, 133.96, 128.02, 123.47, 122.59, 112.92, 109.21, 108.73, 101.68. HRMS calcd for $C_{16}H_{13}N_4O_3$ m/z: 309.09822 (M+H)+, found 309.09813.

4-Amino-7-(6-methoxypyridin-2-yl)quinazoline-6-carboxamide (43)
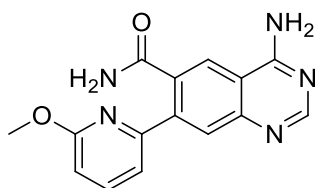
Purified by column chromatography (EtOAc/DCM/toluene/EtOH, 8:1:1:2), followed by recrystallization from EtOAc/EtOH/MeOH. White solid, 56 % yield. ^{1}H NMR (401 MHz,

DMSO-d_6) δ 8.44 (s, 1H), 8.38 (s, 1H), 7.89 (s, 1H), 7.88 (s, 2H), 7.85 (s, 1H), 7.80 (t, J = 7.7 Hz, 1H), 7.44 (s, 1H), 7.40 (d, J = 7.2 Hz, 1H), 6.82 (d, J = 8.2 Hz, 1H), 3.92 (s, 3H). ^{13}C NMR (101 MHz, DMSO-d_6) δ 172.08, 163.15, 162.13, 156.72, 154.29, 149.55, 143.20, 140.38, 135.38, 127.53, 123.87, 116.22, 113.41, 110.30, 53.73. HRMS calcd for $C_{15}H_{14}N_5O_2$ m/z: 296.11420 (M+H)$^+$, found 296.11406. Na-HRMS calcd for $C_{15}H_{13}N_5NaO_2$ m/z: 318.09615 (M+Na)$^+$, found 318.09597.

4-mino-7-(2-methoxypyridin-4-yl)quinazoline-6-carboxamide (44)
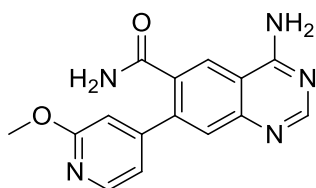
Purified by column chromatography (EtOAc/DCM/EtOH, 8:0.5:1.5), followed by recrystallization from EtOH/MeOH. White solid, 63 % yield. ^{1}H NMR (401 MHz, DMSO-d_6) δ 8.44 (s, 1H), 8.42 (s, 1H), 8.22 (dd, J = 5.3, 0.7 Hz, 1H), 7.99 (s, 2H), 7.95 (s, 1H), 7.64 (s, 1H), 7.56 (s, 1H), 7.10 (dd, J = 5.3, 1.5 Hz, 1H), 6.91 (q, J = 1.5, 0.7 Hz, 1H), 3.90 (s, 3H). ^{13}C NMR (101 MHz, DMSO-d_6) δ 170.40, 164.04, 162.18, 157.20, 150.71, 150.21, 147.16, 141.25, 135.05, 128.36, 123.87, 117.53, 113.73, 110.13, 53.69. HRMS calcd for $C_{15}H_{14}N_5O_2$ m/z: 296.11420 (M+H)$^+$, found 296.11405. Na-HRMS calcd for $C_{15}H_{13}N_5NaO_2$ m/z: 318.09615 (M+Na)$^+$, found 318.09594.

4-Amino-7-(6-methoxypyridin-3-yl)quinazoline-6-carboxamide (45)
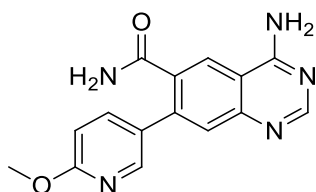
Purified by column chromatography (EtOAc/DCM/EtOH, 6:0.5:1.5), followed by recrystallization from MeOH. 88 mg. White solid, 70 % yield. ^{1}H NMR (401 MHz, DMSO-d_6) δ 8.42 (s, 1H), 8.39 (s, 1H), 8.30 (d, J = 2.0 Hz, 1H), 7.90 (s, 2H), 7.88 (s, 1H), 7.83 (dd, J = 8.5, 2.3 Hz, 1H), 7.62 (s, 1H), 7.52 (s, 1H), 6.90 (d, J = 8.5 Hz, 1H), 3.90 (s, 3H). ^{13}C NMR (101 MHz, DMSO-d_6) δ 170.79, 163.60, 162.18, 157.05, 150.26, 146.28, 140.40, 139.59, 135.40, 129.23, 128.21, 123.73, 113.16, 110.44, 53.77. HRMS calcd for $C_{15}H_{14}N_5O_2$ m/z: 296.11420 (M+H)$^+$, found 296.11407. Na-HRMS calcd for $C_{15}H_{13}N_5NaO_2$ m/z: 318.09615 (M+Na)$^+$, found 318.09590.

4-Amino-7-(3-morpholinophenyl)quinazoline-6-carboxamide (46)
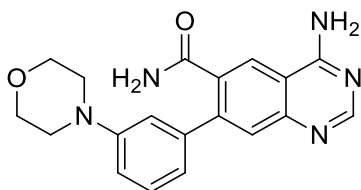
Purified by column chromatography (EtOAc/DCM/EtOH, 4:1:2), followed by recrystallization from Et$_2$O. Yellow solid, 75 % yield. ^{1}H NMR (401 MHz, DMSO-d_6) δ 8.41 (s, 1H), 8.35 (s, 1H), 7.89 (s, 2H), 7.79 (s, 1H), 7.60 (s, 1H), 7.48 (s, 1H), 7.29 (t, J = 7.9 Hz, 1H), 7.10 (t, J = 2.1 Hz, 1H), 7.04 – 6.93 (m, 2H), 3.85 – 3.69 (m, 4H), 3.21 – 3.10 (m, 4H). ^{13}C NMR (101 MHz, DMSO-d_6) δ 171.14, 162.14, 156.88, 151.35, 150.11, 144.31, 140.70, 135.89, 129.39, 128.08, 123.36, 119.72, 115.70, 115.11, 113.02, 66.59, 48.86. HRMS calcd for C$_{19}$H$_{20}$N$_5$O$_2$ m/z: 350.16115 (M+H)$^+$, found 350.16103. Na-HRMS calcd for C$_{19}$H$_{19}$N$_5$NaO$_2$ m/z: 372.14310 (M+Na)$^+$, found 372.14288.

7-(3-Acetamidophenyl)-4-aminoquinazoline-6-carboxamide (47)
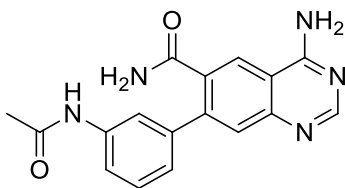
Purified by column chromatography (EtOAc/DCM/EtOH, 4.5:0.5:2), followed by recrystallization from Et$_2$O. Yellow solid, 77 % yield. ^{1}H NMR (400 MHz, DMSO-d_6) δ 10.08 (s, 1H), 8.43 (s, 1H), 8.39 (s, 1H), 7.91 (s, 2H), 7.78 (s, 1H), 7.76 (t, J = 1.9 Hz, 1H), 7.63 (dd, J = 8.0, 1.3 Hz, 2H), 7.53 (s, 1H), 7.43 (s, 1H), 7.34 (t, J = 7.9 Hz, 1H), 7.17 (dt, J = 7.7, 1.3 Hz, 1H), 2.07 (s, 3H). ^{13}C NMR (101 MHz, DMSO-d_6) δ 171.29, 170.16, 162.14, 156.73, 149.47, 144.52, 140.24, 139.16, 135.12, 129.30, 127.80, 123.98, 123.66, 119.64, 119.45, 112.90, 24.15. HRMS calcd for C$_{17}$H$_{16}$N$_5$O$_2$ m/z: 322.12985 (M+H)$^+$, found 322.12973. Na-HRMS calcd for C$_{17}$H$_{15}$N$_5$NaO$_2$ m/z: 344.11180 (M+Na)$^+$, found 344.11163.

**4-Amino-7-(1*H*-indol-6-yl)quinazoline-6-carboxamide (48)**
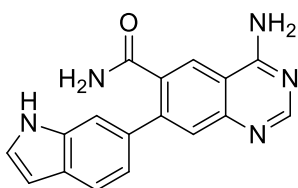
Purified by column chromatography (EtOAc/DCM/EtOH, 10:1:1), followed by recrystallization from Et$_2$O/EtOAc. Beige solid, 83 % yield. ^{1}H NMR (401 MHz, DMSO-d_6) δ 11.26 (s, 1H), 8.42 (s, 1H), 8.37 (s, 1H), 7.89 (s, 2H), 7.73 (s, 1H), 7.60 (s, 1H), 7.59 (d, J = 8.1 Hz, 1H), 7.58 (s, 1H), 7.42 (s, 1H), 7.41 (t, J = 2.7 Hz, 1H), 7.19 (dd, J = 8.3, 1.4 Hz, 1H), 6.47 (t, J = 1.9 Hz, 1H). ^{13}C NMR (101 MHz, DMSO-d_6) δ 171.83, 162.15, 156.57, 149.44, 145.93, 136.20, 135.69, 132.60, 127.87, 127.85, 126.87, 123.51, 120.47, 120.27, 112.41, 111.74, 101.64. HRMS calcd for C$_{17}$H$_{14}$N$_5$O m/z: 304.11929 (M+H)$^+$, found 304.11914.

**4-Amino-7-(3-(hydroxymethyl)phenyl)quinazoline-6-carboxamide (49)**
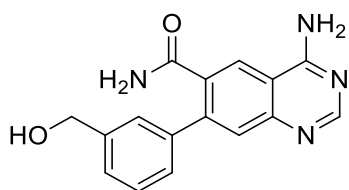
Purified by column chromatography (EtOAc/DCM/EtOH, 5:1.5:1.5), followed by recrystallization from Et$_2$O. White solid, 66 % yield. ^{1}H NMR (401 MHz, DMSO-d_6) δ 8.42 (s, 1H), 8.39 (s, 1H), 7.93 (s, 2H), 7.83 (s, 1H), 7.57 (s, 1H), 7.49 (s, 1H), 7.47 (s, 1H), 7.42 – 7.33 (m, 3H), 5.29 (t, J = 5.7 Hz, 1H), 4.57 (d, J = 5.7 Hz, 2H). ^{13}C NMR (101 MHz, DMSO-d_6) δ 171.48, 162.15, 156.69, 149.49, 144.71, 142.56, 139.48, 135.21, 128.75, 127.85, 127.25, 126.80, 126.74, 123.62, 112.82, 63.26. HRMS calcd for C$_{16}$H$_{15}$N$_4$O$_2$ m/z: 295.11895 (M+H)$^+$, found 295.11887. Na-HRMS calcd for C$_{16}$H$_{14}$N$_4$NaO$_2$ m/z: 317.10090 (M+Na)$^+$, found 317.10077.

4-Amino-7-(2,3-dihydrobenzofuran-5-yl)quinazoline-6-carboxamide (50)
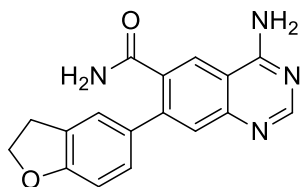
Purified by column chromatography (DCM/EtOAc/EtOH, 6:1:1), followed by recrystallization from EtOH/MeOH. Off-white solid, 73 % yield. ^{1}H NMR (401 MHz, DMSO-d_6) δ 8.40 (s, 1H), 8.33 (s, 1H), 7.86 (s, 2H), 7.77 (s, 1H), 7.53 (s, 1H), 7.47 (s, 1H), 7.40 (s, 1H), 7.26 (dd, J = 8.2, 1.9 Hz, 1H), 6.83 (d, J = 8.2 Hz, 1H), 4.58 (t, J = 8.7 Hz, 2H), 3.23 (t, J = 8.7 Hz, 2H). ^{13}C NMR (101 MHz, DMSO-d_6) δ 171.72, 162.11, 160.11, 156.60, 149.51, 144.62, 135.31, 131.91, 128.69, 128.16, 127.44, 125.59, 123.51, 112.47, 109.24,

71.75, 29.33. HRMS calcd for $C_{17}H_{15}N_4O_2$ m/z: 307.11895 $(M+H)^+$, found 307.11877. Na-HRMS calcd for $C_{17}H_{14}N_4NaO_2$ m/z: 329.10090 $(M+Na)^+$, found 329.10070.

Suzuki coupling and hydrolysis of the carbonitrile leading to 51–57

A solid mixture of compound **39** (104 mg, 0.5 mmol), a suitable boronic acid or a boronate ester (4 eq), K_3PO_4 (541 mg, 2.6 mmol, 5 eq), $Pd_2(dba)_3$ (19 mg, 4 mol%) and SPhos (25 mg, 12 mol%) was purged with argon and suspended in 1,4-dioxane (7 ml) and distilled H_2O (3.5 ml). The suspension was heated with stirring at 95 °C for 24 h. The mixture was cooled to room temperature, diluted with EtOAc, filtered to remove solid impurities and evaporated under reduced pressure. The resulting residue was suspended in EtOH (1.2 ml) and DMSO (0.3 ml) and treated with 1N aqueous NaOH (0.3 ml) and H_2O_2 (30% aqueous solution, 0.3 ml). The suspension was stirred at room temperature for 1 h. The mixture was diluted with EtOAc (150 ml) and washed with brine (70 ml). The organic portion was dried over anhydrous Na_2SO_4 and evaporated under reduced pressure. The residue was purified as specified below.

4-Amino-7-(3-carbamoylphenyl)quinazoline-6-carboxamide (51)

Purified by column chromatography (DCM/EtOH, 3:2), followed by recrystallization from MeOH. White solid, 60 % overall yield. ^{1}H NMR (401 MHz, DMSO-d_6) δ 8.44 (s, 1H), 8.41 (s, 1H), 8.08 (s, 1H), 8.05 (t, J = 1.8 Hz, 1H), 7.90 (s, 2H), 7.89 (dt, J = 7.8, 1.4 Hz, 1H), 7.84 (s, 1H), 7.67 (s, 1H), 7.64 (dt, J = 7.8, 1.4 Hz, 1H), 7.53 (d, J = 7.8 Hz, 1H), 7.50 (s, 1H), 7.42 (s, 1H). ^{13}C NMR (101 MHz, DMSO-d_6) δ 171.10, 169.07, 162.19, 156.88, 149.72, 143.83, 139.92, 135.13, 134.43, 131.79, 128.95, 128.19, 127.86, 127.39, 123.76, 113.06. HRMS calcd for $C_{16}H_{14}N_5O_2$ m/z: 308.11420 $(M+H)^+$, found 308.11405.

7-(3-(1*H*-Tetrazol-5-yl)phenyl)-4-aminoquinazoline-6-carboxamide (52)
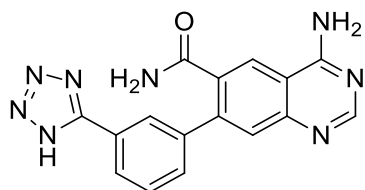
Purified by column chromatography (DCM/EtOH, 2.5:2), followed by recrystallization from MeOH/acetonitrile. White solid, 54 % overall yield. ^{1}H NMR (401 MHz, DMSO-d_6) δ 8.44 (s, 1H), 8.41 (s, 1H), 8.17 (t, J = 1.8 Hz, 1H), 8.01 (dt, J = 7.2, 1.7 Hz, 1H), 7.94 (s, 2H), 7.85 (s, 1H), 7.62 (s, 1H), 7.51 – 7.40 (m, 3H) (peak of NH of tetrazole was not detected). ^{13}C NMR (101 MHz, DMSO-d_6) δ 170.80, 162.20, 160.06, 157.00, 150.21, 144.07, 140.35, 135.62, 131.79, 128.90, 128.25, 128.04, 126.49, 125.80, 123.70, 113.12. HRMS calcd for $C_{16}H_{13}N_8O$ m/z: 333.12068 (M+H)$^+$, found 333.12050. Na-HRMS calcd for $C_{16}H_{12}N_8NaO$ m/z: 355.10263 (M+Na)$^+$, found 355.10245.

4-Amino-7-(3,6-dimethoxypyridazin-4-yl)quinazoline-6-carboxamide (53)
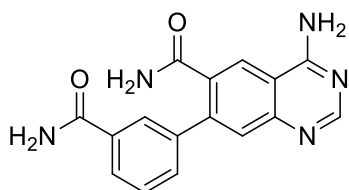

Purified by column chromatography (EtOAc/DCM/EtOH, 6:1:2), followed by recrystallization from Et$_2$O/MeOH. White solid, 63 % overall yield. ^{1}H NMR (401 MHz, DMSO-d_6) δ 8.54 (s, 1H), 8.45 (s, 1H), 7.97 (s, 2H), 7.74 (s, 1H), 7.62 (s, 1H), 7.42 (s, 1H), 7.19 (s, 1H), 3.99 (s, 3H), 3.86 (s, 3H). ^{13}C NMR (101 MHz, DMSO-d_6) δ 169.62, 162.47, 162.34, 159.42, 157.40, 150.63, 137.17, 134.72, 133.94, 129.76, 123.95, 119.60, 113.84, 54.59, 54.42. HRMS calcd for $C_{15}H_{15}N_6O_3$ m/z: 327.12001 (M+H)$^+$, found 327.11987. Na-HRMS calcd for $C_{15}H_{14}N_6NaO_3$ m/z: 349.10196 (M+Na)$^+$, found 349.10178.

4-Amino-7-(2-(furan-2-yl)phenyl)quinazoline-6-carboxamide (54)
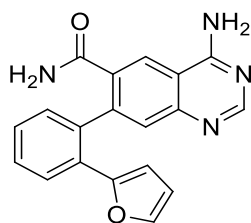
Purified by column chromatography (DCM/EtOH, 6:2), followed by recrystallization from Et$_2$O/MeOH. Off-white solid, 70 % overall yield. ^{1}H NMR (401 MHz, DMSO-d_6) δ 8.48 (s, 1H), 8.40 (s, 1H), 7.95 (s, 2H), 7.76 (dd, J = 7.9, 1.3 Hz, 1H), 7.58 (dd, J = 1.8, 0.7 Hz, 1H), 7.52 – 7.42 (m, 2H), 7.35 (td, J = 7.4, 1.3 Hz, 1H), 7.32 – 7.24 (m, 3H), 6.29 (dd, J = 3.4, 1.8 Hz, 1H), 5.64 (dd, J = 3.4, 0.8 Hz, 1H). ^{13}C NMR (101 MHz, DMSO-d_6) δ 169.96, 162.33, 156.57, 152.12, 149.17, 145.36, 142.79, 136.68, 135.18, 130.69, 129.07, 128.73, 128.00,

127.67, 126.56, 123.58, 112.99, 112.16, 109.48. HRMS calcd for $C_{19}H_{15}N_4O_2$ m/z: 331.11895 (M+H)$^+$, found 331.11877. Na-HRMS calcd for $C_{19}H_{14}N_4NaO_2$ m/z: 353.10090 (M+Na)$^+$, found 353.10072.

4-Amino-7-(1-(tetrahydro-2*H*-pyran-4-yl)-1*H*-pyrazol-4-yl)quinazoline-6-carboxamide (55)
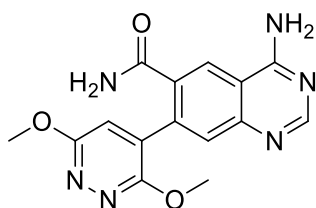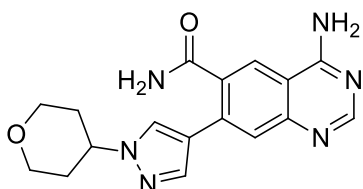

Purified by column chromatography (DCM/EtOH, 5:2), followed by recrystallization from EtOH/MeOH. White solid, 64 % overall yield. ^{1}H NMR (401 MHz, DMSO-d_6) δ 8.38 (s, 1H), 8.23 (s, 2H), 7.96 (s, 1H), 7.88 (s, 1H), 7.81 (s, 2H), 7.79 (s, 1H), 7.64 (s, 1H), 4.45 (tt, *J* = 10.1, 4.8 Hz, 1H), 4.07 – 3.92 (m, 2H), 3.49 (td, *J* = 11.4, 2.8 Hz, 2H), 2.10 – 1.87 (m, 4H). ^{13}C NMR (101 MHz, DMSO-d_6) δ 172.30, 161.95, 156.48, 149.53, 138.07, 134.94, 134.36, 127.83, 125.28, 123.12, 119.14, 112.14, 66.32, 57.78, 33.15. HRMS calcd for $C_{17}H_{19}N_6O_2$ m/z: 339.15640 (M+H)$^+$. found 339.15629. Na-HRMS calcd for $C_{17}H_{18}N_6NaO_2$ m/z: 361.13835 (M+Na)$^+$, found 361.13817.

### 4-Amino-7-(1*H*-benzo[*d*]imidazol-5-yl)quinazoline-6-carboxamide (56)
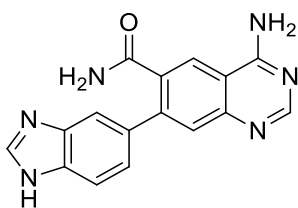
Purified by column chromatography (acetonitrile/EtOH, 3:2), followed by recrystallization from MeOH. White solid, 44 % overall yield. ^{1}H NMR (500 MHz, DMSO-d_6, T = 330 K) δ 8.35 (s, 1H), 8.31 (s, 1H), 8.16 (s, 1H), 7.75 – 7.63 (m, 3H), 7.56 (d, *J* = 8.6 Hz, 1H), 7.54 (s, 1H), 7.50 (s, 1H), 7.30 (dd, *J* = 8.3, 1.7 Hz, 1H), 7.20 (s, 1H). (peak of NH on benzimidazole was not detected). ^{13}C NMR (126 MHz, DMSO-d_6, T = 330 K) δ 171.03, 162.25, 156.87, 150.25, 144.83, 143.09, 136.04, 128.53, 123.53, 112.89. (carbons on benzimidazole were not fully detected due to rapid proton exchange). HRMS calcd for $C_{16}H_{13}N_6O$ m/z: 305.11454 (M+H)$^+$, found 305.11438.

4-Amino-7-(6-oxo-1,6-dihydropyridin-3-yl)quinazoline-6-carboxamide (57)

Purified by column chromatography (acetonitrile/DCM/EtOH, 2:1:2), followed by recrystallization from MeOH. White solid, 52 % overall yield. 1H NMR (500 MHz, DMSO-d_6) δ 8.41 (s, 1H), 8.36 (s, 1H), 8.01 – 7.80 (m, 3H), 7.63 – 7.56 (m, 3H), 7.54 (d, J = 2.7 Hz, 1H), 6.40 (d, J = 9.4 Hz, 1H). (peak of NH on pyridone was not detected). ^{13}C NMR (126 MHz, DMSO-d_6) 170.90, 166.47, 162.22, 162.13, 157.02, 150.37, 142.06, 139.54, 134.85, 127.28, 123.86, 119.69, 117.56, 112.94. HRMS calcd for $C_{14}H_{12}N_5O_2$ m/z: 282.09855 (M+H)$^+$, found 282.09838. Na-HRMS calcd for $C_{14}H_{11}N_5NaO_2$ m/z: 304.08050 (M+Na)$^+$, found 304.08033.

Suzuki coupling, reduction of the formyl group and hydrolysis of the carbonitrile leading to 58 and 59

A solid mixture of compound **39** (104 mg, 0.5 mmol), a boronic acid or a boronate ester (4 eq), K_3PO_4 (541 mg, 2.6 mmol, 5 eq), $Pd_2(dba)_3$ (19 mg, 4 mol%) and SPhos (25 mg, 12 mol%) was purged with argon and suspended in 1,4-dioxane (7 ml) and distilled H_2O (3.5 ml). The suspension was heated with stirring at 95 °C for 24 h. The mixture was cooled to room temperature, diluted with EtOAc, filtered to remove solid impurities and evaporated under reduced pressure. The residue was suspended in EtOH (3.5 ml) and treated with $NaBH_4$ (58 mg, 1.53 mmol, 3 eq) over 10 min at room temperature. The resulting slurry was allowed to stir for 45 min. The mixture was evaporated to dryness. The residue was suspended in EtOH (1.6 ml) and DMSO (0.4 ml) and treated with 1N aqueous NaOH (0.4 ml) and H_2O_2 (30% aqueous solution, 0.4 ml). The suspension was stirred at room temperature for 1 h. The mixture was diluted with EtOAc (150 ml) and washed with brine (70 ml). The organic portion was dried over anhydrous Na_2SO_4 and evaporated under reduced pressure. The residue was purified as specified below.

4-Amino-7-(5-(hydroxymethyl)furan-2-yl)quinazoline-6-carboxamide (58)
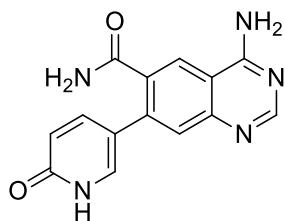

Purified by column chromatography (EtOAc/DCM/EtOH, 6:1:3), followed by recrystallization from MeOH. Off-white solid, 40 % overall yield. ^{1}H NMR (401 MHz, DMSO-d_6) δ 8.40 (s, 1H), 8.25 (s, 1H), 8.03 (s, 1H), 7.92 (s, 1H), 7.86 (s, 2H), 7.69 (s, 1H), 6.90 (d, J = 3.3 Hz, 1H), 6.45 (d, J = 3.3 Hz, 1H), 5.37 (t, J = 5.8 Hz, 1H), 4.49 (d, J = 5.6 Hz, 2H). ^{13}C NMR (101 MHz, DMSO-d_6) δ 171.31, 161.94, 157.05, 156.93, 150.08, 149.58, 133.13, 131.39, 123.44, 123.39, 112.83, 111.51, 109.83, 56.22. HRMS calcd for $C_{14}H_{13}N_4O_3$ m/z: 285.09822 (M+H)$^+$, found 285.09806. Na-HRMS calcd for $C_{14}H_{12}N_4NaO_3$ m/z: 307.08016 (M+Na)$^+$, found 307.07992.

4-Amino-7-(5-(hydroxymethyl)pyridin-3-yl)quinazoline-6-carboxamide (59)
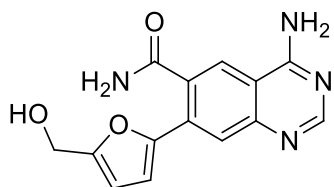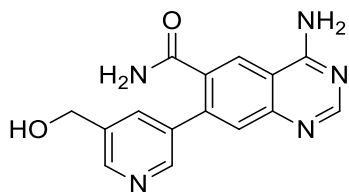

Purified by column chromatography (DCM/EtOH, 2.5:2), followed by recrystallization from MeOH. White solid, 52 % overall yield. ^{1}H NMR (401 MHz, DMSO-d_6) δ 8.56 (d, J = 2.2 Hz, 1H), 8.54 (d, J = 2.0 Hz, 1H), 8.44 (s, 2H), 7.97 (s, 2H), 7.93 (s, 1H), 7.85 (t, J = 2.2 Hz, 1H), 7.63 (s, 1H), 7.54 (s, 1H), 5.42 (t, J = 5.5 Hz, 1H), 4.61 (d, J = 5.2 Hz, 2H). 13C NMR (101 MHz, DMSO-d_6) δ 170.54, 162.21, 157.18, 150.30, 147.66, 147.51, 140.77, 137.62, 135.31, 135.25, 134.39, 128.76, 123.91, 113.43, 61.02. HRMS calcd for $C_{15}H_{14}N_5O_2$ m/z: 296.11420 (M+H)$^+$, found 296.11404. Na-HRMS calcd for $C_{15}H_{13}N_5NaO_2$ m/z: 318.09615 (M+Na)$^+$, found 318.09593.

4.2. Crystallography experiments - Material and methods

4.2.1. PI4K2B production and isolation

Employing procedures previously standardized[71], the truncated human PI4K2B enzyme (residues 90-450) was engineered with a T4 lysozyme tag, serving to replace the cysteine rich loop 165-VHKVCCPCCF-175 and promote the co-crystallization process. The fusion protein sequence to be expressed contained an additional N-terminal 6x histidine (His$_6$) purification tag, followed with a GB1 solubility and folding tags. In addition, the sequence contained a TEV protease cleavage site. Protein expression was conducted in bacteria *E. coli* BL21 DE3 NiCo, provided by New England Biolabs, employing the autoinduction ZY-5052 medium. The bacterial cells were centrifuged and lysed using the Emulsiflex C3 instrument (Avestin) in the lysis buffer (50 mM trimetamol pH 8, 300 mM NaCl, 20 mM imidazole, 10 % glycerol, 3 mM β-mercaptoethanol). Centrifugation of the lysate for 30 min at 30,000 g was followed by incubation with the HisPur Ni-NTA Agarose Superflow (Thermo Fisher Scientific) for 30 min. The chromatography matrix beads were subsequently washed with the lysis buffer previously employed. The enzyme was eluted by supplementing the buffer with 300 mM imidazole. Removal of the His$_6$-GB1 tag by cleavage with the recombinant TEV protease was performed overnight. PI4K2B was obtained after purification by size exclusion chromatography at the HiLoad 16/600 Superdex 200 prep grade column (Cytiva) in the buffer A (10 mM 2-(N-morpholino)ethanesulfonic acid pH 6.5, 100 mM NaCl, 3 mM β-mercaptoethanol), followed by cation exchange chromatography at the HiTrap S HP column (Cytiva) shifting from the buffer A to the buffer B (10 mM 2-(N-morpholino)ethanesulfonic acid pH 6.5, 500 mM NaCl, 3 mM β-mercaptoethanol). After concentration to 6 mg/ml, as a standard storage procedure[71], the enzyme preparation was divided into aliquots that were flash frozen in liquid nitrogen at 193 K.

4.2.2. Co-crystallization procedure and analysis

A soaking methodology was employed to obtain co-crystallization of **49** in complex with PI4K2B. Crystals of PI4K2B devoid of the ligand were first prepared and selected. The enzyme was supplemented with 5 mM TCEP. Employing a vapor diffusion technique at 291 K, crystals were obtained over 3-5 days stand in sitting drops containing 400 nl of the solution of the enzyme and 400 nl of the solution of the well. Crystals were set to grow in a well solution consisting of 10 % polyethylene glycol 8,000, 20 % ethylene glycol, 3 % DMSO, 100 mM bicine/Trizma base pH 8.5, and a mixture of alcohols (1,6-hexanediol, 1-butanol, 1,2-propanediol, 2-propanol, 1,4-butanediol, 1,3-propanediol), each at the concentration of 20 mM. At this point, the crystals were submitted to soaking in sitting drops

of the same composition consisting of a saturated solution of the ligand **49** over 24 h. A single crystal enabled the collection of the crystallographic dataset, which was conducted by employing in-house equipment, including the Rigaku MicroMax-007 HF rotating anode and the Dectris Pilatus 200K pixel detector. *XDS* was employed for integration and scaling of the data.[165] Molecular replacement of the ligand from the structure of the PI4K2B/ATP **1** complex (PDB: 4WTV)[71] enabled to resolve the structure of the PI4K2B/**49** complex. The collected data are summarized in **Table 9**.

Table 9. Data on the co-crystal structure of the PI4K2B/**49** complex. Parentheses define the highest resolution shell values. R.m.s.d. stands for root-mean-square deviation.

Crystal		PI4K2B/**49** complex
PDB accession code		8A5X
Data collection and processing		
Space group		P 1 2_1 1 (no. 4)
Cell dimensions	a, b, c (Å)	48.4 87.0 71.4
	α, β, γ (°)	90.0 107.8 90.0
Resolution range (Å)		30.44 - 2.40 (2.49 - 2.40)
No. of unique reflections		20,410 (1,863)
Completeness (%)		92.2 (84.4)
Multiplicity		3.6 (3.8)
Mean I/σ(I)		13.38 (2.29)
Wilson B factor (Å^2)		32.31
R-merge		0.0995 (0.6079)
R-meas		0.1164 (0.7059)
CC1/2 (%)		99.6 (76.4)
CC* (%)		99.9 (93.1)
Structure resolution and refinement		
R-work (%)		21.04 (26.82)
R-free (%)		22.93 (28.02)
CC-work (%)		94.6 (82.7)
CC-free (%)		91.7 (84.5)
R.m.s.d.	bonds (Å)	0.002
	angles (°)	0.47
Average B factor (Å^2)	overall	43.98
	protein	44.14
	ligands	57.55
	solvent	35.44
Clashscore		0.79
Ramachandran (%)	favored	98.48
	allowed	1.52
	outliers	0.00

CHAPTER 5 – Experimental part of the RIPK2/3 project

5.1. Chemistry – Material, procedures and NMR characterizations

General part on the material, procedures and instrumentation employed was previously described (see **Chapter 4, Section 4.1.**).

(*E*)-*N'*-(5-Chloro-2-cyano-4-iodophenyl)-*N*,*N*-dimethylformimidamide (88)
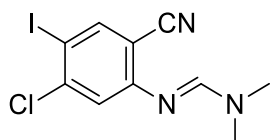
Intermediate **36** (250 mg, 0.9 mmol) was suspended in DMF-DMA (6.6 ml) and the suspension was heated at 95 °C with stirring for 1 h. The mixture was cooled to room temperature and the solvent was removed under reduced pressure, affording the derivative **88** (300 mg, quantitative yield) as a yellow solid. ^{1}H NMR (401 MHz, DMSO-d_6) δ 8.11 (s, 1H), 8.09 (s, 1H), 7.49 (s, 1H), 3.09 (s, 3H), 3.00 (s, 3H). ^{13}C NMR (101 MHz, DMSO-d_6) δ 156.34, 156.32, 143.45, 143.11, 119.56, 116.97, 107.17, 87.58, 40.43, 34.59. LC-MS m/z: 334.0 (M+H)$^+$. Rt = 4.1 minutes.

Stille coupling leading to 89a–89m

Intermediate **88** (300 mg, 0.9 mmol) was dissolved in anhydrous 1,4-dioxane (4.2 ml). The solution was treated with a tributylstannyl substrate (1.5 eq), LiCl (5eq) and PdCl$_2$(PPh$_3$)$_2$ (4 mol%). After purging with argon, the suspension was set under heating with stirring at 95 °C for 18 h. The mixture was cooled to room temperature, diluted with EtOAc and filtered to remove solid impurities. The solvent was removed under reduced pressure and the residue was purified as specified below.

(*E*)-*N'*-(5-Chloro-2-cyano-4-(thiophen-2-yl)phenyl)-*N*,*N*-dimethylformimidamide (89a)
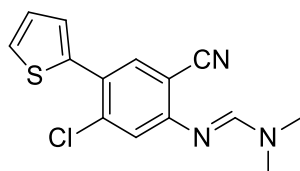
Purified by column chromatography (DCM/EtOAc, 10:1), followed by reverse phase column chromatography (H$_2$O/MeOH, 30 % to 100 %). White solid, 94 % yield. ^{1}H NMR (401 MHz, DMSO-d_6) δ 8.15 (s, 1H), 7.85 (s, 1H), 7.67 (dd, *J* = 5.1, 1.2 Hz, 1H), 7.47 (s, 1H), 7.41 (dd,

J = 3.6, 1.2 Hz, 1H), 7.16 (dd, J = 5.1, 3.6 Hz, 1H), 3.12 (s, 3H), 3.03 (s, 3H). ^{13}C NMR (101 MHz, DMSO-d_6) δ 156.33, 155.29, 138.26, 136.73, 135.33, 128.40, 127.84, 127.68, 125.95, 120.40, 117.92, 106.04, 40.45, 34.61. LC-MS m/z: 290.0 (M+H)[+]. Rt = 4.3 minutes.

(*E*)-*N'*-(5-Chloro-2-cyano-4-(2-methylthiazol-5-yl)phenyl)-*N,N*-dimethylformimidamide (89b)
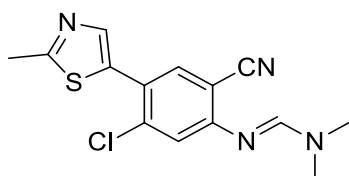
Purified by column chromatography (toluene/DCM/EtOAc, 4:1:1), followed by reverse phase column chromatography (H$_2$O/MeOH, 30 % to 100 %). Yellow solid, 90 % yield. ^{1}H NMR (401 MHz, DMSO-d_6) δ 8.15 (s, 1H), 7.91 (s, 1H), 7.90 (s, 1H), 7.49 (s, 1H), 3.12 (s, 3H), 3.03 (s, 3H), 2.69 (s, 3H). ^{13}C NMR (101 MHz, DMSO-d_6) δ 166.73, 156.41, 155.81, 142.30, 136.96, 135.44, 132.80, 123.07, 120.24, 117.83, 106.12, 40.47, 34.62, 19.19. LC-MS m/z: 305.0 (M+H)[+]. Rt = 3.8 minutes.

(*E*)-*N'*-(5-Chloro-2-cyano-4-(1-methyl-1*H*-pyrrol-2-yl)phenyl)-*N,N*-dimethylformimidamide (89c)
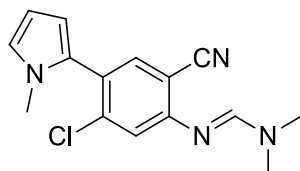
Purified by column chromatography (toluene/DCM/EtOAc, 9:1:1), followed by reverse phase column chromatography (H$_2$O/MeOH, 30 % to 100 %). White solid, 96 % yield. ^{1}H NMR (401 MHz, DMSO-d_6) δ 8.13 (s, 1H), 7.59 (s, 1H), 7.44 (s, 1H), 6.85 (dd, J = 2.6, 1.8 Hz, 1H), 6.10 – 6.02 (m, 2H), 3.42 (s, 3H), 3.11 (s, 3H), 3.03 (s, 3H). ^{13}C NMR (101 MHz, DMSO-d_6) δ 156.28, 155.86, 139.68, 136.74, 129.08, 125.33, 123.57, 119.79, 118.05, 110.18, 107.57, 105.40, 40.41, 34.58, 34.44. LC-MS m/z: 287.2 (M+H)[+]. Rt = 3.9 minutes.

(E)-N′-(5-Chloro-2-cyano-4-(1-methyl-1H-imidazol-2-yl)phenyl)-N,N-dimethylformimidamide (89d)

Purified by column chromatography (acetone/EtOAc/DCM/EtOH, 5:3:1:1), followed by reverse phase column chromatography (H$_2$O/MeOH, 30 % to 100 %). White solid, 92 % yield. ^{1}H NMR (401 MHz, DMSO-d_6) δ 8.15 (s, 1H), 7.73 (s, 1H), 7.67 (s, 1H), 7.50 (s, 1H), 6.95 (s, 1H), 3.47 (s, 3H), 3.12 (s, 3H), 3.03 (s, 3H). ^{13}C NMR (101 MHz, DMSO-d_6) δ 156.54, 156.45, 139.58, 139.42, 136.90, 129.35, 128.59, 121.76, 119.86, 117.93, 105.58, 40.46, 34.61, 31.95. LC-MS m/z: 287.7 (M+H)[+]. Rt = 2.7 minutes.

(E)-N′-(5-Chloro-2-cyano-4-(1-methyl-1H-imidazol-4-yl)phenyl)-N,N-dimethylformimidamide (89e)

Purified by column chromatography (EtOAc), followed by reverse phase column chromatography (H$_2$O/MeOH, 30 % to 100 %). White solid, 95 % yield. ^{1}H NMR (401 MHz, DMSO-d_6) δ 8.20 (s, 1H), 8.08 (s, 1H), 7.73 (d, J = 1.2 Hz, 1H), 7.71 (dd, J = 1.2, 0.5 Hz, 1H), 7.36 (s, 1H), 3.72 (s, 3H), 3.10 (s, 3H), 3.01 (s, 3H). ^{13}C NMR (101 MHz, DMSO-d_6) δ 155.90, 153.60, 138.44, 135.89, 135.13, 133.00, 126.79, 120.54, 120.28, 118.41, 105.80, 40.34, 34.54, 33.60. LC-MS m/z: 287.9 (M+H)[+]. Rt = 2.7 minutes.

(E)-N′-(5-Chloro-2-cyano-4-(4-methylthiazol-2-yl)phenyl)-N,N-dimethylformimidamide (89f)

Purified by column chromatography (toluene/DCM/EtOAc, 8:3:1), followed by reverse phase column chromatography (H$_2$O/MeOH, 30 % to 100 %). Yellow solid, 88 % yield. ^{1}H NMR (401 MHz, DMSO-d_6) δ 8.33 (s, 1H), 8.21 (s, 1H), 7.52 (s, 1H), 7.45 (q, J = 1.0 Hz, 1H), 3.13 (s, 3H), 3.05 (s, 3H), 2.45 (d, J = 1.0 Hz, 3H). ^{13}C NMR (101 MHz, DMSO-d_6) δ 160.68, 156.62, 156.14, 152.46, 136.10, 134.86, 124.78, 120.37, 117.78, 116.71, 106.23, 40.55, 34.68, 17.22. LC-MS m/z: 305.1 (M+H)$^+$. Rt = 4.4 minutes.

(*E*)-*N'*-(5-Chloro-2-cyano-4-(1-methyl-1*H*-pyrazol-4-yl)phenyl)-*N,N*-dimethylformimidamide (89g)

Purified by column chromatography (DCM/toluene/EtOAc, 4:2:1), followed by reverse phase column chromatography (H$_2$O/MeOH, 30 % to 100 %). White solid, 86 % yield. ^{1}H NMR (401 MHz, DMSO-d_6) δ 8.16 – 8.11 (m, 1H), 8.08 (s, 1H), 7.86 – 7.80 (m, 2H), 7.39 (s, 1H), 3.88 (s, 3H), 3.10 (s, 3H), 3.01 (s, 3H). ^{13}C NMR (101 MHz, DMSO-d_6) δ 155.96, 154.02, 138.50, 136.26, 133.83, 130.45, 125.02, 120.30, 118.24, 117.74, 106.01, 40.35, 39.11, 34.54. LC-MS m/z: 288.1 (M+H)$^+$. Rt = 3.0 minutes.

(*E*)-*N′*-(5-Chloro-2-cyano-4-(1-methyl-1*H*-imidazol-5-yl)phenyl)-*N,N*-dimethylformimidamide (89h)

Purified by column chromatography (EtOAc/acetone/DCM/EtOH, 5:2:1:1), followed by reverse phase column chromatography (H$_2$O/MeOH, 30 % to 100 %). White solid, 90 % yield. 1H NMR (401 MHz, DMSO-$d6$) δ 8.15 (s, 1H), 7.76 – 7.71 (m, 1H), 7.67 (s, 1H), 7.50 (s, 1H), 6.95 (d, J = 1.1 Hz,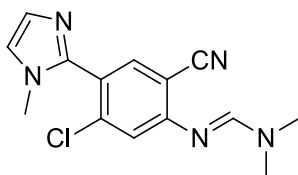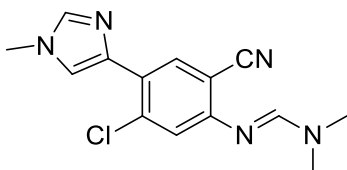 1H), 3.47 (s, 3H), 3.12 (s, 3H), 3.03 (s, 3H). ^{13}C NMR (101 MHz, DMSO-d_6) δ 156.54, 156.45, 139.58, 139.42, 136.90, 129.35, 128.59, 121.76, 119.86, 117.93, 105.57, 40.46, 34.61, 31.95. LC-MS m/z: 288.1 (M+H)$^+$. Rt = 2.6 minutes.

(*E*)-*N*′-(5-Chloro-2-cyano-4-(1,2-dimethyl-1*H*-imidazol-5-yl)phenyl)-*N*,*N*-dimethylformimidamide (89i)
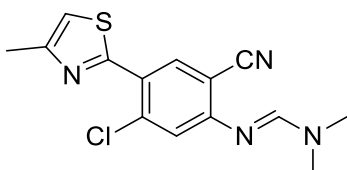

Purified by column chromatography (EtOAc/EtOH, 8:2), followed by reverse phase column chromatography (H$_2$O/MeOH, 30 % to 100 %). White solid, 80 % yield. ^{1}H NMR (401 MHz, DMSO-d_6) δ 8.15 (s, 1H), 7.61 (s, 1H), 7.49 (s, 1H), 6.79 (s, 1H), 3.32 (s, 3H), 3.12 (s, 3H), 3.03 (s, 3H), 2.34 (s, 3H). ^{13}C NMR (101 MHz, DMSO-d_6) δ 156.40, 156.39, 145.68, 139.67, 136.92, 128.61, 127.22, 122.53, 119.85, 117.96, 105.56, 40.45, 34.61, 31.10, 13.68. LC-MS m/z: 302.2 (M+H)$^+$. Rt = 2.7 minutes.

(*E*)-*N*′-(5-Chloro-2-cyano-4-(1-methyl-1*H*-pyrazol-5-yl)phenyl)-*N*,*N*-dimethylformimidamide (89j)
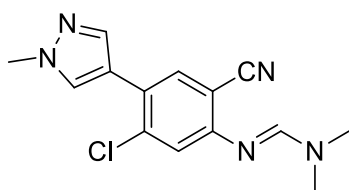

Purified by column chromatography (DCM/EtOAc, 6:4), followed by reverse phase column chromatography (H$_2$O/MeOH, 30 % to 100 %). White solid, 93 % yield. ^{1}H NMR (401 MHz, DMSO-d_6) δ 8.17 (s, 1H), 7.71 (s, 1H), 7.52 (s, 1H), 7.49 (d, *J* = 1.8 Hz, 1H), 6.33 (d, *J* = 1.8 Hz, 1H), 3.65 (s, 3H), 3.13 (s, 3H), 3.04 (s, 3H). ^{13}C NMR (101 MHz, DMSO-d_6) δ 156.84, 156.54, 138.88, 138.70, 138.28, 136.44, 122.42, 119.85, 117.85, 107.87, 105.64, 40.48, 37.21, 34.63. LC-MS m/z: 288.2 (M+H)$^+$. Rt = 3.4 minutes.

(*E*)-*N*′-(5-Chloro-2-cyano-4-(4,5-dimethylthiazol-2-yl)phenyl)-*N*,*N*-dimethylformimidamide (89k)
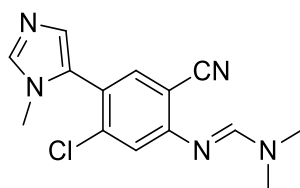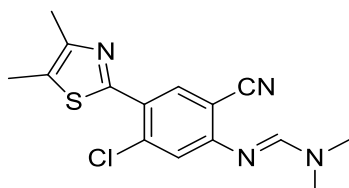
Purified by column chromatography (toluene/DCM/EtOAc, 8:3:1.5), followed by reverse phase column chromatography (H$_2$O/MeOH, 30 % to 100 %). Yellow solid, 70 % yield. ^{1}H NMR (401 MHz, DMSO-d_6) δ 8.28 (s, 1H), 8.19 (s, 1H), 7.49 (s, 1H), 3.13 (s, 3H), 3.04 (s, 3H), 2.40 (d, J = 0.7 Hz, 3H), 2.34 (d, J = 0.7 Hz, 3H). ^{13}C NMR (101 MHz, DMSO-d_6) δ 156.53, 156.41, 155.87, 148.42, 135.78, 134.31, 128.71, 124.98, 120.32, 117.81, 106.23, 40.53, 34.66, 14.92, 11.24. LC-MS m/z: 319.2 (M+H)$^+$. Rt = 4.5 minutes.

(*E*)-*N*′-(5-Chloro-2-cyano-4-(1-methyl-3-(trifluoromethyl)-1*H*-pyrazol-5-yl)phenyl)-*N*,*N*-dimethylformimidamide (89l)
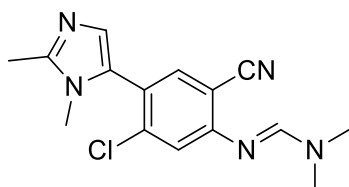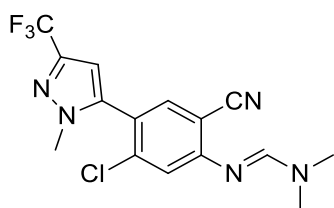

Purified by column chromatography (toluene/DCM/EtOAc, 8:2:1), followed by reverse phase column chromatography (H$_2$O/MeOH, 30 % to 100 %). White solid, 80 % yield. ^{1}H NMR (401 MHz, DMSO-d_6) δ 8.20 (s, 1H), 7.84 (s, 1H), 7.56 (s, 1H), 6.87 (s, 1H), 3.74 (s, 3H), 3.13 (s, 3H), 3.05 (s, 3H). ^{13}C NMR (101 MHz, DMSO-d_6) δ 157.44, 156.71, 140.90, 139.92 (q, J = 37.5 Hz), 138.85, 136.82, 121.92 (q, J = 268.2 Hz), 120.51, 119.83, 117.74, 106.63 (q, J = 2.0 Hz), 105.72, 40.53, 38.06, 34.66. LC-MS m/z: 355.8 (M+H)$^+$. Rt = 4.5 minutes.

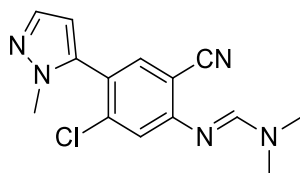**(*E*)-*N*′-(5-Chloro-2-cyano-4-(3-methylthiophen-2-yl)phenyl)-*N*,*N*-dimethylformimidamide (89m)**
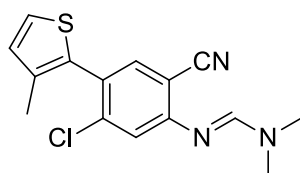
Purified by column chromatography (toluene/DCM/EtOAc, 10:2:1), followed by reverse phase column chromatography (H$_2$O/MeOH, 30 % to 100 %). White solid, 87 % yield. ^{1}H NMR (401 MHz, DMSO-d_6) δ 8.15 (s, 1H), 7.63 (s, 1H), 7.54 (d, J = 5.1 Hz, 1H), 7.47 (s, 1H), 7.00 (d, J = 5.1 Hz, 1H), 3.12 (s, 3H), 3.03 (s, 3H), 2.05 (s, 3H). ^{13}C NMR (101 MHz, DMSO-d_6) δ 156.42, 156.20, 139.38, 136.79, 136.34, 132.44, 130.30, 125.92, 125.61, 119.91, 117.90, 105.53, 40.48, 34.60, 14.72. LC-MS m/z: 303.7 (M+H)$^+$. Rt = 4.5 minutes.

Cyclization leading to 90a–90m

A starting material (**89a-89m**, 0.7 mmol) and 5-aminobenzothiazole (1.1 eq) were suspended in AcOH (3 ml) and heated with stirring at 95 °C for 1 h. The mixture was cooled to room temperature, leading to a precipitation of a solid. The slurry was diluted with distilled H_2O (15 ml), and the solid was collected on a sintered funnel. Further purification of the solid was performed as specified below.

***N*-(7-Chloro-6-(thiophen-2-yl)quinazolin-4-yl)benzo[*d*]thiazol-5-amine (90a)**
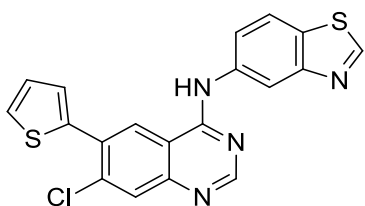
Purified by column chromatography (EtOAc/acetonitrile, 6:1), followed by recrystallization from EtOAc. White solid, 81 % yield. ^{1}H NMR (401 MHz, DMSO-d_6) δ 10.23 (s, 1H), 9.42 (s, 1H), 8.87 (s, 1H), 8.69 (d, J = 2.0 Hz, 1H), 8.67 (s, 1H), 8.17 (d, J = 8.7 Hz, 1H), 8.00 (s, 1H), 7.92 (dd, J = 8.7, 2.1 Hz, 1H), 7.81 (dd, J = 5.1, 1.2 Hz, 1H), 7.56 (dd, J = 3.6, 1.3 Hz, 1H), 7.28 (dd, J = 5.1, 3.6 Hz, 1H). ^{13}C NMR (101 MHz, DMSO-d_6) δ 158.08, 157.52, 156.35, 153.96, 150.09, 138.74, 137.82, 136.64, 131.36, 129.59, 129.36, 128.82, 128.57, 127.92, 126.52, 122.48, 121.64, 116.86, 114.67. LC-MS m/z: 395.1 (M+H)[+]. Rt = 4.1 minutes. HRMS calcd for $C_{19}H_{12}ClN_4S_2$ m/z: 395.01864 (M+H)[+], found 395.01885.

***N*-(7-Chloro-6-(2-methylthiazol-5-yl)quinazolin-4-yl)benzo[*d*]thiazol-5-amine (90b)**
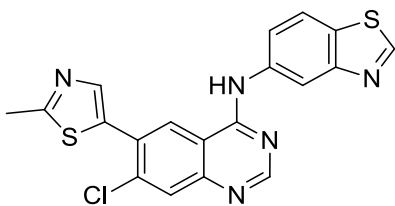
Purified by column chromatography (EtOAc/acetonitrile, 5:2), followed by recrystallization from EtOH. Yellow solid, 90 % yield. ^{1}H NMR (401 MHz, DMSO-d_6) δ 10.18 (s, 1H), 9.43 (s, 1H), 8.88 (s, 1H), 8.68 (d, J = 2.0 Hz, 1H), 8.67 (s, 1H), 8.17 (d, J = 8.7 Hz, 1H), 8.05 (s, 1H), 7.99 (s, 1H), 7.91 (dd, J = 8.7, 2.1 Hz, 1H), 2.76 (s, 3H). ^{13}C NMR (101 MHz, DMSO-d_6) δ 167.73, 158.01, 157.56, 156.54, 153.95, 150.37, 143.26, 137.71, 136.52, 133.34, 129.42, 128.79, 128.49, 126.56, 122.51, 121.57, 116.82, 114.66, 19.28. LC-MS m/z: 410.1 (M+H)[+]. Rt = 3.7 minutes. HRMS calcd for $C_{19}H_{13}ClN_5S_2$ m/z: 410.02954 (M+H)[+], found 410.02970.

N-(7-Chloro-6-(1-methyl-1H-pyrrol-2-yl)quinazolin-4-yl)benzo[d]thiazol-5-amine (90c)

Purified by column chromatography (EtOAc), followed by recrystallization from EtOH. Yellow solid, 85 % yield. ^{1}H NMR (401 MHz, DMSO-d_6) δ 10.14 (s, 1H), 9.41 (s, 1H), 8.75 (s, 1H), 8.74 (s, 1H), 8.69 (s, 1H), 8.15 (d, J = 8.7 Hz, 1H), 7.98 (s, 1H), 7.94 (dd, J = 8.8, 2.1 Hz, 1H), 6.97 (dd, J = 2.7, 1.8 Hz, 1H), 6.25 (dd, J = 3.6, 1.8 Hz, 1H), 6.17 (dd, J = 3.6, 2.7 Hz, 1H), 3.52 (s, 3H). ^{13}C NMR (101 MHz, DMSO-d_6) δ 158.09, 157.46, 156.29, 153.95, 150.42, 139.09, 137.95, 130.64, 129.79, 129.17, 128.04, 127.92, 123.95, 122.45, 121.39, 116.56, 114.33, 110.85, 107.72, 34.60. LC-MS m/z: 392.2 (M+H)$^+$. Rt = 3.9 minutes. HRMS calcd for $C_{20}H_{15}ClN_5S$ m/z: 392.07312 (M+H)$^+$, found 392.07343.

N-(7-Chloro-6-(1-methyl-1H-imidazol-2-yl)quinazolin-4-yl)benzo[d]thiazol-5-amine (90d)
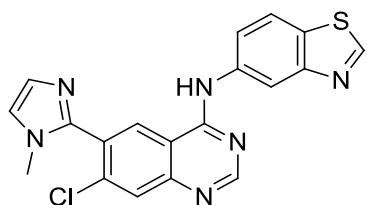
Purified by column chromatography (EtOAc/acetonitrile, 6:1). White solid, 84 % yield. ^{1}H NMR (401 MHz, DMSO-d_6) δ 10.19 (s, 1H), 9.42 (s, 1H), 8.80 (s, 1H), 8.73 (d, J = 2.0 Hz, 1H), 8.71 (s, 1H), 8.16 (d, J = 8.7 Hz, 1H), 8.03 (s, 1H), 7.93 (dd, J = 8.7, 2.1 Hz, 1H), 7.86 (s, 1H), 7.14 (d, J = 1.1 Hz, 1H), 3.58 (s, 3H). ^{13}C NMR (101 MHz, DMSO-d_6) δ 158.13, 157.53, 156.64, 153.95, 150.92, 139.75, 138.73, 137.83, 129.81, 129.34, 129.29, 128.35, 128.25, 127.22, 122.49, 121.44, 116.65, 114.39, 32.12. LC-MS m/z: 393.2 (M+H)$^+$. Rt = 2.9 minutes. HRMS calcd for $C_{19}H_{14}ClN_6S$ m/z: 393.06837 (M+H)$^+$, found 393.06863.

N-(7-Chloro-6-(1-methyl-1H-imidazol-4-yl)quinazolin-4-yl)benzo[d]thiazol-5-amine (90e)
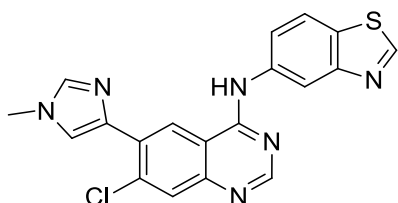
Purified by recrystallization from MeOH/acetone. Yellow solid, 76 % yield. ^{1}H NMR (401 MHz, DMSO-d_6) δ 10.41 (s, 1H), 9.42 (s, 1H), 9.19 (s, 1H), 8.69 (d, J = 2.0 Hz, 1H), 8.60 (s, 1H), 8.15 (d, J = 8.7 Hz, 1H), 7.96 (dd, J = 8.7, 2.1 Hz, 1H), 7.92 (s, 1H), 7.90 (s, 1H), 7.86 (s, 1H), 3.79 (s, 3H). ^{13}C NMR (101 MHz, DMSO-d_6) δ 158.26, 157.32, 155.50, 153.95, 149.09, 138.70, 138.17, 136.75, 135.58, 131.85, 129.11, 128.65, 123.88, 122.29, 121.89, 121.84, 116.96, 114.94, 33.70. LC-MS m/z: 393.2 (M+H)$^+$. Rt = 2.9 minutes. HRMS calcd for $C_{19}H_{14}ClN_6S$ m/z: 393.06837 (M+H)$^+$, found 393.06867.

N-(7-Chloro-6-(4-methylthiazol-2-yl)quinazolin-4-yl)benzo[d]thiazol-5-amine (90f)
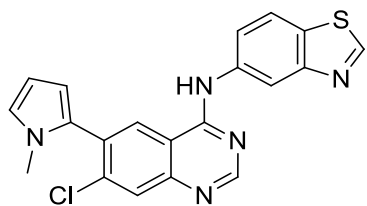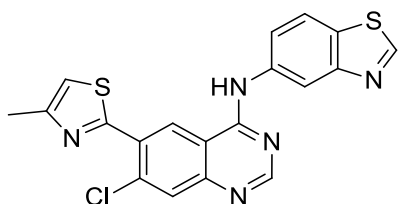

Purified by column chromatography (EtOAc), followed by recrystallization from EtOH. Yellow solid, 86 % yield. ^{1}H NMR (400 MHz, DMSO-d_6) δ 10.45 (s, 1H), 9.42 (s, 1H), 9.20 (s, 1H), 8.68 (s, 1H), 8.67 (d, J = 2.0 Hz, 1H), 8.17 (d, J = 8.7 Hz, 1H), 8.03 (s, 1H), 7.92 (dd, J = 8.7, 2.1 Hz, 1H), 7.61 (q, J = 1.0 Hz, 1H), 2.54 (d, J = 1.0 Hz, 3H). ^{13}C NMR (101 MHz, DMSO-d_6) δ 161.64, 158.53, 157.48, 156.92, 153.94, 153.02, 150.87, 137.78, 135.65, 130.27, 129.50, 129.16, 126.99, 122.44, 121.88, 117.83, 117.13, 114.72, 17.33. LC-MS m/z: 410.1 (M+H)$^+$. Rt = 4.1 minutes. HRMS calcd for $C_{19}H_{13}ClN_5S_2$ m/z: 410.02954 (M+H)$^+$, found 410.02967.

***N*-(7-Chloro-6-(1-methyl-1*H*-pyrazol-4-yl)quinazolin-4-yl)benzo[*d*]thiazol-5-amine (90g)**
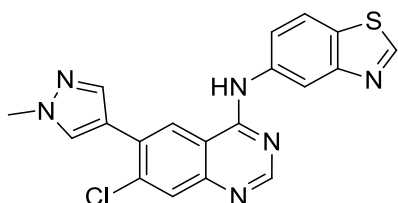
Purified by recrystallization from MeOH/acetone. White solid, 82 % yield. ^{1}H NMR (401 MHz, DMSO-d_6) δ 10.09 (s, 1H), 9.43 (s, 1H), 8.78 (s, 1H), 8.69 (d, *J* = 1.9 Hz, 1H), 8.62 (s, 1H), 8.29 (s, 1H), 8.18 (d, *J* = 8.7 Hz, 1H), 8.00 (s, 1H), 7.96 – 7.89 (m, 2H), 3.97 (s, 3H). ^{13}C NMR (101 MHz, DMSO-d_6) δ 157.90, 157.52, 155.66, 153.99, 149.14, 139.26, 137.88, 136.44, 131.13, 130.25, 129.31, 128.65, 124.03, 122.50, 121.66, 118.48, 116.83, 114.79, 39.20. LC-MS m/z: 393.1 (M+H)[+]. Rt = 3.3 minutes. HRMS calcd for C$_{19}$H$_{14}$N$_6$ClS m/z: 393.06837 (M+H)[+], found 393.06883.

***N*-(7-Chloro-6-(1-methyl-1*H*-imidazol-5-yl)quinazolin-4-yl)benzo[*d*]thiazol-5-amine (90h)**
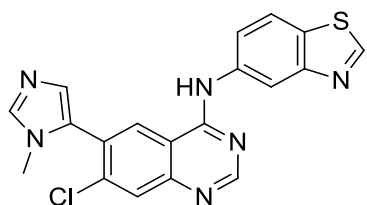
Purified by column chromatography (EtOAc/acetone/DCM/EtOH, 4:4:1:1). Yellow solid, 85 % yield. ^{1}H NMR (401 MHz, DMSO-d_6) δ 10.15 (s, 1H), 9.42 (s, 1H), 8.78 (s, 1H), 8.72 (d, *J* = 2.1 Hz, 1H), 8.71 (s, 1H), 8.16 (d, *J* = 8.7 Hz, 1H), 8.03 (s, 1H), 7.92 (dd, *J* = 8.8, 2.1 Hz, 1H), 7.86 (s, 1H), 7.14 (s, 1H), 3.57 (s, 3H). ^{13}C NMR (101 MHz, DMSO-d_6) δ 158.11, 157.53, 156.64, 153.95, 150.92, 139.75, 138.73, 137.82, 129.80, 129.35, 129.30, 128.31, 128.25, 127.23, 122.50, 121.41, 116.62, 114.38, 32.11. LC-MS m/z: 393.0 (M+H)[+]. Rt = 2.9 minutes. HRMS calcd for C$_{19}$H$_{14}$N$_6$ClS m/z: 393.06837 (M+H)[+], found 393.06871.

***N*-(7-Chloro-6-(1,2-dimethyl-1*H*-imidazol-5-yl)quinazolin-4-yl)benzo[*d*]thiazol-5-amine (90i)**
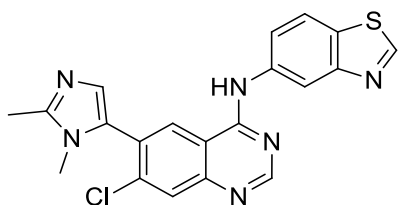
Purified by column chromatography (EtOAc/acetone/DCM/EtOH, 4:4:1:1). Yellow solid, 75 % yield. ^{1}H NMR (401 MHz, DMSO-d_6) δ 10.14 (s, 1H), 9.42 (s, 1H), 8.76 – 8.69 (m, 3H), 8.16 (d, *J* = 8.7 Hz, 1H), 8.02 (s, 1H), 7.93 (dd, *J* = 8.8, 2.1 Hz, 1H), 6.98 (s, 1H), 3.42 (s, 3H), 2.41 (s, 3H). ^{13}C NMR (101 MHz, DMSO-d_6) δ 158.12, 157.52, 156.56, 153.96, 150.83, 146.08, 138.88, 137.86, 129.37, 129.27, 128.29, 128.21, 127.94, 127.72, 122.50, 121.40, 116.60, 114.41, 31.30, 13.67. LC-MS m/z: 406.8 (M+H)[+]. Rt = 2.9 minutes. HRMS calcd for $C_{20}H_{16}N_6ClS$ m/z: 407.08402 (M+H)[+], found 407.08436.

***N*-(7-Chloro-6-(1-methyl-1*H*-pyrazol-5-yl)quinazolin-4-yl)benzo[*d*]thiazol-5-amine (90j)**
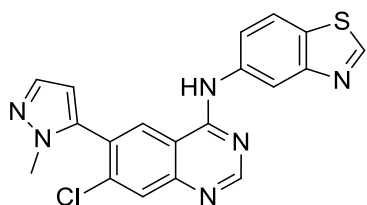
Purified by recrystallization from MeOH. White solid, 88 % yield. ^{1}H NMR (401 MHz, DMSO-d_6) δ 10.15 (s, 1H), 9.42 (s, 1H), 8.81 (s, 1H), 8.74 – 8.71 (m, 2H), 8.16 (d, *J* = 8.7 Hz, 1H), 8.05 (s, 1H), 7.92 (dd, *J* = 8.7, 1.9 Hz, 1H), 7.61 (d, *J* = 1.9 Hz, 1H), 6.53 (d, *J* = 1.9 Hz, 1H), 3.74 (s, 3H). ^{13}C NMR (101 MHz, DMSO-d_6) δ 158.19, 157.55, 156.83, 153.96, 151.12, 139.38, 138.46, 138.00, 137.78, 129.35, 128.35, 127.94, 127.92, 122.53, 121.38, 116.63, 114.37, 108.33, 37.36. LC-MS m/z: 393.2 (M+H)[+]. Rt = 3.7 minutes. HRMS calcd for $C_{19}H_{14}N_6ClS$ m/z: 393.06837 (M+H)[+], found 393.06861.

N-(7-Chloro-6-(4,5-dimethylthiazol-2-yl)quinazolin-4-yl)benzo[d]thiazol-5-amine (90k)
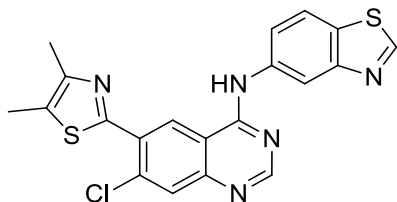
Purified by recrystallization from MeOH. Yellow solid, 92 % yield. ^{1}H NMR (401 MHz, DMSO-d_6) δ 10.45 (s, 1H), 9.42 (s, 1H), 9.17 (s, 1H), 8.67 (s, 2H), 8.17 (d, J = 8.6 Hz, 1H), 8.01 (s, 1H), 7.92 (dd, J = 8.6, 1.8 Hz, 1H), 2.47 (s, 3H), 2.43 (s, 3H). ^{13}C NMR (101 MHz, DMSO-d_6) δ 158.49, 157.48, 157.34, 156.76, 153.93, 150.61, 149.01, 137.79, 135.48, 130.35, 129.94, 129.47, 129.08, 126.43, 122.44, 121.89, 117.12, 114.75, 15.01, 11.34. LC-MS m/z: 423.8 (M+H)$^+$. Rt = 4.3 minutes. HRMS calcd for $C_{20}H_{15}N_5ClS_2$ m/z: 424.04519 (M+H)$^+$, found 424.04541. Na-HRMS calcd for $C_{20}H_{14}N_5ClNaS_2$ m/z: 446.02714 (M+Na)$^+$, found 446.02723.

N-(7-Chloro-6-(1-methyl-3-(trifluoromethyl)-1H-pyrazol-5-yl)quinazolin-4-yl)benzo[d]thiazol-5-amine (90l)
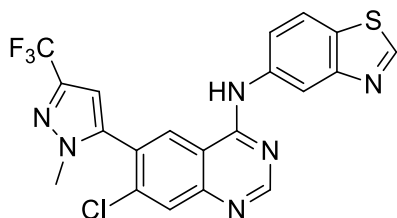
Purified by recrystallization from MeOH. White solid, 87 % yield. ^{1}H NMR (401 MHz, DMSO-d_6) δ 10.14 (s, 1H), 9.43 (s, 1H), 8.86 (s, 1H), 8.75 (s, 1H), 8.72 (d, J = 2.0 Hz, 1H), 8.17 (d, J = 8.7 Hz, 1H), 8.09 (s, 1H), 7.91 (dd, J = 8.6, 2.1 Hz, 1H), 7.08 (s, 1H), 3.84 (s, 3H). ^{13}C NMR (101 MHz, DMSO-d_6) δ 158.20, 157.61, 157.17, 153.96, 151.54, 141.66, 140.23 (q, J = 37.5 Hz), 137.69, 137.66, 129.45, 128.55, 128.49, 126.02, 121.92 (q, J = 268.2 Hz), 122.59, 121.33, 116.62, 114.38, 106.98 (q, J = 2.0 Hz), 38.24. LC-MS m/z: 460.8 (M+H)$^+$. Rt = 4.3 minutes. HRMS calcd for $C_{20}H_{13}N_6ClF_3S$ m/z: 461.05575 (M+H)$^+$, found 461.05596.

N-(7-Chloro-6-(3-methylthiophen-2-yl)quinazolin-4-yl)benzo[d]thiazol-5-amine (90m)
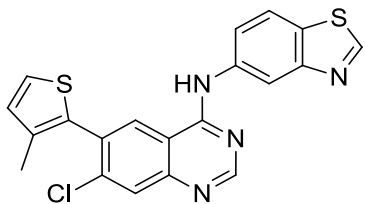

Purified by recrystallization from MeOH. White solid, 91 % yield. ^{1}H NMR (401 MHz, DMSO-d_6) δ 10.16 (s, 1H), 9.42 (s, 1H), 8.80 (s, 1H), 8.72 (d, J = 1.8 Hz, 1H), 8.70 (s, 1H), 8.16 (d, J = 8.7 Hz, 1H), 8.02 (s, 1H), 7.93 (dd, J = 8.7, 1.9 Hz, 1H), 7.65 (d, J = 5.1 Hz, 1H), 7.10 (d, J = 5.1 Hz, 1H), 2.13 (s, 3H). ^{13}C NMR (101 MHz, DMSO-d_6) δ 158.08, 157.46, 156.50, 153.96, 150.68, 138.79, 137.87, 136.81, 133.00, 131.20, 130.37, 129.27, 128.21, 128.15, 126.20, 122.45, 121.48, 116.70, 114.35, 14.75. LC-MS m/z: 409.2 (M+H)[+]. Rt = 4.2 minutes. HRMS calcd for $C_{20}H_{14}N_4ClS_2$ m/z: 409.03429 (M+H)[+], found 409.03453.

Pd-catalyzed reductive hydrodechlorination leading to 91a–91i, 91k and 91m

To a starting material (**90a–90i**, **90k** and **90m**, 0.35 mmol) were added HCOONH$_4$ (12 eq), Pd$_2$(dba)$_3$ (4 mol%) and SPhos (12 mol%). The solid mixture was purged with argon and suspended in 1,4-dioxane (4.2 ml) and distilled H$_2$O (1.7 ml). The resulting suspension was heated with stirring at 95 °C for 24 h. The mixture was cooled to room temperature, diluted with EtOAc and filtered to remove solid impurities. The solvent was removed under reduced pressure, purifying the residue as described below.

N-(6-(Thiophen-2-yl)quinazolin-4-yl)benzo[d]thiazol-5-amine (91a)


Purified by column chromatography (EtOAc). Yellow solid, 85 % yield. ^{1}H NMR (401 MHz, DMSO-d_6) δ 10.16 (s, 1H), 9.43 (s, 1H), 8.85 (d, J = 1.8 Hz, 1H), 8.70 (d, J = 1.9 Hz, 1H), 8.63 (s, 1H), 8.19 (d, J = 8.7 Hz, 1H), 8.18 (dd, J = 8.7, 2.0 Hz, 1H), 7.95 (dd, J = 8.7, 2.0 Hz, 1H), 7.84 (d, J = 8.7 Hz, 1H), 7.77 (dd, J = 3.6, 1.1 Hz, 1H), 7.69 (dd, J = 5.1, 1.1 Hz, 1H), 7.26 (dd, J = 5.1, 3.6 Hz, 1H). ^{13}C NMR (101 MHz, DMSO-d_6) δ 158.25, 158.23, 157.47, 154.86, 154.02, 149.60, 143.00, 138.10, 132.41, 131.33, 129.19, 129.14, 127.26, 125.48,

122.46, 121.87, 119.21, 116.95, 116.02. LC-MS m/z: 360.7 (M+H)$^+$. Rt = 3.5 minutes. HRMS calcd for $C_{19}H_{13}N_4S_2$ m/z: 361.05761 (M+H)$^+$, found 361.05782.

N-(6-(2-Methylthiazol-5-yl)quinazolin-4-yl)benzo[*d*]thiazol-5-amine (91b)
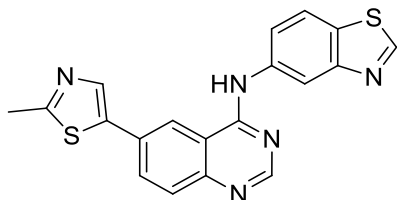
Purified by column chromatography (EtOAc/EtOH, 10:1). Yellow solid, 80 % yield. ^{1}H NMR (401 MHz, DMSO-d_6) δ 10.13 (s, 1H), 9.43 (s, 1H), 8.79 (s, 1H), 8.69 (d, *J* = 1.9 Hz, 1H), 8.64 (s, 1H), 8.25 (s, 1H), 8.19 (d, *J* = 8.7 Hz, 1H), 8.14 (dd, *J* = 8.7, 1.8 Hz, 1H), 7.94 (dd, *J* = 8.7, 1.9 Hz, 1H), 7.84 (d, *J* = 8.7 Hz, 1H), 2.74 (s, 3H). ^{13}C NMR (101 MHz, DMSO-d_6) δ 166.19, 164.39, 158.18, 157.50, 155.12, 154.01, 149.78, 139.78, 138.00, 137.89, 131.69, 129.67, 129.27, 122.49, 121.82, 120.36, 116.94, 115.98, 19.58. LC-MS m/z: 375.8 (M+H)$^+$. Rt = 3.2 minutes. HRMS calcd for $C_{19}H_{14}N_5S_2$ m/z: 376.06851 (M+H)$^+$, found 376.06856.

N-(6-(1-Methyl-1*H*-pyrrol-2-yl)quinazolin-4-yl)benzo[*d*]thiazol-5-amine (91c)
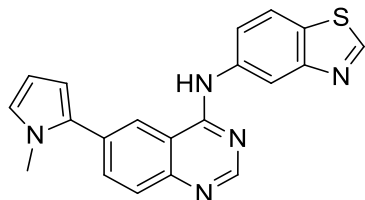
Purified by column chromatography (EtOAc). Orange solid, 83 % yield. ^{1}H NMR (401 MHz, DMSO-d_6) δ 10.02 (s, 1H), 9.42 (s, 1H), 8.75 (d, *J* = 1.9 Hz, 1H), 8.65 (s, 1H), 8.64 (d, *J* = 1.6 Hz, 1H), 8.17 (d, *J* = 8.7 Hz, 1H), 7.98 (dd, *J* = 3.6, 1.9 Hz, 1H), 7.96 (dd, *J* = 3.7, 1.9 Hz, 1H), 7.84 (d, *J* = 8.6 Hz, 1H), 6.97 (d, *J* = 4.4 Hz, 1H), 6.39 (dd, *J* = 3.6, 1.8 Hz, 1H), 6.17 (dd, *J* = 3.5, 2.7 Hz, 1H), 3.77 (s, 3H).^{13}C NMR (101 MHz, DMSO-d_6) δ 158.14, 157.40, 154.67, 154.02, 148.86, 138.28, 133.86, 133.14, 131.64, 128.95, 128.44, 125.47, 122.42, 121.78, 121.57, 116.57, 115.70, 110.22, 108.11, 35.47. LC-MS m/z: 357.7 (M+H)$^+$. Rt = 3.4 minutes. HRMS calcd for $C_{20}H_{16}N_5S$ m/z: 358.11209 (M+H)$^+$, found 358.11232.

N-(6-(1-Methyl-1H-imidazol-2-yl)quinazolin-4-yl)benzo[d]thiazol-5-amine (91d)

Purified by column chromatography (acetone/EtOH/DCM, 6:2:1), followed by recrystallization from EtOAc. White solid, 78 % yield. ^{1}H NMR (401 MHz, DMSO-d_6) δ 10.46 (s, 1H), 9.43 (s, 1H), 8.92 (s, 1H), 8.78 (d, J = 1.6 Hz, 1H), 8.65 (s, 1H), 8.16 (d, J = 8.7 Hz, 1H), 8.05 (dd, J = 8.7, 1.7 Hz, 1H), 8.00 (dd, J = 8.6, 1.5 Hz, 1H), 7.86 (d, J = 8.6 Hz, 1H), 7.82 (s, 1H), 7.30 (s, 1H), 3.86 (s, 3H). ^{13}C NMR (101 MHz, DMSO-d_6) δ 158.32, 157.33, 155.06, 153.95, 149.41, 140.69, 138.28, 133.42, 132.49, 129.16, 128.98, 128.70, 128.29, 122.49, 122.26, 121.90, 116.90, 115.88, 33.06. LC-MS m/z: 358.7 (M+H)$^+$. Rt = 2.6 minutes. HRMS calcd for C$_{19}$H$_{15}$N$_6$S m/z: 359.10734 (M+H)$^+$, found 359.10759.

N-(6-(1-Methyl-1H-imidazol-4-yl)quinazolin-4-yl)benzo[d]thiazol-5-amine (91e)

Purified by column chromatography (EtOAc/EtOH/DCM/acetone, 5:2:2:1), followed by recrystallization from EtOAc. Yellow solid, 86 % yield. ^{1}H NMR (401 MHz, DMSO-d_6) δ 10.16 (s, 1H), 9.42 (s, 1H), 8.96 (d, J = 1.5 Hz, 1H), 8.74 (d, J = 1.9 Hz, 1H), 8.59 (s, 1H), 8.27 (dd, J = 8.7, 1.7 Hz, 1H), 8.16 (d, J = 8.5 Hz, 1H), 8.01 (dd, J = 8.7, 2.0 Hz, 1H), 7.82 (d, J = 1.1 Hz, 1H), 7.79 (d, J = 8.7 Hz, 1H), 7.77 (d, J = 0.7 Hz, 1H), 3.77 (s, 3H). ^{13}C NMR (101 MHz, DMSO-d_6) δ 158.22, 157.31, 154.07, 154.02, 149.09, 140.58, 139.36, 138.48, 133.43, 130.47, 128.78, 128.51, 122.31, 121.68, 118.58, 117.51, 116.60, 116.08, 33.69. LC-MS m/z: 359.2 (M+H)$^+$. Rt = 2.8 minutes. HRMS calcd for C$_{19}$H$_{15}$N$_6$S m/z: 359.10734 (M+H)$^+$, found 359.10766.

N-(6-(4-Methylthiazol-2-yl)quinazolin-4-yl)benzo[d]thiazol-5-amine (91f)
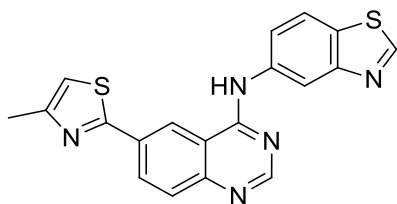
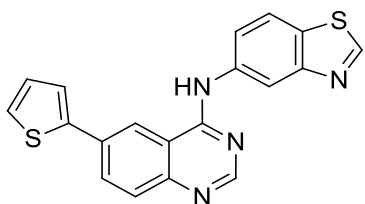Purified by column chromatography (EtOAc/EtOH/DCM, 10:1:1), followed by recrystallization from EtOAc. Yellow solid, 79 % yield. ^{1}H NMR (401 MHz, DMSO-d_6) δ 10.39 (s, 1H), 9.43 (s, 1H), 9.11 (s, 1H), 8.69 (d, J = 1.9 Hz, 1H), 8.66 (s, 1H), 8.40 (dd, J = 8.7, 1.8 Hz, 1H), 8.19 (d, J = 8.7 Hz, 1H), 7.95 (dd, J = 8.7, 2.0 Hz, 1H), 7.89 (d, J = 8.7 Hz, 1H), 7.46 (s, 1H), 2.50 (s, 3H). ^{13}C NMR (101 MHz, DMSO-d_6) δ 165.92, 164.32, 158.62, 157.43, 155.69, 154.01, 153.99, 151.10, 138.01, 131.58, 131.17, 129.32, 122.41, 122.04, 121.06, 117.18, 116.16, 115.93, 17.46. LC-MS m/z: 376.1 (M+H)$^+$. Rt = 3.4 minutes. HRMS calcd for $C_{19}H_{14}N_5S_2$ m/z: 376.06851 (M+H)$^+$, found 376.06873.

N-(6-(1-Methyl-1H-pyrazol-4-yl)quinazolin-4-yl)benzo[d]thiazol-5-amine (91g)
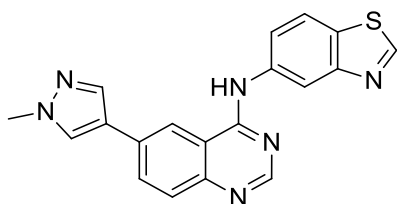
Purified by column chromatography (EtOAc/acetone/DCM/EtOH, 7:1:1:1), followed by recrystallization from EtOAc. White solid, 83 % yield. ^{1}H NMR (401 MHz, DMSO-d_6) δ 9.93 (s, 1H), 9.43 (s, 1H), 8.75 (d, J = 1.6 Hz, 1H), 8.73 (d, J = 1.9 Hz, 1H), 8.60 (s, 1H), 8.30 (s, 1H), 8.19 (d, J = 8.7 Hz, 1H), 8.12 – 8.08 (m, 2H), 7.96 (dd, J = 8.7, 2.0 Hz, 1H), 7.80 (d, J = 8.6 Hz, 1H), 3.94 (s, 3H). ^{13}C NMR (101 MHz, DMSO-d_6) δ 157.98, 157.48, 154.19, 154.06, 148.71, 138.22, 136.98, 131.39, 131.22, 129.00, 128.87, 128.85, 122.49, 121.88, 121.61, 117.90, 116.62, 116.03, 39.29. LC-MS m/z: 359.1 (M+H)$^+$. Rt = 3.1 minutes. HRMS calcd for $C_{19}H_{15}N_6S$ m/z: 359.10734 (M+H)$^+$, found 359.10758.

N-(6-(1-Methyl-1H-imidazol-5-yl)quinazolin-4-yl)benzo[d]thiazol-5-amine (91h)

Purified by column chromatography (acetone/EtOH/DCM, 4:1.5:1). White solid, 74 % yield. ^{1}H NMR (401 MHz, DMSO-d_6) δ 10.05 (s, 1H), 9.43 (s, 1H), 8.73 (d, J = 1.7 Hz, 1H), 8.69 (d, J = 1.5 Hz, 1H), 8.67 (s, 1H), 8.18 (d, J = 8.7 Hz, 1H), 8.02 (dd, J = 8.6, 1.5 Hz, 1H), 7.95 (dd, J = 8.7, 1.8 Hz, 1H), 7.89 (d, J = 8.6 Hz, 1H), 7.84 (s, 1H), 7.27 (s, 1H), 3.81 (s, 3H). ^{13}C NMR (101 MHz, DMSO-d_6) δ 158.21, 157.48, 155.11, 154.01, 149.39, 149.03, 138.11, 133.45, 132.49, 129.13, 128.99, 128.79, 128.32, 122.48, 122.24, 121.66, 116.74, 115.76, 32.96. LC-MS m/z: 358.8 (M+H)[+]. Rt = 2.6 minutes. HRMS calcd for $C_{19}H_{15}N_6S$ m/z: 359.10734 (M+H)[+], found 359.10751.

N-(6-(1,2-Dimethyl-1H-imidazol-5-yl)quinazolin-4-yl)benzo[d]thiazol-5-amine (91i)

Purified by column chromatography (acetone/EtOH/DCM, 4:1.5:1). White solid, 70 % yield. ^{1}H NMR (401 MHz, DMSO-d_6) δ 10.04 (s, 1H), 9.42 (s, 1H), 8.73 (d, J = 1.9 Hz, 1H), 8.67 (s, 1H), 8.64 (d, J = 1.5 Hz, 1H), 8.17 (d, J = 8.7 Hz, 1H), 7.96 (d, J = 1.6 Hz, 1H), 7.94 (d, J = 1.7 Hz, 1H), 7.87 (d, J = 8.6 Hz, 1H), 7.08 (s, 1H), 3.65 (s, 3H), 2.42 (s, 3H). ^{13}C NMR (101 MHz, DMSO) δ 158.18, 157.43, 155.00, 154.01, 149.27, 146.76, 138.19, 133.55, 132.57, 129.07, 128.99, 128.74, 127.11, 122.45, 122.20, 121.64, 116.69, 115.81, 31.86, 13.89. LC-MS m/z: 372.7 (M+H)[+]. Rt = 2.6 minutes. HRMS calcd for $C_{20}H_{17}N_6S$ m/z: 373.12299 (M+H)[+], found 373.12308.

N-(6-(4,5-Dimethylthiazol-2-yl)quinazolin-4-yl)benzo[*d*]thiazol-5-amine (91k)
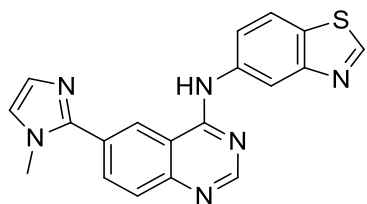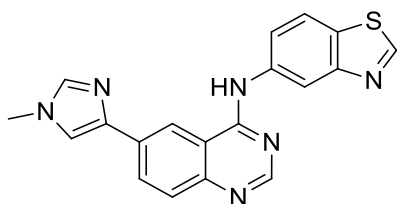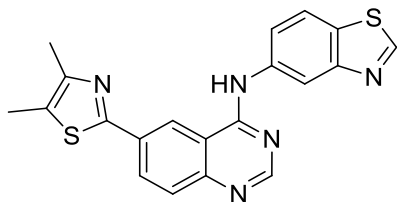

Purified by column chromatography (EtOAc). Yellow solid, 85 % yield. ^{1}H NMR (401 MHz, DMSO-d_6) δ 10.35 (s, 1H), 9.43 (s, 1H), 9.02 (d, *J* = 1.7 Hz, 1H), 8.68 (d, *J* = 1.9 Hz, 1H), 8.64 (s, 1H), 8.33 (dd, *J* = 8.7, 1.8 Hz, 1H), 8.18 (d, *J* = 8.7 Hz, 1H), 7.95 (dd, *J* = 8.7, 2.0 Hz, 1H), 7.86 (d, *J* = 8.7 Hz, 1H), 2.45 (d, *J* = 0.9 Hz, 4H), 2.39 (d, *J* = 0.9 Hz, 3H). ^{13}C NMR (101 MHz, DMSO-d_6) δ 161.67, 158.56, 157.39, 155.50, 153.98, 150.89, 149.91, 138.05, 131.69, 130.87, 129.27, 129.23, 128.28, 122.38, 122.00, 120.48, 117.12, 115.93, 15.11, 11.61. LC-MS m/z: 389.8 (M+H)$^+$. Rt = 3.6 minutes. HRMS calcd for $C_{20}H_{16}N_5S_2$ m/z: 390.08416 (M+H)$^+$, found 390.08430. Na-HRMS calcd for $C_{20}H_{15}N_5NaS_2$ m/z: 412.06611 (M+Na)$^+$, found 412.06634.

N-(6-(3-Methylthiophen-2-yl)quinazolin-4-yl)benzo[*d*]thiazol-5-amine (91m)
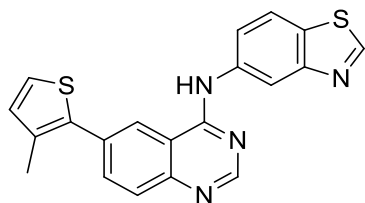
Purified by column chromatography (EtOAc/DCM/EtOH, 6:3:0.5). White solid, 90 % yield. ^{1}H NMR (401 MHz, DMSO-d_6) δ 10.11 (s, 1H), 9.42 (s, 1H), 8.72 (d, *J* = 1.9 Hz, 1H), 8.68 (d, *J* = 1.6 Hz, 1H), 8.67 (s, 1H), 8.17 (d, *J* = 8.7 Hz, 1H), 7.96 (dd, *J* = 8.6, 1.8 Hz, 1H), 7.95 (dd, *J* = 8.6, 2.1 Hz, 2H), 7.88 (d, *J* = 8.6 Hz, 1H), 7.59 (d, *J* = 5.1 Hz, 1H), 7.10 (d, *J* = 5.1 Hz, 1H), 2.37 (s, 3H). ^{13}C NMR (101 MHz, DMSO-d_6) δ 158.26, 157.38, 155.09, 154.00, 149.33, 138.18, 136.50, 134.54, 134.29, 132.79, 131.85, 129.10, 128.74, 125.47, 123.14, 122.41, 121.73, 116.80, 115.75, 15.09. LC-MS m/z: 375.0 (M+H)$^+$. Rt = 3.5 minutes. HRMS calcd for $C_{20}H_{15}N_4S_2$ m/z: 375.07326 (M+H)$^+$, found 375.07342. Na-HRMS calcd for $C_{20}H_{14}N_4NaS_2$ m/z: 397.05521 (M+Na)$^+$, found 397.05535.

Suzuki coupling leading to 92an, 92ao, 92ap, 92cn and 92mn

To a starting material (**90a**, **90c** and **90m**, 0.16 mmol) were added sequentially a boronic acid or a boronate ester substrate (4 eq), K_3PO_4 (5 eq), Pd$_2$(dba)$_3$ (4 mol%) and SPhos (12 mol%).

The solid mixture was purged with argon and suspended in 1,4-dioxane (2 ml) and distilled H$_2$O (0.8 ml). The suspension was heated with stirring at 95 °C for 24 h. The mixture was cooled to room temperature, diluted with EtOAc and filtered to remove solid impurities. The solvent was removed under reduced pressure, purifying the residue as described below.

(3-(4-(Benzo[*d*]thiazol-5-ylamino)-6-(thiophen-2-yl)quinazolin-7-yl)phenyl)methanol (92an)
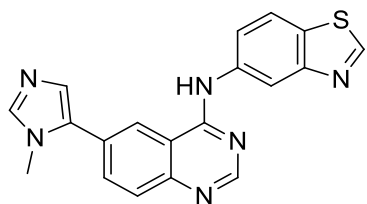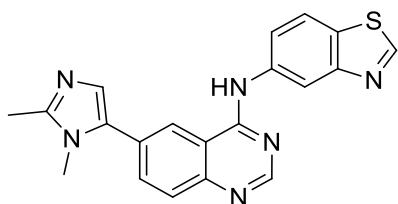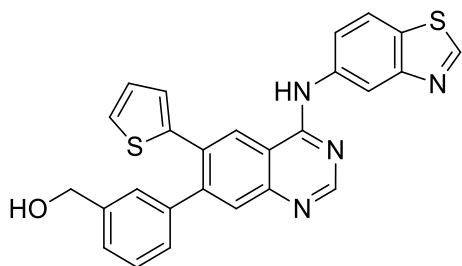

Purified by column chromatography (EtOAc/toluene/EtOH, 6:3:0.5), followed by recrystallization from EtOAc. Yellow solid, 70 % yield. ^{1}H NMR (401 MHz, DMSO-d_6) δ 10.20 (s, 1H), 9.43 (s, 1H), 8.82 (s, 1H), 8.75 (d, J = 1.9 Hz, 1H), 8.69 (s, 1H), 8.18 (d, J = 8.7 Hz, 1H), 7.97 (dd, J = 8.7, 2.0 Hz, 1H), 7.72 (s, 1H), 7.55 (dd, J = 5.0, 1.3 Hz, 1H), 7.37 – 7.27 (m, 3H), 7.14 (dt, J = 6.8, 1.9 Hz, 1H), 7.10 – 7.03 (m, 2H), 5.23 (t, J = 5.7 Hz, 1H), 4.52 (d, J = 5.7 Hz, 2H). ^{13}C NMR (101 MHz, DMSO-d_6) δ 158.08, 157.43, 155.65, 154.01, 149.55, 145.97, 143.19, 141.91, 139.92, 138.17, 132.07, 129.43, 129.09, 128.36, 128.35, 128.12, 127.86, 127.70, 127.57, 126.33, 125.11, 122.44, 121.59, 116.67, 114.92, 63.14. LC-MS m/z: 466.8 (M+H)$^+$. Rt = 3.6 minutes. HRMS calcd for C$_{26}$H$_{19}$ON$_4$S$_2$ m/z: 467.09948 (M+H)$^+$, found 467.09942. Na-HRMS calcd for C$_{26}$H$_{18}$ON$_4$NaS$_2$ m/z: 489.08142 (M+Na)$^+$, found 489.08137.

(5-(4-(Benzo[*d*]thiazol-5-ylamino)-6-(thiophen-2-yl)quinazolin-7-yl)furan-2-yl)methanol (92ao)
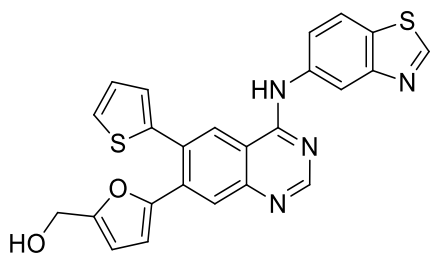
Purified by column chromatography (DCM/EtOAc/EtOH, 7:1:0.5), followed by recrystallization from MeOH/Et$_2$O. Yellow solid, 45 % yield. ^{1}H NMR (400 MHz, DMSO-

d$_6$) δ 10.11 (s, 1H), 9.41 (s, 1H), 8.76 – 8.72 (m, 2H), 8.70 (s, 1H), 8.15 (d, *J* = 8.7 Hz, 1H), 8.12 (s, 1H), 7.95 (dd, *J* = 8.8, 2.1 Hz, 1H), 7.75 (dd, *J* = 4.2, 2.3 Hz, 1H), 7.26 – 7.21 (m, 2H), 6.33 (d, *J* = 3.4 Hz, 1H), 5.80 (d, *J* = 3.4 Hz, 1H), 5.36 (t, *J* = 5.8 Hz, 1H), 4.45 (d, *J* = 5.7 Hz, 2H). ^{13}C NMR (101 MHz, DMSO-*d*$_6$) δ 157.94, 157.39, 156.88, 156.08, 153.98, 150.13, 149.74, 141.37, 138.12, 134.76, 129.64, 129.04, 128.31, 127.97, 127.67, 127.01, 124.84, 122.39, 121.44, 116.55, 114.10, 112.34, 109.63, 56.18. LC-MS m/z: 457.2 (M+H)$^+$. Rt = 4.3 minutes. HRMS calcd for C$_{24}$H$_{17}$O$_2$N$_4$S$_2$ m/z: 457.07874 (M+H)$^+$, found 457.07852. Na-HRMS calcd for C$_{24}$H$_{16}$O$_2$N$_4$NaS$_2$ m/z: 479.06069 (M+Na)$^+$, found 479.06048.

N-(7-(2,5-Dihydrofuran-3-yl)-6-(thiophen-2-yl)quinazolin-4-yl)benzo[*d*]thiazol-5-amine (92ap)
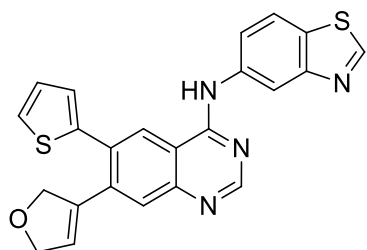
Purified by column chromatography (DCM/EtOAc/EtOH, 8:2:0.5), followed by recrystallization from MeOH/Et$_2$O. White solid, 76 % yield. ^{1}H NMR (400 MHz, DMSO-*d*$_6$) δ 10.12 (s, 1H), 9.41 (s, 1H), 8.73 (d, *J* = 2.0 Hz, 1H), 8.71 (s, 1H), 8.68 (s, 1H), 8.15 (d, *J* = 8.7 Hz, 1H), 7.95 (dd, *J* = 8.7, 2.1 Hz, 1H), 7.75 – 7.72 (m, 2H), 7.31 (dd, *J* = 3.5, 1.3 Hz, 1H), 7.23 (dd, *J* = 5.1, 3.4 Hz, 1H), 6.03 (p, *J* = 2.0 Hz, 1H), 4.67 (td, *J* = 4.9, 1.9 Hz, 2H), 4.55 (td, *J* = 4.9, 2.1 Hz, 2H). ^{13}C NMR (101 MHz, DMSO-*d*$_6$) δ 157.97, 157.41, 155.75, 153.98, 149.68, 141.49, 138.29, 138.10, 138.05, 131.66, 129.07, 128.26, 128.08, 128.02, 127.98, 127.94, 125.62, 122.41, 121.45, 116.56, 114.81, 76.38, 76.14. LC-MS m/z: 429.2 (M+H)$^+$. Rt = 3.7 minutes. HRMS calcd for C$_{23}$H$_{17}$ON$_4$S$_2$ m/z: 429.08383 (M+H)$^+$, found 429.08360.

(3-(4-(Benzo[*d*]thiazol-5-ylamino)-6-(1-methyl-1*H*-pyrrol-2-yl)quinazolin-7-yl)phenyl)methanol (92cn)
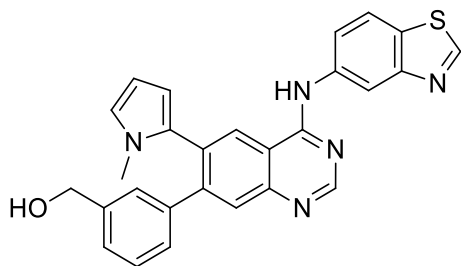
Purified by column chromatography (DCM/EtOAc/EtOH, 4.5:4:0.5), followed by recrystallization from MeOH. Yellow solid, 60 % yield. ^{1}H NMR (401 MHz, DMSO-d_6) δ 10.12 (s, 1H), 9.42 (s, 1H), 8.80 (d, J = 1.9 Hz, 1H), 8.72 (s, 1H), 8.71 (s, 1H), 8.16 (d, J = 8.7 Hz, 1H), 7.99 (dd, J = 8.7, 1.9 Hz, 1H), 7.84 (s, 1H), 7.32 – 7.24 (m, 3H), 7.07 (d, J = 7.5 Hz, 1H), 6.73 – 6.70 (m, 1H), 6.13 (dd, J = 3.5, 1.8 Hz, 1H), 6.09 (dd, J = 3.5, 2.7 Hz, 1H), 5.19 (t, J = 5.7 Hz, 1H), 4.48 (d, J = 5.6 Hz, 2H), 3.03 (s, 3H). ^{13}C NMR (101 MHz, DMSO-d_6) δ 158.03, 155.52, 154.00, 149.96, 148.02, 146.51, 143.19, 139.95, 138.29, 132.00, 130.74, 128.91, 128.65, 128.36, 127.31, 127.28, 126.73, 126.17, 123.10, 122.40, 121.36, 116.38, 114.59, 110.72, 107.84, 63.24, 34.24. LC-MS m/z: 464.3 (M+H)$^+$. Rt = 3.5 minutes. HRMS calcd for $C_{27}H_{22}ON_5S$ m/z: 464.15396 (M+H)$^+$, found 464.15391. Na-HRMS calcd for $C_{27}H_{21}ON_5NaS$ m/z: 486.13590 (M+Na)$^+$, found 486.13596.

(3-(4-(Benzo[*d*]thiazol-5-ylamino)-6-(3-methylthiophen-2-yl)quinazolin-7-yl)phenyl)methanol (92mn)
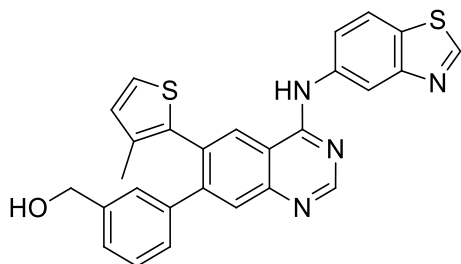
Purified by column chromatography (EtOAc/toluene/EtOH, 6:3:0.5), followed by recrystallization from EtOAc/Et$_2$O. White solid, 68 % yield. ^{1}H NMR (401 MHz, DMSO-d_6) δ 10.15 (s, 1H), 9.42 (s, 1H), 8.77 (d, J = 1.9 Hz, 1H), 8.76 (s, 1H), 8.72 (s, 1H), 8.16 (d, J = 8.7 Hz, 1H), 7.98 (dd, J = 8.7, 1.9 Hz, 1H), 7.81 (s, 1H), 7.48 (d, J = 5.1 Hz, 1H), 7.34 – 7.23 (m, 3H), 7.08 (dt, J = 7.0, 1.6 Hz, 1H), 6.87 (d, J = 5.1 Hz, 1H), 5.20 (t, J = 5.7 Hz, 1H), 4.48 (d, J = 5.6 Hz, 2H), 1.79 (s, 3H). ^{13}C NMR (101 MHz, DMSO-d_6) δ 158.04, 157.38, 155.76,

154.00, 150.02, 147.22, 143.02, 139.82, 138.20, 135.80, 135.29, 131.48, 130.22, 129.01, 128.95, 128.20, 127.53, 127.43, 126.94, 126.08, 125.67, 122.39, 121.47, 116.55, 114.56, 63.16, 14.54. LC-MS m/z: 480.9 (M+H)$^+$. Rt = 3.5 minutes. HRMS calcd for $C_{27}H_{21}ON_4S_2$ m/z: 481.11513 (M+H)$^+$, found 481.11518.

N-(7-Chloro-6-iodoquinazolin-4-yl)benzo[*d*]thiazol-5-amine (93)
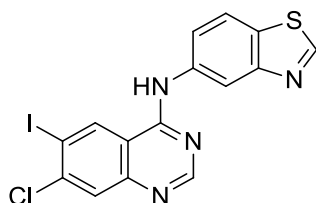
Intermediate **88** (375 mg, 1.12 mmol) and 5-aminobenzothiazole (186 mg, 1.24 mmol, 1.1 eq) were suspended in AcOH (4.7 ml) and heated at 95 °C with stirring for 1 h. The mixture was cooled to room temperature, leading to a precipitation of a solid. The slurry was diluted with H_2O (13 ml) and the solid was collected on a sintered funnel. Purification by column chromatography (EtOAc/toluene, 1:1), followed by recrystallization of the residue from MeOH, afforded **93** (450 mg, 91 % yield) as a white solid. ^{1}H NMR (401 MHz, DMSO-d_6) δ 10.17 (s, 1H), 9.42 (s, 1H), 9.26 (s, 1H), 8.70 (d, *J* = 1.9 Hz, 1H), 8.66 (s, 1H), 8.17 (d, *J* = 8.7 Hz, 1H), 7.98 (s, 1H), 7.92 (dd, *J* = 8.7, 1.9 Hz, 1H). 13C NMR (101 MHz, DMSO-d_6) δ 157.51, 156.94, 156.34, 153.95, 150.61, 141.97, 137.77, 135.33, 129.35, 127.79, 122.49, 121.46, 116.69, 115.82, 96.57. LC-MS m/z: 438.7 (M+H)$^+$. Rt = 4.0 minutes.

Suzuki coupling leading to 94a–94d

Intermediate **93** (0.41 mmol) was suspended in 1,4-dioxane (16 ml) and H_2O (5.5 ml). The suspension was treated with a boronic acid or a boronate ester substrate (1.5 eq), K_2CO_3 (2 eq) and Pd(dppf)Cl$_2$ · DCM (10 mol%). The resulting suspension was purged with argon and heated with stirring at 95 °C for 20 h. The mixture cooled to room temperature, diluted with EtOAc and filtered to remove solid impurities. The solvent was evaporated under reduced pressure, purifying the residue as described below.

N-(7-Chloro-6-(1*H*-pyrazol-3-yl)quinazolin-4-yl)benzo[*d*]thiazol-5-amine (94a)
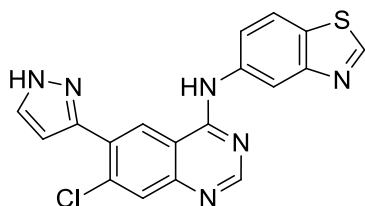
Purified by column chromatography (EtOAc/EtOH, 9.6:0.4). White solid, 70 % yield. ^{1}H NMR (401 MHz, DMSO-d_6) δ 13.25 (s, 1H), 10.31 (s, 1H), 9.42 (s, 1H), 8.96 (s, 1H), 8.71 (d, J = 1.7 Hz, 1H), 8.66 (s, 1H), 8.16 (d, J = 8.7 Hz, 1H), 7.98 – 7.90 (m, 3H), 6.80 (t, J = 1.9 Hz, 1H). ^{13}C NMR (101 MHz, DMSO-d_6) δ 158.27, 157.77, 156.02, 153.96, 150.00, 147.87, 138.03, 136.92, 131.79, 129.78, 129.19, 128.57, 125.83, 122.39, 121.67, 116.81, 114.67, 106.47. LC-MS m/z: 379.1 (M+H)$^+$. Rt = 3.3 minutes. HRMS calcd for $C_{18}H_{12}N_6ClS$ m/z: 379.05272 (M+H)$^+$, found 379.05293.

N-(7-Chloro-6-(6-methoxypyridin-2-yl)quinazolin-4-yl)benzo[d]thiazol-5-amine (94b)
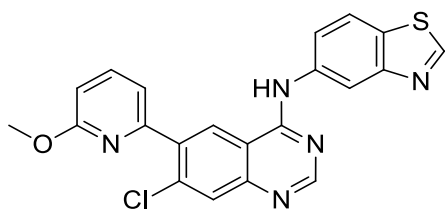
Purified by column chromatography (EtOAc/toluene/DCM, 5:5:1). White solid, 80 % yield. ^{1}H NMR (401 MHz, DMSO-d_6) δ 10.21 (s, 1H), 9.42 (s, 1H), 8.87 (s, 1H), 8.71 (d, J = 2.7 Hz, 2H), 8.17 (d, J = 8.7 Hz, 1H), 8.00 (s, 1H), 7.95 – 7.89 (m, 2H), 7.37 (dd, J = 7.3, 0.6 Hz, 1H), 6.95 (dd, J = 8.3, 0.6 Hz, 1H), 3.94 (s, 3H). ^{13}C NMR (101 MHz, DMSO-d_6) δ 163.49, 158.33, 157.50, 156.50, 153.97, 153.83, 150.55, 140.10, 137.87, 137.27, 136.77, 129.31, 128.61, 126.76, 122.49, 121.59, 118.34, 116.79, 114.45, 110.45, 53.85. LC-MS m/z: 420.2 (M+H)$^+$. Rt = 3.9 minutes. HRMS calcd for $C_{21}H_{15}ON_5ClS$ m/z: 420.06803 (M+H)$^+$, found 420.06844. Na-HRMS calcd for $C_{21}H_{14}ON_5ClNaS$ m/z: 442.04998 (M+Na)$^+$, found. 442.05040.

N-(7-Chloro-6-phenylquinazolin-4-yl)benzo[d]thiazol-5-amine (94c)

Purified by column chromatography (EtOAc/toluene, 6:4). White solid, 65 % yield. ^{1}H NMR (401 MHz, DMSO-d_6) δ 10.15 (s, 1H), 9.42 (s, 1H), 8.73 (s, 1H), 8.72 (d, J = 2.0 Hz, 1H), 8.69 (s, 1H), 8.16 (d, J = 8.7 Hz, 1H), 8.00 (s, 1H), 7.93 (dd, J = 8.7, 2.0 Hz, 1H), 7.61 – 7.55 (m, 4H), 7.53 – 7.49 (m, 1H). ^{13}C NMR (101 MHz, DMSO-d_6) δ 158.17, 157.48, 156.15, 153.97, 150.14, 138.71, 138.55, 137.94, 137.02, 130.20, 129.20, 128.76, 128.62, 128.31,

126.36, 122.46, 121.45, 116.61, 114.62. LC-MS m/z: 389.2 (M+H)⁺. Rt = 4.0 minutes. HRMS calcd for $C_{21}H_{14}N_4ClS$ m/z: 389.06222 (M+H)⁺, found 389.06260.

N-(7-Chloro-6-(4-methylthiophen-3-yl)quinazolin-4-yl)benzo[*d*]thiazol-5-amine (94d)

Purified by column chromatography (EtOAc/toluene, 6:3). White solid, 83 % yield. ¹H NMR (401 MHz, DMSO-d_6) δ 10.12 (s, 1H), 9.42 (s, 1H), 8.73 (d, *J* = 1.8 Hz, 2H), 8.70 (s, 2H), 8.69 (s, 2H), 8.15 (d, *J* = 8.7 Hz, 1H), 8.00 (s, 1H), 7.93 (dd, *J* = 8.9, 1.9 Hz, 1H), 7.61 (d, *J* = 3.2 Hz, 1H), 7.38 (dd, *J* = 2.9, 1.0 Hz, 1H), 2.11 (d, *J* = 1.0 Hz, 3H). ¹³C NMR (101 MHz, DMSO-d_6) δ 159.90, 158.08, 156.19, 153.95, 150.39, 139.59, 138.26, 137.93, 137.19, 134.31, 129.19, 127.91, 126.76, 125.98, 122.49, 122.45, 121.42, 116.59, 114.36, 14.95. LC-MS m/z: 409.2 (M+H)⁺. Rt = 4.1 minutes. HRMS calcd for $C_{20}H_{14}N_4ClS_2$ m/z: 409.03429 (M+H)⁺, found 409.03467.

Pd-catalyzed reductive hydrodechlorination leading to 95a–95d

The same methodology (reagents and conditions) that was previously described for the synthesis of compounds **91a–91i, 91k and 91m**, was applied to convert compounds **94a–94d** into the products. The products were purified as described below.

N-(6-(1*H*-Pyrazol-3-yl)quinazolin-4-yl)benzo[*d*]thiazol-5-amine (95a)
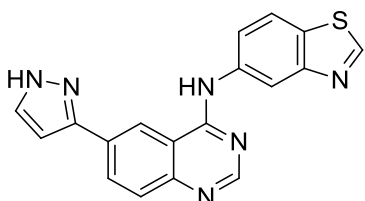
Purified by column chromatography (EtOAc/DCM/EtOH, 9:0.6:0.4), followed by recrystallization from MeOH. White solid, 80 % yield. ¹H NMR (401 MHz, DMSO-d_6) δ 13.09 (s, 1H), 10.14 (s, 1H), 9.43 (s, 1H), 8.98 (s, 1H), 8.73 (d, *J* = 2.0 Hz, 1H), 8.63 (s, 1H), 8.39 (d, *J* = 8.7 Hz, 1H), 8.18 (d, *J* = 8.7 Hz, 1H), 7.98 (dd, *J* = 8.7, 2.1 Hz, 1H), 7.91 (s, 1H), 7.85 (d, *J* = 8.7 Hz, 1H), 6.99 – 6.94 (m, 1H). ¹³C NMR (101 MHz, DMSO-d_6) δ 158.34, 157.39, 154.56, 154.03, 150.01, 149.65, 138.28, 132.54, 130.99, 130.72, 129.00, 128.66,

122.40, 121.75, 119.12, 116.75, 115.91, 102.94. LC-MS m/z: 345.1 (M+H)$^+$. Rt = 3.0 minutes. C$_{18}$H$_{13}$N$_6$S m/z: 345.09169 (M+H)$^+$, found 345.09184. Na-HRMS calcd for C$_{18}$H$_{12}$N$_6$NaS m/z: 367.07364 (M+Na)$^+$, found 367.07375.

N-(6-(6-Methoxypyridin-2-yl)quinazolin-4-yl)benzo[*d*]thiazol-5-amine (95b)
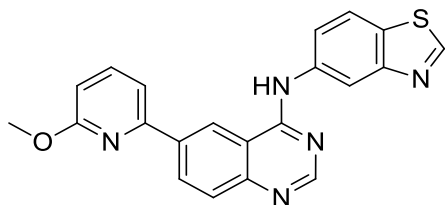
Purified by column chromatography (EtOAc/toluene, 6:3). White solid, 86 % yield. ^{1}H NMR (401 MHz, DMSO-*d*$_6$) δ 10.22 (s, 1H), 9.44 (s, 1H), 9.22 (d, *J* = 1.9 Hz, 1H), 8.72 (d, *J* = 1.9 Hz, 1H), 8.71 – 8.63 (m, 2H), 8.20 (d, *J* = 8.7 Hz, 1H), 8.01 – 7.84 (m, 4H), 6.88 (d, *J* = 8.1 Hz, 1H), 4.05 (s, 3H). ^{13}C NMR (101 MHz, DMSO-*d*$_6$) δ 163.86, 159.13, 158.65, 155.41, 154.04, 153.40, 150.65, 140.62, 138.11, 136.79, 131.74, 129.22, 128.74, 122.51, 121.83, 121.22, 116.93, 115.66, 114.21, 110.23, 53.60. LC-MS m/z: 386.2 (M+H)$^+$. Rt = 3.5 minutes. HRMS calcd for C$_{21}$H$_{16}$ON$_5$S m/z: 386.10701 (M+H)$^+$, found 386.10714. Na-HRMS calcd for C$_{21}$H$_{15}$ON$_5$NaS m/z: 408.08895 (M+Na)$^+$, found 408.08903.

N-(6-Phenylquinazolin-4-yl)benzo[*d*]thiazol-5-amine (95c)
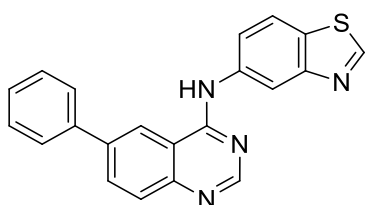
Purified by column chromatography (EtOAc/toluene/DCM, 6:4:1), followed by recrystallization from EtOAc. White solid, 83 % yield. ^{1}H NMR (401 MHz, DMSO-*d*$_6$) δ 10.15 (s, 1H), 9.43 (s, 1H), 8.91 (d, *J* = 1.8 Hz, 1H), 8.73 (d, *J* = 1.9 Hz, 1H), 8.67 (s, 1H), 8.23 (dd, *J* = 8.7, 2.0 Hz, 1H), 8.19 (d, *J* = 8.8 Hz, 1H), 7.97 (dd, *J* = 8.7, 1.9 Hz, 1H), 7.95 – 7.89 (m, 3H), 7.61 – 7.56 (m, 2H), 7.50 – 7.44 (m, 1H). ^{13}C NMR (101 MHz, DMSO-*d*$_6$) δ 158.41, 157.44, 154.95, 154.03, 149.59, 139.66, 138.64, 138.20, 132.34, 129.54, 129.07, 128.95, 128.45, 127.68, 122.45, 121.68, 120.97, 116.74, 115.91. LC-MS m/z: 355.2 (M+H)$^+$. Rt = 3.5 minutes. HRMS calcd for C$_{21}$H$_{15}$N$_4$S m/z: 355.10119 (M+H)$^+$, found 355.10133.

N-(6-(4-Methylthiophen-3-yl)quinazolin-4-yl)benzo[d]thiazol-5-amine (95d)

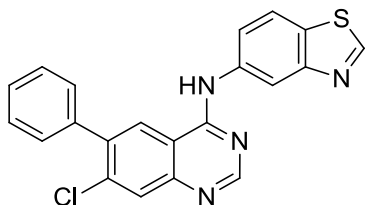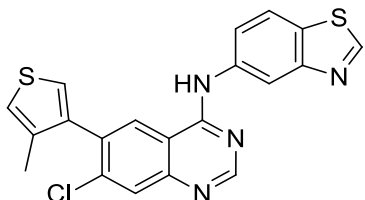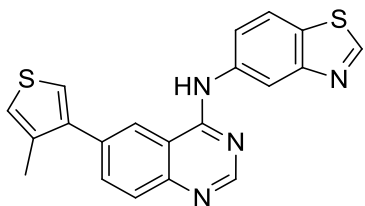Purified by column chromatography (EtOAc/toluene, 6:3). White solid, 78 % yield. ^{1}H NMR (401 MHz, DMSO-d_6) δ 10.03 (s, 1H), 9.42 (s, 1H), 8.75 (d, J = 1.9 Hz, 1H), 8.68 (s, 1H), 8.67 (d, J = 1.6 Hz, 1H), 8.17 (d, J = 8.7 Hz, 1H), 7.96 (ddd, J = 8.4, 6.2, 1.9 Hz, 2H), 7.87 (d, J = 8.6 Hz, 1H), 7.67 (d, J = 3.1 Hz, 1H), 7.39 (dd, J = 3.3, 1.1 Hz, 1H), 2.33 (d, J = 1.0 Hz, 3H). ^{13}C NMR (101 MHz, DMSO-d_6) δ 158.24, 157.39, 154.87, 154.01, 149.21, 142.16, 138.26, 136.19, 135.22, 134.08, 128.95, 128.34, 125.10, 123.48, 122.73, 122.42, 121.51, 116.53, 115.62, 15.74. LC-MS m/z: 375.2 (M+H)$^+$. Rt = 3.5 minutes. HRMS calcd for $C_{20}H_{15}N_4S_2$ m/z: 375.07326 (M+H)$^+$, found 375.07339.

5.2. Molecular docking analyses

5.2.1. Schrödinger Maestro

Known structures of enzyme/ligand complexes (RIPK2, PDB: 6RNA[139] and RIPK3, PDB: 7MX3[154]) were uploaded into the Maestro software (Schrödinger LLC, version 12.9.123, release 2021-3)[166], using the Protein Preparation Wizard to assign bond orders, add all hydrogens and remove of all water molecules. The OPLS3e force field was employed to restrain energy minimization. LigPrep module was utilized for the preparation of the new ligands to analyze, adjusting bond distances and orders as well as the ionization of compounds to pH 7±1. Considering that the compounds prepared could likely bind to the ATP-binding pocket of RIPK2 and RIPK3, appropriate docking grids were generated defining the kinase domains of the proteins. The Schrödinger Grid-based Ligand Docking with Energetics (GLIDE) Suite 2021 application module served for the docking analyses of the ligand in complex with the kinase domains of the enzyme targets. In the case of Glide, twenty poses per ligand were set. The Glide redocking was conducted setting the extra precision parameters.

5.2.2. Autodock Vina

As aforementioned, but employing Autodock Vina 1.1[167], docking simulations were performed with the pre-treated RIPK2 and RIPK3 structures (PDB: 6RNA and PDB: 7MX3, respectively). The chain A of RIPK2 was employed during the docking determinations,

selecting a search space of 20 × 20 × 20 Å, which was centered at coordinates -39.1, 40.0, and -2.5 Å. Rotation and flexibility were set for the residue Ser25 of the enzyme RIPK2. In the case of RIPK3, the enzyme chain A served to conduct the docking analyses, using a search space of 20 × 20 × 20 Å, which was centered at coordinates 8.2, 19.5, and 25.3 Å. During the docking, comprehensiveness parameter was set at 200 to ensure accurate sampling.

5.3. RIPK1-4 production and expression

The enzymes RIPK1 (residues 1-321), RIPK2 (8-310), RIPK3 (1-307) and RIPK4 (1-340) were suitably cloned into a pACEBac1 vector (Geneva Biotech) bearing a N-terminal polyhistidine tag, which was followed by a tag for MBP affinity and a cleavage site for TEV protease. The sequences were expressed in Sf9 cells, according to manufacturer's instructions. Removal of tags and the isolations of the recombinant enzymes were performed as described earlier by others.[168]

5.4. RIPK1-4 biochemical assays

ADP-Glo^{TM} kinase reagent (Promega) analyses served to determine the ADP generated during the kinase reaction. Biochemical reactions were conducted in reaction buffer including, 20 mM trometamol, pH 7.2, 2.5 mM $MnCl_2$, 100 mM NaCl, 4 mM $MgCl_2$, 0.05 mM dithiothreitol, added to 105 nM RIPK1, 12 nM RIPK2, 70 nM RIPK3 or 50 nM RIPK4, 25 μM (or 50 μM for RIPK4) myelin basic protein and 5 μM ATP concentrations. The inhibitors were tested at selected concentrations. Pre-seeding of the compound was carried out onto 384-well white plates (Thermo Fisher Scientific) employing an ECHO® liquid handler from 10 mM of DMSO solutions as commercially marketed. Subsequently, myelin basic protein and the enzymes in a reaction buffer were incorporated employing a Mantis® liquid dispenser (Formulatrix®). After pre-incubation for 15 min at room temperature, the reactions were induced by adding ATP (ECHO®). The reactions were allowed to run for 90 min at room temperature. At this point, the reactions were quenched by adding 5 μL of ADP-Glo^{TM} Reagent and left on an orbital shaker for 40 min, serving to deplete the residual ATP. Subsequently, 10 μL of Kinase Detection Reagent were added and the suspension was left to stand on an orbital shaker for further 10 min to convert ADP into ATP. Quantification of the product was achieved by luciferase reaction. Luminescence was detected using a TECAN Spark multimode reader and, following background subtraction of the reactions not including ATP, it was plotted against the compound concentration. GraphPad Prism software tool v.8.0 was utilized to calculate the IC_{50} values through a non-linear regression model.

5.5. Cellular NOD/RIPK2/NF-κB reporter assays

NF-κB reporter monocytes (InvivoGen) were utilized to evaluate cellular responses to the RIPK2 inhibitors analyzed. The compounds were pre-seeded onto 384-well plates and coated by 20 μL of cell suspension (1×10^6 cells/mL in RPMI 1640 medium supplemented with 10% endotoxin-free fetal bovine serum). After 30 min of pre-incubation, 5 μL of meso-lanthionine tripeptide (C14-Tri-LAN-Gly as a NOD1 stimulant, 1 μg/mL), or muramyl dipeptide (MDP as a NOD2 stimulant, 10 μg/mL), were added to the monocytes to promote NOD-related signaling. In parallel experiments, LPS (1 μg/mL) were added to the cells to activate NF-κB signaling induced by other enzymatic cascades non-correlated to NOD stimulation. The monocytes were then set for 24 h at 37 °C in 5 % CO_2. At the end of the experiments, 5 μL of the cell medium were mixed with 20 μL of QUANTI-Luc™ Gold reagent, allowing luminescence to be detected by a TECAN Spark multimode reader. After luminescence of empty media was deducted, IC_{50} values of compounds were calculated through a non-linear regression model, utilizing the GraphPad Prism software tool v.8.0. Cytotoxicity exerted by the compounds at 10 μM was evaluated using the CellTiter-Glo® 2.0 (Promega) reagent. Equal volumes of the reagent and the cell suspension were mixed on an orbital shaker for 20 min, following which luminescence was finally measured.

5.6. Cellular RIPK3-mediated necroptosis assays

Human colon cancer HT-29 cells (ATCC HTB-38) were employed to assess the effects of the compounds against necroptosis. The HT-29 cells were set in the 384-well white plates at a concentration of 4,000 cells per well and subjected to a pre-incubation period of 24 h. The cells were subsequently mixed with variable concentrations of the compounds, 20 μM z-VAD-FMK, 100 nM BV-6 and 10 ng/mL TNF-α, which were added employing a ECHO-550® liquid handler. After an incubation period of 24 h in a 5 % CO_2 atmosphere at 37 °C, cell viability was measured by means of CellTiter-Glo® 2.0 detection reagent enabling ATP quantification. The reagent was incorporated to the medium in a 1:1 ratio. Subsequently, the plate was allowed to stand on an orbital shaker for 3 min at 350 rpm, at room temperature. A multimode plate reader was employed to measure luminescence. The signal of the cells treated only by vehicle corresponded to complete viability, whereas the signal of the necroptotic cells treated with zVAD-FMK/BV-6/TNF-α corresponded to nil viability.

5.7. Cytotoxicity assays in HT-29 cells and NF-κB reporter monocytes

To evaluate cytotoxicity of the molecules in HT-29 cells or THP1-Lucia™ NF-κB monocytes, the cells were pre-set in Dulbecco's modified eagle medium high glucose culture

containing 1 % GlutaMax and 10 % fetal bovine serum devoid of antibiotics. Subsequently, the cells were seeded in 384-well white plates (Thermo Fisher Scientific, Waltham, USA) at a concentration range of 4,000 – 20,000 cells per well for both HT-29 and THP-1 cells. After 24 h, selected concentrations of the compounds were added to the cells, which were then set at 37 °C under a 5 % CO_2 atmosphere for additional 24 h. At this stage, CellTiter-Glo® 2.0 detection reagent (Promega, Madison, USA) was incorporated to the cell medium and the plate was left on an orbital shaker at 350 rpm for 3 min, at room temperature. Final measurement of luminescence was conducted through a multimode plate reader. Interpretation of signals of the cells treated with the compounds was calibrated according to the values of the cells that were not treated, setting the latter as 100 % viability.

5.8. Metabolic stability assays in human and mouse liver microsomes and plasma

Microsomal stability assays were conducted incubating 0.5 mg/ml of human and mouse liver microsomal preparations (Thermo Fisher Scientific) and 10 µM of compound solutions in 90 mM trometamol hydrochloride buffer (pH 7.4), including 2 mM $MgCl_2$ and 2 mM NADPH, at 37 °C, over 45 min. The reactions were quenched by adding four volumes of ice-cold MeOH, mixing vigorously the suspension at −20 °C for 1 h. Centrifuging of the samples and analyses of the supernatant were performed through an ECHO-MS® System (Sciex, Framingham, MA, USA). Prior to the addition of microsomes, zero time points were generated by adding ice-cold MeOH to the mixture consisting only of cofactors and the compounds analyzed.

In the plasma stability assays, 5 µM of compound preparations were subjected to incubation with human and mouse plasma (Biowest) at 37 °C for 2 and 4 h. The reactions were quenched as previously described in the microsomal assays. Centrifuging of the samples and analyses of the supernatant were performed using the above-mentioned ECHO-MS®. Prior to the addition of plasma, starting time points were generated by adding ice-cold MeOH to the buffer containing only the compounds.

REFERENCES

(1)   Manning, G.; Whyte, D. B.; Martinez, R.; Hunter, T.; Sudarsanam, S. The Protein Kinase Complement of the Human Genome. *Science* **2002**, *298* (5600), 1912–1934. https://doi.org/10.1126/science.1075762.

(2)   Cheng, H.-C.; Qi, R. Z.; Paudel, H.; Zhu, H.-J. Regulation and Function of Protein Kinases and Phosphatases. *Enzyme Res* **2011**, *2011*, 1–3. https://doi.org/10.4061/2011/794089.

(3)   Ardito, F.; Giuliani, M.; Perrone, D.; Troiano, G.; Muzio, L. Lo. The Crucial Role of Protein Phosphorylation in Cell Signaling and Its Use as Targeted Therapy (Review). *Int J Mol Med* **2017**, *40* (2), 271–280. https://doi.org/10.3892/ijmm.2017.3036.

(4)   Eyers, P. A.; Murphy, J. M. The Evolving World of Pseudoenzymes: Proteins, Prejudice and Zombies. *BMC Biol* **2016**, *14* (1), 98. https://doi.org/10.1186/s12915-016-0322-x.

(5)   Shaw, A. S.; Kornev, A. P.; Hu, J.; Ahuja, L. G.; Taylor, S. S. Kinases and Pseudokinases: Lessons from RAF. *Mol Cell Biol* **2014**, *34* (9), 1538–1546. https://doi.org/10.1128/MCB.00057-14.

(6)   Fabbro, D.; Cowan-Jacob, S. W.; Moebitz, H. Ten Things You Should Know about Protein Kinases: IUPHAR Review 14. *Br J Pharmacol* **2015**, *172* (11), 2675–2700. https://doi.org/10.1111/bph.13096.

(7)   Bork, P.; Sander, C.; Valencia, A. Convergent Evolution of Similar Enzymatic Function on Different Protein Folds: The Hexokinase, Ribokinase, and Galactokinase Families of Sugar Kinases. *Protein Sci* **1993**, *2* (1), 31–40. https://doi.org/10.1002/pro.5560020104.

(8)   Aufderklamm, S.; Todenhöfer, T.; Gakis, G.; Kruck, S.; Hennenlotter, J.; Stenzl, A.; Schwentner, C. Thymidine Kinase and Cancer Monitoring. *Cancer Lett* **2012**, *316* (1), 6–10. https://doi.org/10.1016/j.canlet.2011.10.025.

(9)   Heath, C. M.; Stahl, P. D.; Barbieri, M. A. Lipid Kinases Play Crucial and Multiple Roles in Membrane Trafficking and Signaling. *Histol Histopathol* **2003**, *18* (3), 989–998. https://doi.org/10.14670/HH-18.989.

(10)   Duong-Ly, K. C.; Peterson, J. R. The Human Kinome and Kinase Inhibition. *Curr Protoc Pharmacol* **2013**, *60* (1). https://doi.org/10.1002/0471141755.ph0209s60.

(11)   Jeon, J. Y.; Sparreboom, A.; Baker, S. D. Kinase Inhibitors: The Reality Behind the Success. *Clin Pharmacol Ther* **2017**, *102* (5), 726–730. https://doi.org/10.1002/cpt.815.

(12)   Bhullar, K. S.; Lagarón, N. O.; McGowan, E. M.; Parmar, I.; Jha, A.; Hubbard, B. P.; Rupasinghe, H. P. V. Kinase-Targeted Cancer Therapies: Progress, Challenges and Future Directions. *Mol Cancer* **2018**, *17* (1), 48. https://doi.org/10.1186/s12943-018-0804-2.

(13)   Veber, D. F.; Johnson, S. R.; Cheng, H.-Y.; Smith, B. R.; Ward, K. W.; Kopple, K. D. Molecular Properties That Influence the Oral Bioavailability of Drug Candidates. *J Med Chem* **2002**, *45* (12), 2615–2623. https://doi.org/10.1021/jm020017n.

(14)   Hojjat-Farsangi, M. Small-Molecule Inhibitors of the Receptor Tyrosine Kinases: Promising Tools for Targeted Cancer Therapies. *Int J Mol Sci* **2014**, *15* (8), 13768–13801. https://doi.org/10.3390/ijms150813768.

(15)   Roskoski, R. Classification of Small Molecule Protein Kinase Inhibitors Based upon the Structures of Their Drug-Enzyme Complexes. *Pharmacol Res* **2016**, *103*, 26–48. https://doi.org/10.1016/j.phrs.2015.10.021.

(16)   Ayala-Aguilera, C. C.; Valero, T.; Lorente-Macías, Á.; Baillache, D. J.; Croke, S.; Unciti-Broceta, A. Small Molecule Kinase Inhibitor Drugs (1995–2021): Medical Indication, Pharmacology, and Synthesis. *J Med Chem* **2022**, *65* (2), 1047–1131. https://doi.org/10.1021/acs.jmedchem.1c00963.

(17)   Roskoski Jr., R. Properties of FDA-Approved Small Molecule Protein Kinase Inhibitors: A 2022 Update. *Pharmacol Res* **2022**, *175*, 106037. https://doi.org/10.1016/j.phrs.2021.106037.

(18)   Carles, F.; Bourg, S.; Meyer, C.; Bonnet, P. PKIDB: A Curated, Annotated and Updated Database of Protein Kinase Inhibitors in Clinical Trials. *Molecules* **2018**, *23* (4), 908. https://doi.org/10.3390/molecules23040908.

(19)   Zhang, M.; Liu, Y.; Jang, H.; Nussinov, R. Strategy toward Kinase-Selective Drug Discovery. *J Chem Theory Comput* **2023**, *19* (5), 1615–1628. https://doi.org/10.1021/acs.jctc.2c01171.

(20)   Zhang, J.; Yang, P. L.; Gray, N. S. Targeting Cancer with Small Molecule Kinase Inhibitors. *Nat Rev Cancer* **2009**, *9* (1), 28–39. https://doi.org/10.1038/nrc2559.

(21)   Noble, M. E. M.; Endicott, J. A.; Johnson, L. N. Protein Kinase Inhibitors: Insights into Drug Design from Structure. *Science* **2004**, *303* (5665), 1800–1805. https://doi.org/10.1126/science.1095920.

(22)   Maveyraud, L.; Mourey, L. Protein X-Ray Crystallography and Drug Discovery. *Molecules* **2020**, *25* (5), 1030. https://doi.org/10.3390/molecules25051030.

(23) Xiao, Y.; Liddle, J. C.; Pardi, A.; Ahn, N. G. Dynamics of Protein Kinases: Insights from Nuclear Magnetic Resonance. *Acc Chem Res* **2015**, *48* (4), 1106–1114. https://doi.org/10.1021/acs.accounts.5b00001.

(24) Scapin, G.; Potter, C. S.; Carragher, B. Cryo-EM for Small Molecules Discovery, Design, Understanding, and Application. *Cell Chem Biol* **2018**, *25* (11), 1318–1325. https://doi.org/10.1016/j.chembiol.2018.07.006.

(25) Gagic, Z.; Ruzic, D.; Djokovic, N.; Djikic, T.; Nikolic, K. *In Silico* Methods for Design of Kinase Inhibitors as Anticancer Drugs. *Front Chem* **2020**, *7*. https://doi.org/10.3389/fchem.2019.00873.

(26) Knighton, D. R.; Zheng, J.; Ten Eyck, L. F.; Ashford, V. A.; Xuong, N.-H.; Taylor, S. S.; Sowadski, J. M. Crystal Structure of the Catalytic Subunit of Cyclic Adenosine Monophosphate-Dependent Protein Kinase. *Science* **1991**, *253* (5018), 407–414. https://doi.org/10.1126/science.1862342.

(27) Arter, C.; Trask, L.; Ward, S.; Yeoh, S.; Bayliss, R. Structural Features of the Protein Kinase Domain and Targeted Binding by Small-Molecule Inhibitors. *J Biol Chem* **2022**, *298* (8), 102247. https://doi.org/10.1016/j.jbc.2022.102247.

(28) Huang, H.; Zhao, R.; Dickson, B. M.; Skeel, R. D.; Post, C. B. AC Helix as a Switch in the Conformational Transition of Src/CDK-like Kinase Domains. *J Phys Chem B* **2012**, *116* (15), 4465–4475. https://doi.org/10.1021/jp301628r.

(29) Zheng, J.; Trafny, E. A.; Knighton, D. R.; Xuong, N.; Taylor, S. S.; Ten Eyck, L. F.; Sowadski, J. M. 2.2 Å Refined Crystal Structure of the Catalytic Subunit of CAMP-Dependent Protein Kinase Complexed with MnATP and a Peptide Inhibitor. *Acta Crystallogr D Biol Crystallogr* **1993**, *49* (3), 362–365. https://doi.org/10.1107/S0907444993000423.

(30) Zuccotto, F.; Ardini, E.; Casale, E.; Angiolini, M. Through the "Gatekeeper Door": Exploiting the Active Kinase Conformation. *J Med Chem* **2010**, *53* (7), 2681–2694. https://doi.org/10.1021/jm901443h.

(31) Adams, J. A. Activation Loop Phosphorylation and Catalysis in Protein Kinases: Is There Functional Evidence for the Autoinhibitor Model? *Biochemistry* **2003**, *42* (3), 601–607. https://doi.org/10.1021/bi020617o.

(32) Steichen, J. M.; Kuchinskas, M.; Keshwani, M. M.; Yang, J.; Adams, J. A.; Taylor, S. S. Structural Basis for the Regulation of Protein Kinase A by Activation Loop

Phosphorylation. *J Biol Chem* **2012**, *287* (18), 14672–14680. https://doi.org/10.1074/jbc.M111.335091.

(33) Treiber, D. K.; Shah, N. P. Ins and Outs of Kinase DFG Motifs. *Chem Biol* **2013**, *20* (6), 745–746. https://doi.org/10.1016/j.chembiol.2013.06.001.

(34) Johnson, L. N.; Noble, M. E. M.; Owen, D. J. Active and Inactive Protein Kinases: Structural Basis for Regulation. *Cell* **1996**, *85* (2), 149–158. https://doi.org/10.1016/S0092-8674(00)81092-2.

(35) Vijayan, R. S. K.; He, P.; Modi, V.; Duong-Ly, K. C.; Ma, H.; Peterson, J. R.; Dunbrack, R. L.; Levy, R. M. Conformational Analysis of the DFG-Out Kinase Motif and Biochemical Profiling of Structurally Validated Type II Inhibitors. *J Med Chem* **2015**, *58* (1), 466–479. https://doi.org/10.1021/jm501603h.

(36) Zhao, Z.; Wu, H.; Wang, L.; Liu, Y.; Knapp, S.; Liu, Q.; Gray, N. S. Exploration of Type II Binding Mode: A Privileged Approach for Kinase Inhibitor Focused Drug Discovery? *ACS Chem Biol* **2014**, *9* (6), 1230–1241. https://doi.org/10.1021/cb500129t.

(37) Tokarski, J. S.; Newitt, J. A.; Chang, C. Y. J.; Cheng, J. D.; Wittekind, M.; Kiefer, S. E.; Kish, K.; Lee, F. Y. F.; Borzillerri, R.; Lombardo, L. J.; Xie, D.; Zhang, Y.; Klei, H. E. The Structure of Dasatinib (BMS-354825) Bound to Activated ABL Kinase Domain Elucidates Its Inhibitory Activity against Imatinib-Resistant ABL Mutants. *Cancer Res* **2006**, *66* (11), 5790–5797. https://doi.org/10.1158/0008-5472.CAN-05-4187.

(38) Nagar, B.; Hantschel, O.; Young, M. A.; Scheffzek, K.; Veach, D.; Bornmann, W.; Clarkson, B.; Superti-Furga, G.; Kuriyan, J. Structural Basis for the Autoinhibition of C-Abl Tyrosine Kinase. *Cell* **2003**, *112* (6), 859–871. https://doi.org/10.1016/S0092-8674(03)00194-6.

(39) Verkhivker, G. M. Making the Invisible Visible: Toward Structural Characterization of Allosteric States, Interaction Networks, and Allosteric Regulatory Mechanisms in Protein Kinases. *Curr Opin Struct Biol* **2021**, *71*, 71–78. https://doi.org/10.1016/j.sbi.2021.06.002.

(40) Calleja, V.; Alcor, D.; Laguerre, M.; Park, J.; Vojnovic, B.; Hemmings, B. A.; Downward, J.; Parker, P. J.; Larijani, B. Intramolecular and Intermolecular Interactions of Protein Kinase B Define Its Activation In Vivo. *PLoS Biol* **2007**, *5* (4), e95. https://doi.org/10.1371/journal.pbio.0050095.

(41)   Fang, Z.; Grütter, C.; Rauh, D. Strategies for the Selective Regulation of Kinases with Allosteric Modulators: Exploiting Exclusive Structural Features. *ACS Chem Biol* **2013**, *8* (1), 58–70. https://doi.org/10.1021/cb300663j.

(42)   Weisner, J.; Landel, I.; Reintjes, C.; Uhlenbrock, N.; Trajkovic-Arsic, M.; Dienstbier, N.; Hardick, J.; Ladigan, S.; Lindemann, M.; Smith, S.; Quambusch, L.; Scheinpflug, R.; Depta, L.; Gontla, R.; Unger, A.; Müller, H.; Baumann, M.; Schultz-Fademrecht, C.; Günther, G.; Maghnouj, A.; Müller, M. P.; Pohl, M.; Teschendorf, C.; Wolters, H.; Viebahn, R.; Tannapfel, A.; Uhl, W.; Hengstler, J. G.; Hahn, S. A.; Siveke, J. T.; Rauh, D. Preclinical Efficacy of Covalent-Allosteric AKT Inhibitor Borussertib in Combination with Trametinib in *KRAS* -Mutant Pancreatic and Colorectal Cancer. *Cancer Res* **2019**, *79* (9), 2367–2378. https://doi.org/10.1158/0008-5472.CAN-18-2861.

(43)   Martinez, R.; Defnet, A.; Shapiro, P. Avoiding or Co-Opting ATP Inhibition: Overview of Type III, IV, V, and VI Kinase Inhibitors. In *Next Generation Kinase Inhibitors*; Springer International Publishing: Cham, **2020**, 29–59. https://doi.org/10.1007/978-3-030-48283-1_3.

(44)   Yun, C.-H.; Boggon, T. J.; Li, Y.; Woo, M. S.; Greulich, H.; Meyerson, M.; Eck, M. J. Structures of Lung Cancer-Derived EGFR Mutants and Inhibitor Complexes: Mechanism of Activation and Insights into Differential Inhibitor Sensitivity. *Cancer Cell* **2007**, *11* (3), 217–227. https://doi.org/10.1016/j.ccr.2006.12.017.

(45)   Stamos, J.; Sliwkowski, M. X.; Eigenbrot, C. Structure of the Epidermal Growth Factor Receptor Kinase Domain Alone and in Complex with a 4-Anilinoquinazoline Inhibitor. *J Biol Chem* **2002**, *277* (48), 46265–46272. https://doi.org/10.1074/jbc.M207135200.

(46)   Liao, J. J.-L. Molecular Recognition of Protein Kinase Binding Pockets for Design of Potent and Selective Kinase Inhibitors. *J Med Chem* **2007**, *50* (3), 409–424. https://doi.org/10.1021/jm0608107.

(47)   Weisberg, E.; Manley, P. W.; Breitenstein, W.; Brüggen, J.; Cowan-Jacob, S. W.; Ray, A.; Huntly, B.; Fabbro, D.; Fendrich, G.; Hall-Meyers, E.; Kung, A. L.; Mestan, J.; Daley, G. Q.; Callahan, L.; Catley, L.; Cavazza, C.; Mohammed, A.; Neuberg, D.; Wright, R. D.; Gilliland, D. G.; Griffin, J. D. Characterization of AMN107, a Selective Inhibitor of Native and Mutant Bcr-Abl. *Cancer Cell* **2005**, *7* (2), 129–141. https://doi.org/10.1016/j.ccr.2005.01.007.

(48)   Okamoto, K.; Ikemori-Kawada, M.; Jestel, A.; von König, K.; Funahashi, Y.; Matsushima, T.; Tsuruoka, A.; Inoue, A.; Matsui, J. Distinct Binding Mode of Multikinase Inhibitor

Lenvatinib Revealed by Biochemical Characterization. *ACS Med Chem Lett* **2015**, *6* (1), 89–94. https://doi.org/10.1021/ml500394m.

(49) Blanc, J.; Geney, R.; Menet, C. Type II Kinase Inhibitors: An Opportunity in Cancer for Rational Design. *Anticancer Agents Med Chem* **2013**, *13* (5), 731–747. https://doi.org/10.2174/1871520611313050008.

(50) Gavrin, L. K.; Saiah, E. Approaches to Discover Non-ATP Site Kinase Inhibitors. *Med Chem Commun* **2013**, *4* (1), 41–51. https://doi.org/10.1039/C2MD20180A.

(51) Gonzalez-Del Pino, G. L.; Li, K.; Park, E.; Schmoker, A. M.; Ha, B. H.; Eck, M. J. Allosteric MEK Inhibitors Act on BRAF/MEK Complexes to Block MEK Activation. *Proc Natl Acad Sci U S A* **2021**, *118* (36), e2107207118. https://doi.org/10.1073/pnas.2107207118.

(52) Rice, K. D.; Aay, N.; Anand, N. K.; Blazey, C. M.; Bowles, O. J.; Bussenius, J.; Costanzo, S.; Curtis, J. K.; Defina, S. C.; Dubenko, L.; Engst, S.; Joshi, A. A.; Kennedy, A. R.; Kim, A. I.; Koltun, E. S.; Lougheed, J. C.; Manalo, J.-C. L.; Martini, J.-F.; Nuss, J. M.; Peto, C. J.; Tsang, T. H.; Yu, P.; Johnston, S. Novel Carboxamide-Based Allosteric MEK Inhibitors: Discovery and Optimization Efforts toward XL518 (GDC-0973). *ACS Med Chem Lett* **2012**, *3* (5), 416–421. https://doi.org/10.1021/ml300049d.

(53) Wylie, A. A.; Schoepfer, J.; Jahnke, W.; Cowan-Jacob, S. W.; Loo, A.; Furet, P.; Marzinzik, A. L.; Pelle, X.; Donovan, J.; Zhu, W.; Buonamici, S.; Hassan, A. Q.; Lombardo, F.; Iyer, V.; Palmer, M.; Berellini, G.; Dodd, S.; Thohan, S.; Bitter, H.; Branford, S.; Ross, D. M.; Hughes, T. P.; Petruzzelli, L.; Vanasse, K. G.; Warmuth, M.; Hofmann, F.; Keen, N. J.; Sellers, W. R. The Allosteric Inhibitor ABL001 Enables Dual Targeting of BCR–ABL1. *Nature* **2017**, *543* (7647), 733–737. https://doi.org/10.1038/nature21702.

(54) Zhang, J.; Adrián, F. J.; Jahnke, W.; Cowan-Jacob, S. W.; Li, A. G.; Iacob, R. E.; Sim, T.; Powers, J.; Dierks, C.; Sun, F.; Guo, G.-R.; Ding, Q.; Okram, B.; Choi, Y.; Wojciechowski, A.; Deng, X.; Liu, G.; Fendrich, G.; Strauss, A.; Vajpai, N.; Grzesiek, S.; Tuntland, T.; Liu, Y.; Bursulaya, B.; Azam, M.; Manley, P. W.; Engen, J. R.; Daley, G. Q.; Warmuth, M.; Gray, N. S. Targeting Bcr–Abl by Combining Allosteric with ATP-Binding-Site Inhibitors. *Nature* **2010**, *463* (7280), 501–506. https://doi.org/10.1038/nature08675.

(55) Adrián, F. J.; Ding, Q.; Sim, T.; Velentza, A.; Sloan, C.; Liu, Y.; Zhang, G.; Hur, W.; Ding, S.; Manley, P.; Mestan, J.; Fabbro, D.; Gray, N. S. Allosteric Inhibitors of Bcr-Abl–

Dependent Cell Proliferation. *Nat Chem Biol* **2006**, *2* (2), 95–102. https://doi.org/10.1038/nchembio760.

(56)   Lamba, V.; Ghosh, I. New Directions in Targeting Protein Kinases: Focusing Upon True Allosteric and Bivalent Inhibitors. *Curr Pharm Des* **2012**, *18* (20), 2936–2945. https://doi.org/10.2174/138161212800672813.

(57)   Johnson, T. K.; Soellner, M. B. Bivalent Inhibitors of C-Src Tyrosine Kinase That Bind a Regulatory Domain. *Bioconjug Chem* **2016**, *27* (7), 1745–1749. https://doi.org/10.1021/acs.bioconjchem.6b00243.

(58)   Lavogina, D.; Enkvist, E.; Uri, A. Bisubstrate Inhibitors of Protein Kinases: From Principle to Practical Applications. *Chem Med Chem* **2010**, *5* (1), 23–34. https://doi.org/10.1002/cmdc.200900252.

(59)   Gower, C. M.; Chang, M. E. K.; Maly, D. J. Bivalent Inhibitors of Protein Kinases. *Crit Rev Biochem Mol Biol* **2014**, *49* (2), 102–115. https://doi.org/10.3109/10409238.2013.875513.

(60)   Jackson, P. A.; Widen, J. C.; Harki, D. A.; Brummond, K. M. Covalent Modifiers: A Chemical Perspective on the Reactivity of α,β-Unsaturated Carbonyls with Thiols via Hetero-Michael Addition Reactions. *J Med Chem* **2017**, *60* (3), 839–885. https://doi.org/10.1021/acs.jmedchem.6b00788.

(61)   Solca, F.; Dahl, G.; Zoephel, A.; Bader, G.; Sanderson, M.; Klein, C.; Kraemer, O.; Himmelsbach, F.; Haaksma, E.; Adolf, G. R. Target Binding Properties and Cellular Activity of Afatinib (BIBW 2992), an Irreversible ErbB Family Blocker. *J Pharmacol Exp Ther* **2012**, *343* (2), 342–350. https://doi.org/10.1124/jpet.112.197756.

(62)   Bender, A. T.; Gardberg, A.; Pereira, A.; Johnson, T.; Wu, Y.; Grenningloh, R.; Head, J.; Morandi, F.; Haselmayer, P.; Liu-Bujalski, L. Ability of Bruton's Tyrosine Kinase Inhibitors to Sequester Y551 and Prevent Phosphorylation Determines Potency for Inhibition of Fc Receptor but Not B-Cell Receptor Signaling. *Mol Pharmacol* **2017**, *91* (3), 208–219. https://doi.org/10.1124/mol.116.107037.

(63)   Serafimova, I. M.; Pufall, M. A.; Krishnan, S.; Duda, K.; Cohen, M. S.; Maglathlin, R. L.; McFarland, J. M.; Miller, R. M.; Frödin, M.; Taunton, J. Reversible Targeting of Noncatalytic Cysteines with Chemically Tuned Electrophiles. *Nat Chem Biol* **2012**, *8* (5), 471–476. https://doi.org/10.1038/nchembio.925.

(64)   Bradshaw, J. M.; McFarland, J. M.; Paavilainen, V. O.; Bisconte, A.; Tam, D.; Phan, V. T.; Romanov, S.; Finkle, D.; Shu, J.; Patel, V.; Ton, T.; Li, X.; Loughhead, D. G.; Nunn,

P. A.; Karr, D. E.; Gerritsen, M. E.; Funk, J. O.; Owens, T. D.; Verner, E.; Brameld, K. A.; Hill, R. J.; Goldstein, D. M.; Taunton, J. Prolonged and Tunable Residence Time Using Reversible Covalent Kinase Inhibitors. *Nat Chem Biol* **2015**, *11* (7), 525–531. https://doi.org/10.1038/nchembio.1817.

(65) Bradshaw, J.M., Brameld, K.A., Mrosek, M., Lammens, A., Blaesse, M., Crystal Structure of the Covalently Bonded Complex of Rilzabrutinib with BTK **2022**. https://doi.org/10.2210/pdb7L5P/pdb.

(66) Balla, A.; Tuymetova, G.; Barshishat, M.; Geiszt, M.; Balla, T. Characterization of Type II Phosphatidylinositol 4-Kinase Isoforms Reveals Association of the Enzymes with Endosomal Vesicular Compartments. *J Biol Chem* **2002**, *277* (22), 20041–20050. https://doi.org/10.1074/jbc.M111807200.

(67) Balla, A.; Balla, T. Phosphatidylinositol 4-Kinases: Old Enzymes with Emerging Functions. *Trends Cell Biol* **2006**, *16* (7), 351–361. https://doi.org/10.1016/j.tcb.2006.05.003.

(68) Brown, J. R.; Auger, K. R. Phylogenomics of Phosphoinositide Lipid Kinases: Perspectives on the Evolution of Second Messenger Signaling and Drug Discovery. *BMC Evol Biol* **2011**, *11* (1), 4. https://doi.org/10.1186/1471-2148-11-4.

(69) Burke, J. E.; Inglis, A. J.; Perisic, O.; Masson, G. R.; McLaughlin, S. H.; Rutaganira, F.; Shokat, K. M.; Williams, R. L. Structures of PI4KIIIβ Complexes Show Simultaneous Recruitment of Rab11 and Its Effectors. *Science* **2014**, *344* (6187), 1035–1038. https://doi.org/10.1126/science.1253397.

(70) Baumlova, A.; Chalupska, D.; Różycki, B.; Jovic, M.; Wisniewski, E.; Klima, M.; Dubankova, A.; Kloer, D. P.; Nencka, R.; Balla, T.; Boura, E. The Crystal Structure of the Phosphatidylinositol 4-kinase IIα. *EMBO Rep* **2014**, *15* (10), 1085–1092. https://doi.org/10.15252/embr.201438841.

(71) Klima, M.; Baumlova, A.; Chalupska, D.; Hřebabecký, H.; Dejmek, M.; Nencka, R.; Boura, E. The High-Resolution Crystal Structure of Phosphatidylinositol 4-Kinase IIβ and the Crystal Structure of Phosphatidylinositol 4-Kinase IIα Containing a Nucleoside Analogue Provide a Structural Basis for Isoform-Specific Inhibitor Design. *Acta Crystallogr D Biol Crystallogr* **2015**, *71* (7), 1555–1563. https://doi.org/10.1107/S1399004715009505.

(72)   Chu, K. M. E.; Minogue, S.; Hsuan, J. J.; Waugh, M. G. Differential Effects of the Phosphatidylinositol 4-Kinases, PI4KIIα and PI4KIIIβ, on Akt Activation and Apoptosis. *Cell Death Dis* **2010**, *1* (12), e106–e106. https://doi.org/10.1038/cddis.2010.84.

(73)   Tan, J.; Brill, J. A. Cinderella Story: PI4P Goes from Precursor to Key Signaling Molecule. *Crit Rev Biochem Mol Biol* **2014**, *49* (1), 33–58. https://doi.org/10.3109/10409238.2013.853024.

(74)   Hammond, G. R. V.; Burke, J. E. Novel Roles of Phosphoinositides in Signaling, Lipid Transport, and Disease. *Curr Opin Cell Biol* **2020**, *63*, 57–67. https://doi.org/10.1016/j.ceb.2019.12.007.

(75)   Clayton, E. L.; Minogue, S.; Waugh, M. G. Mammalian Phosphatidylinositol 4-Kinases as Modulators of Membrane Trafficking and Lipid Signaling Networks. *Prog Lipid Res* **2013**, *52* (3), 294–304. https://doi.org/10.1016/j.plipres.2013.04.002.

(76)   Minogue, S.; Waugh, M. G. The Phosphatidylinositol 4-Kinases: Don't Call It a Comeback. *Subcell Biochem*. **2012**, *58*, 1–24. doi:10.1007/978-94-007-3012-0_1.

(77)   Barylko, B.; Mao, Y. S.; Wlodarski, P.; Jung, G.; Binns, D. D.; Sun, H.-Q.; Yin, H. L.; Albanesi, J. P. Palmitoylation Controls the Catalytic Activity and Subcellular Distribution of Phosphatidylinositol 4-Kinase IIα. *J Biol Chem* **2009**, *284* (15), 9994–10003. https://doi.org/10.1074/jbc.M900724200.

(78)   Jung, G.; Wang, J.; Wlodarski, P.; Barylko, B.; Binns, D. D.; Shu, H.; Yin, H. L.; Albanesi, J. P. Molecular Determinants of Activation and Membrane Targeting of Phosphoinositol 4-Kinase IIβ. *Biochem J* **2008**, *409* (2), 501–509. https://doi.org/10.1042/BJ20070821.

(79)   Minogue, S.; Waugh, M. G.; De Matteis, M. A.; Stephens, D. J.; Berditchevski, F.; Hsuan, J. J. Phosphatidylinositol 4-Kinase Is Required for Endosomal Trafficking and Degradation of the EGF Receptor. *J Cell Sci* **2006**, *119* (3), 571–581. https://doi.org/10.1242/jcs.02752.

(80)   Pan, W.; Choi, S.-C.; Wang, H.; Qin, Y.; Volpicelli-Daley, L.; Swan, L.; Lucast, L.; Khoo, C.; Zhang, X.; Li, L.; Abrams, C. S.; Sokol, S. Y.; Wu, D. Wnt3a-Mediated Formation of Phosphatidylinositol 4,5-Bisphosphate Regulates LRP6 Phosphorylation. *Science* **2008**, *321* (5894), 1350–1353. https://doi.org/10.1126/science.1160741.

(81)   Li, J.; Lu, Y.; Zhang, J.; Kang, H.; Qin, Z.; Chen, C. PI4KIIα Is a Novel Regulator of Tumor Growth by Its Action on Angiogenesis and HIF-1α Regulation. *Oncogene* **2010**, *29* (17), 2550–2559. https://doi.org/10.1038/onc.2010.14.

(82)   Waugh, M. G. Phosphatidylinositol 4-Kinases, Phosphatidylinositol 4-Phosphate and Cancer. *Cancer Lett* **2012**, *325* (2), 125–131. https://doi.org/10.1016/j.canlet.2012.06.009.

(83)   Huang, X.; Cao, Y.; Bao, P.; Zhu, B.; Cheng, Z. High Expression of PI4K2A Predicted Poor Prognosis of Colon Adenocarcinoma (COAD) and Correlated with Immunity. *Cancer Med* **2023**, *12* (1), 837–851. https://doi.org/10.1002/cam4.4895.

(84)   Jović, M.; Kean, M. J.; Szentpetery, Z.; Polevoy, G.; Gingras, A.-C.; Brill, J. A.; Balla, T. Two Phosphatidylinositol 4-Kinases Control Lysosomal Delivery of the Gaucher Disease Enzyme, β-Glucocerebrosidase. *Mol Biol Cell* **2012**, *23* (8), 1533–1545. https://doi.org/10.1091/mbc.e11-06-0553.

(85)   Kang, M. S.; Baek, S.-H.; Chun, Y. S.; Moore, A. Z.; Landman, N.; Berman, D.; Yang, H. O.; Morishima-Kawashima, M.; Osawa, S.; Funamoto, S.; Ihara, Y.; Di Paolo, G.; Park, J. H.; Chung, S.; Kim, T.-W. Modulation of Lipid Kinase PI4KIIα Activity and Lipid Raft Association of Presenilin 1 Underlies γ-Secretase Inhibition by Ginsenoside (20S)-Rg3. *J Biol Chem* **2013**, *288* (29), 20868–20882. https://doi.org/10.1074/jbc.M112.445734.

(86)   Simons, J. P.; Al-Shawi, R.; Minogue, S.; Waugh, M. G.; Wiedemann, C.; Evangelou, S.; Loesch, A.; Sihra, T. S.; King, R.; Warner, T. T.; Hsuan, J. J. Loss of Phosphatidylinositol 4-Kinase 2α Activity Causes Late Onset Degeneration of Spinal Cord Axons. *Proc Natl Acad Sci U S A* **2009**, *106* (28), 11535–11539. https://doi.org/10.1073/pnas.0903011106.

(87)   Wieffer, M.; Cibrián Uhalte, E.; Posor, Y.; Otten, C.; Branz, K.; Schütz, I.; Mössinger, J.; Schu, P.; Abdelilah-Seyfried, S.; Krauß, M.; Haucke, V. PI4K2β/AP-1-Based TGN-Endosomal Sorting Regulates Wnt Signaling. *Curr Biol* **2013**, *23* (21), 2185–2190. https://doi.org/10.1016/j.cub.2013.09.017.

(88)   Alli-Balogun, G. O.; Gewinner, C. A.; Jacobs, R.; Kriston-Vizi, J.; Waugh, M. G.; Minogue, S. Phosphatidylinositol 4-Kinase IIβ Negatively Regulates Invadopodia Formation and Suppresses an Invasive Cellular Phenotype. *Mol Biol Cell* **2016**, *27* (25), 4033–4042. https://doi.org/10.1091/mbc.E16-08-0564.

(89)   Sobocińska, J.; Roszczenko-Jasińska, P.; Zaręba-Kozioł, M.; Hromada-Judycka, A.; Matveichuk, O. V.; Traczyk, G.; Łukasiuk, K.; Kwiatkowska, K. Lipopolysaccharide Upregulates Palmitoylated Enzymes of the Phosphatidylinositol Cycle: An Insight from Proteomic Studies. *Mol Cell Proteomics* **2018**, *17* (2), 233–254. https://doi.org/10.1074/mcp.RA117.000050.

(90)   Li, Y.; Mikrani, R.; Hu, Y.; Faran Ashraf Baig, M. M.; Abbas, M.; Akhtar, F.; Xu, M. Research Progress of Phosphatidylinositol 4-Kinase and Its Inhibitors in Inflammatory

Diseases. *Eur J Pharmacol* **2021**, *907*, 174300. https://doi.org/10.1016/j.ejphar.2021.174300.

(91) Boura, E.; Nencka, R. Phosphatidylinositol 4-Kinases: Function, Structure, and Inhibition. *Exp Cell Res* **2015**, *337* (2), 136–145. https://doi.org/10.1016/j.yexcr.2015.03.028.

(92) Sinha, R. K.; Patel, R. Y.; Bojjireddy, N.; Datta, A.; Subrahmanyam, G. Epigallocatechin Gallate (EGCG) Inhibits Type II Phosphatidylinositol 4-Kinases: A Key Component in Pathways of Phosphoinositide Turnover. *Arch Biochem Biophys* **2011**, *516* (1), 45–51. https://doi.org/10.1016/j.abb.2011.09.005.

(93) Srivastava, R.; Ratheesh, A.; Gude, R. K.; Rao, K. V. K.; Panda, D.; Subrahmanyam, G. Resveratrol Inhibits Type II Phosphatidylinositol 4-Kinase: A Key Component in Pathways of Phosphoinositide Turn Over. *Biochem Pharmacol* **2005**, *70* (7), 1048–1055. https://doi.org/10.1016/j.bcp.2005.07.003.

(94) Sah, J. F.; Balasubramanian, S.; Eckert, R. L.; Rorke, E. A. Epigallocatechin-3-Gallate Inhibits Epidermal Growth Factor Receptor Signaling Pathway. *J Biol Chem* **2004**, *279* (13), 12755–12762. https://doi.org/10.1074/jbc.M312333200.

(95) Pirola, L.; Fröjdö, S. Resveratrol: One Molecule, Many Targets. *IUBMB Life* **2008**, *60* (5), 323–332. https://doi.org/10.1002/iub.47.

(96) Whitman, M.; Kaplan, D.; Roberts, T.; Cantley, L. Evidence for Two Distinct Phosphatidylinositol Kinases in Fibroblasts. Implications for Cellular Regulation. *Biochem J* **1987**, *247* (1), 165–174. https://doi.org/10.1042/bj2470165.

(97) Sengupta, N.; Jović, M.; Barnaeva, E.; Kim, D. W.; Hu, X.; Southall, N.; Dejmek, M.; Mejdrova, I.; Nencka, R.; Baumlova, A.; Chalupska, D.; Boura, E.; Ferrer, M.; Marugan, J.; Balla, T. A Large Scale High-Throughput Screen Identifies Chemical Inhibitors of Phosphatidylinositol 4-Kinase Type II Alpha. *J Lipid Res* **2019**, *60* (3), 683–693. https://doi.org/10.1194/jlr.D090159.

(98) Li, J.; Gao, Z.; Zhao, D.; Zhang, L.; Qiao, X.; Zhao, Y.; Ding, H.; Zhang, P.; Lu, J.; Liu, J.; Jiang, H.; Luo, C.; Chen, C. PI-273, a Substrate-Competitive, Specific Small-Molecule Inhibitor of PI4KIIα, Inhibits the Growth of Breast Cancer Cells. *Cancer Res* **2017**, *77* (22), 6253–6266. https://doi.org/10.1158/0008-5472.CAN-17-0484.

(99) Bansal, R.; Malhotra, A. Therapeutic Progression of Quinazolines as Targeted Chemotherapeutic Agents. *Eur J Med Chem* **2021**, *211*, 113016. https://doi.org/10.1016/j.ejmech.2020.113016.

(100) Das, D.; Hong, J. Recent Advancements of 4-Aminoquinazoline Derivatives as Kinase Inhibitors and Their Applications in Medicinal Chemistry. *Eur J Med Chem* **2019**, *170*, 55–72. https://doi.org/10.1016/j.ejmech.2019.03.004.

(101) Connolly, D. J.; Cusack, D.; O'Sullivan, T. P.; Guiry, P. J. Synthesis of Quinazolinones and Quinazolines. *Tetrahedron* **2005**, *61* (43), 10153–10202. https://doi.org/10.1016/j.tet.2005.07.010.

(102) Rad-Moghadam, K.; Samavi, L. One-Pot Three-Component Synthesis of 2-Substituted 4-Aminoquinazolines. *J Heterocycl Chem* **2006**, *43* (4), 913–916. https://doi.org/10.1002/jhet.5570430415.

(103) Lacbay, C. M.; Mancuso, J.; Lin, Y.-S.; Bennett, N.; Götte, M.; Tsantrizos, Y. S. Modular Assembly of Purine-like Bisphosphonates as Inhibitors of HIV-1 Reverse Transcriptase. *J Med Chem* **2014**, *57* (17), 7435–7449. https://doi.org/10.1021/jm501010f.

(104) Sakamoto, T.; Ohsawa, K. Palladium-Catalyzed Cyanation of Aryl and Heteroaryl Iodides with Copper(I) Cyanide. *J Chem Soc Perkin 1* **1999**, No. 16, 2323–2326. https://doi.org/10.1039/a903345i.

(105) Martin, R.; Buchwald, S. L. Palladium-Catalyzed Suzuki−Miyaura Cross-Coupling Reactions Employing Dialkylbiaryl Phosphine Ligands. *Acc Chem Res* **2008**, *41* (11), 1461–1473. https://doi.org/10.1021/ar800036s.

(106) Tai, A. W.; Bojjireddy, N.; Balla, T. A Homogeneous and Nonisotopic Assay for Phosphatidylinositol 4-Kinases. *Anal Biochem* **2011**, *417* (1), 97–102. https://doi.org/10.1016/j.ab.2011.05.046.

(107) Zhang, D.; Lin, J.; Han, J. Receptor-Interacting Protein (RIP) Kinase Family. *Cell Mol Immunol* **2010**, *7* (4), 243–249. https://doi.org/10.1038/cmi.2010.10.

(108) Cuny, G. D.; Degterev, A. RIPK Protein Kinase Family: Atypical Lives of Typical Kinases. *Semin Cell Dev Biol.* **2021**, *109*, 96–105. https://doi.org/10.1016/j.semcdb.2020.06.014.

(109) Eng, V. V.; Wemyss, M. A.; Pearson, J. S. The Diverse Roles of RIP Kinases in Host-Pathogen Interactions. *Semin Cell Dev Biol* **2021**, *109*, 125–143. https://doi.org/10.1016/j.semcdb.2020.08.005.

(110) Declercq, W.; Vanden Berghe, T.; Vandenabeele, P. RIP Kinases at the Crossroads of Cell Death and Survival. *Cell* **2009**, *138* (2), 229–232. https://doi.org/10.1016/j.cell.2009.07.006.

(111) He, S.; Wang, X. RIP Kinases as Modulators of Inflammation and Immunity. *Nat Immunol* **2018**, *19* (9), 912–922. https://doi.org/10.1038/s41590-018-0188-x.

(112) Lv, S.; Jiang, Y.; Li, Y.; Huang, R.; Peng, L.; Ma, Z.; Lu, N.; Lin, X.; Yan, J. Comparative and Evolutionary Analysis of RIP Kinases in Immune Responses. *Front Genet* **2022**, *13*. https://doi.org/10.3389/fgene.2022.796291.

(113) Newton, K. RIPK1 and RIPK3: Critical Regulators of Inflammation and Cell Death. *Trends Cell Biol* **2015**, *25* (6), 347–353. https://doi.org/10.1016/j.tcb.2015.01.001.

(114) Yatim, N.; Jusforgues-Saklani, H.; Orozco, S.; Schulz, O.; Barreira da Silva, R.; Reis e Sousa, C.; Green, D. R.; Oberst, A.; Albert, M. L. RIPK1 and NF-KB Signaling in Dying Cells Determines Cross-Priming of CD8 $^+$ T Cells. *Science* **2015**, *350* (6258), 328–334. https://doi.org/10.1126/science.aad0395.

(115) Gong, Q.; Long, Z.; Zhong, F. L.; Teo, D. E. T.; Jin, Y.; Yin, Z.; Boo, Z. Z.; Zhang, Y.; Zhang, J.; Yang, R.; Bhushan, S.; Reversade, B.; Li, Z.; Wu, B. Structural Basis of RIP2 Activation and Signaling. *Nat Commun* **2018**, *9* (1), 4993. https://doi.org/10.1038/s41467-018-07447-9.

(116) Yang, Q.; Tian, S.; Liu, Z.; Dong, W. Knockdown of RIPK2 Inhibits Proliferation and Migration, and Induces Apoptosis via the NF-KB Signaling Pathway in Gastric Cancer. *Front Genet* **2021**, *12*. https://doi.org/10.3389/fgene.2021.627464.

(117) Moriwaki, K.; Chan, F. K.-M. Regulation of RIPK3- and RHIM-Dependent Necroptosis by the Proteasome. *J Biol Chem* **2016**, *291* (11), 5948–5959. https://doi.org/10.1074/jbc.M115.700997.

(118) Meylan, E.; Martinon, F.; Thome, M.; Gschwendt, M.; Tschopp, J. RIP4 (DIK/PKK), a Novel Member of the RIP Kinase Family, Activates NF-κB and Is Processed during Apoptosis. *EMBO Rep* **2002**, *3* (12), 1201–1208. https://doi.org/10.1093/embo-reports/kvf236.

(119) Zha, J.; Zhou, Q.; Xu, L.-G.; Chen, D.; Li, L.; Zhai, Z.; Shu, H.-B. RIP5 Is a RIP-Homologous Inducer of Cell Death. *Biochem Biophys Res Commun* **2004**, *319* (2), 298–303. https://doi.org/10.1016/j.bbrc.2004.04.194.

(120) Dzamko, N. L. LRRK2 and the Immune System. *Adv Neurobiol* **2017**, *14*, 123–143. https://doi.org/10.1007/978-3-319-49969-7_7.

(121) Honjo, H.; Watanabe, T.; Kamata, K.; Minaga, K.; Kudo, M. RIPK2 as a New Therapeutic Target in Inflammatory Bowel Diseases. *Front Pharmacol* **2021**, *12*, 650403. https://doi.org/10.3389/fphar.2021.650403.

(122) Lin, C.-C.; Mabe, N. W.; Lin, Y.-T.; Yang, W.-H.; Tang, X.; Hong, L.; Sun, T.; Force, J.; Marks, J. R.; Yao, T.-P.; Alvarez, J. V.; Chi, J.-T. RIPK3 Upregulation Confers Robust Proliferation and Collateral Cystine-Dependence on Breast Cancer Recurrence. *Cell Death Differ* **2020**, *27* (7), 2234–2247. https://doi.org/10.1038/s41418-020-0499-y.

(123) Fernández-García, V.; González-Ramos, S.; Martín-Sanz, P.; Portillo, F. G.; Laparra, J. M.; Boscá, L. NOD1 in the Interplay between Microbiota and Gastrointestinal Immune Adaptations. *Pharmacol Res* **2021**, *171*, 105775. https://doi.org/10.1016/j.phrs.2021.105775.

(124) Damgaard, R. B.; Nachbur, U.; Yabal, M.; Wong, W. W.-L.; Fiil, B. K.; Kastirr, M.; Rieser, E.; Rickard, J. A.; Bankovacki, A.; Peschel, C.; Ruland, J.; Bekker-Jensen, S.; Mailand, N.; Kaufmann, T.; Strasser, A.; Walczak, H.; Silke, J.; Jost, P. J.; Gyrd-Hansen, M. The Ubiquitin Ligase XIAP Recruits LUBAC for NOD2 Signaling in Inflammation and Innate Immunity. *Mol Cell* **2012**, *46* (6), 746–758. https://doi.org/10.1016/j.molcel.2012.04.014.

(125) Martínez-Torres, R. J.; Chamaillard, M. The Ubiquitin Code of NODs Signaling Pathways in Health and Disease. *Front Immunol* **2019**, *10*, 2648. https://doi.org/10.3389/fimmu.2019.02648.

(126) Heim, V. J.; Stafford, C. A.; Nachbur, U. NOD Signaling and Cell Death. *Front Cell Dev Biol* **2019**, *7*. https://doi.org/10.3389/fcell.2019.00208.

(127) Liu, S.; Joshi, K.; Denning, M. F.; Zhang, J. RIPK3 Signaling and Its Role in the Pathogenesis of Cancers. *Cell Mol Life Sci* **2021**, *78* (23), 7199–7217. https://doi.org/10.1007/s00018-021-03947-y.

(128) Ahn, D.; Prince, A. Participation of Necroptosis in the Host Response to Acute Bacterial Pneumonia. *J Innate Immun* **2017**, *9* (3), 262–270. https://doi.org/10.1159/000455100.

(129) Upton, J. W.; Shubina, M.; Balachandran, S. RIPK3-driven Cell Death during Virus Infections. *Immunol Rev* **2017**, *277* (1), 90–101. https://doi.org/10.1111/imr.12539.

(130) Zhang, H.; Wu, X.; Li, X.; Li, M.; Li, F.; Wang, L.; Zhang, X.; Zhang, Y.; Luo, Y.; Wang, H.; Jiang, Y.; Zhang, H. Crucial Roles of the RIP Homotypic Interaction Motifs of RIPK3 in RIPK1-Dependent Cell Death and Lymphoproliferative Disease. *Cell Rep* **2020**, *31* (7), 107650. https://doi.org/10.1016/j.celrep.2020.107650.

(131) Mompeán, M.; Li, W.; Li, J.; Laage, S.; Siemer, A. B.; Bozkurt, G.; Wu, H.; McDermott, A. E. The Structure of the Necrosome RIPK1-RIPK3 Core, a Human Hetero-Amyloid Signaling Complex. *Cell* **2018**, *173* (5), 1244–1253.e10. https://doi.org/10.1016/j.cell.2018.03.032.

(132) Dhuriya, Y. K.; Sharma, D. Necroptosis: A Regulated Inflammatory Mode of Cell Death. *J Neuroinflammation* **2018**, *15* (1), 199. https://doi.org/10.1186/s12974-018-1235-0.

(133) Orozco, S. L.; Daniels, B. P.; Yatim, N.; Messmer, M. N.; Quarato, G.; Chen-Harris, H.; Cullen, S. P.; Snyder, A. G.; Ralli-Jain, P.; Frase, S.; Tait, S. W. G.; Green, D. R.; Albert, M. L.; Oberst, A. RIPK3 Activation Leads to Cytokine Synthesis That Continues after Loss of Cell Membrane Integrity. *Cell Rep* **2019**, *28* (9), 2275–2287.e5. https://doi.org/10.1016/j.celrep.2019.07.077.

(134) Pham, A. T.; Ghilardi, A. F.; Sun, L. Recent Advances in the Development of RIPK2 Modulators for the Treatment of Inflammatory Diseases. *Front Pharmacol* **2023**, *14*, 1127722. https://doi.org/10.3389/fphar.2023.1127722.

(135) Martens, S.; Hofmans, S.; Declercq, W.; Augustyns, K.; Vandenabeele, P. Inhibitors Targeting RIPK1/RIPK3: Old and New Drugs. *Trends Pharmacol Sci* **2020**, *41* (3), 209–224. https://doi.org/10.1016/j.tips.2020.01.002.

(136) Tigno-Aranjuez, J. T.; Benderitter, P.; Rombouts, F.; Deroose, F.; Bai, X.; Mattioli, B.; Cominelli, F.; Pizarro, T. T.; Hoflack, J.; Abbott, D. W. In Vivo Inhibition of RIPK2 Kinase Alleviates Inflammatory Disease. *J Biol Chem* **2014**, *289* (43), 29651–29664. https://doi.org/10.1074/jbc.M114.591388.

(137) Nachbur, U.; Stafford, C. A.; Bankovacki, A.; Zhan, Y.; Lindqvist, L. M.; Fiil, B. K.; Khakham, Y.; Ko, H.-J.; Sandow, J. J.; Falk, H.; Holien, J. K.; Chau, D.; Hildebrand, J.; Vince, J. E.; Sharp, P. P.; Webb, A. I.; Jackman, K. A.; Mühlen, S.; Kennedy, C. L.; Lowes, K. N.; Murphy, J. M.; Gyrd-Hansen, M.; Parker, M. W.; Hartland, E. L.; Lew, A. M.; Huang, D. C. S.; Lessene, G.; Silke, J. A RIPK2 Inhibitor Delays NOD Signalling Events yet Prevents Inflammatory Cytokine Production. *Nat Commun* **2015**, *6* (1), 6442. https://doi.org/10.1038/ncomms7442.

(138) Haile, P. A.; Votta, B. J.; Marquis, R. W.; Bury, M. J.; Mehlmann, J. F.; Singhaus, R.; Charnley, A. K.; Lakdawala, A. S.; Convery, M. A.; Lipshutz, D. B.; Desai, B. M.; Swift, B.; Capriotti, C. A.; Berger, S. B.; Mahajan, M. K.; Reilly, M. A.; Rivera, E. J.; Sun, H. H.; Nagilla, R.; Beal, A. M.; Finger, J. N.; Cook, M. N.; King, B. W.; Ouellette, M. T.; Totoritis, R. D.; Pierdomenico, M.; Negroni, A.; Stronati, L.; Cucchiara, S.; Ziółkowski, B.; Vossenkämper, A.; MacDonald, T. T.; Gough, P. J.; Bertin, J.; Casillas, L. N. The

Identification and Pharmacological Characterization of 6-(*Tert*-Butylsulfonyl)-*N*-(5-Fluoro-1*H*-Indazol-3-Yl)Quinolin-4-Amine (GSK583), a Highly Potent and Selective Inhibitor of RIP2 Kinase. *J Med Chem* **2016**, *59* (10), 4867–4880. https://doi.org/10.1021/acs.jmedchem.6b00211.

(139) Haile, P. A.; Casillas, L. N.; Votta, B. J.; Wang, G. Z.; Charnley, A. K.; Dong, X.; Bury, M. J.; Romano, J. J.; Mehlmann, J. F.; King, B. W.; Erhard, K. F.; Hanning, C. R.; Lipshutz, D. B.; Desai, B. M.; Capriotti, C. A.; Schaeffer, M. C.; Berger, S. B.; Mahajan, M. K.; Reilly, M. A.; Nagilla, R.; Rivera, E. J.; Sun, H. H.; Kenna, J. K.; Beal, A. M.; Ouellette, M. T.; Kelly, M.; Stemp, G.; Convery, M. A.; Vossenkämper, A.; MacDonald, T. T.; Gough, P. J.; Bertin, J.; Marquis, R. W. Discovery of a First-in-Class Receptor Interacting Protein 2 (RIP2) Kinase Specific Clinical Candidate, 2-((4-(Benzo[*d*]Thiazol-5-Ylamino)-6-(*Tert* -Butylsulfonyl)Quinazolin-7-Yl)Oxy)Ethyl Dihydrogen Phosphate, for the Treatment of Inflammatory Diseases. *J Med Chem* **2019**, *62* (14), 6482–6494. https://doi.org/10.1021/acs.jmedchem.9b00575.

(140) Hrdinka, M.; Schlicher, L.; Dai, B.; Pinkas, D. M.; Bufton, J. C.; Picaud, S.; Ward, J. A.; Rogers, C.; Suebsuwong, C.; Nikhar, S.; Cuny, G. D.; Huber, K. V.; Filippakopoulos, P.; Bullock, A. N.; Degterev, A.; Gyrd-Hansen, M. Small Molecule Inhibitors Reveal an Indispensable Scaffolding Role of RIPK2 in NOD2 Signaling. *EMBO J* **2018**, *37* (17). https://doi.org/10.15252/embj.201899372.

(141) Suebsuwong, C.; Dai, B.; Pinkas, D. M.; Duddupudi, A. L.; Li, L.; Bufton, J. C.; Schlicher, L.; Gyrd-Hansen, M.; Hu, M.; Bullock, A. N.; Degterev, A.; Cuny, G. D. Receptor-Interacting Protein Kinase 2 (RIPK2) and Nucleotide-Binding Oligomerization Domain (NOD) Cell Signaling Inhibitors Based on a 3,5-Diphenyl-2-Aminopyridine Scaffold. *Eur J Med Chem* **2020**, *200*, 112417. https://doi.org/10.1016/j.ejmech.2020.112417.

(142) Yuan, X.; Chen, Y.; Tang, M.; Wei, Y.; Shi, M.; Yang, Y.; Zhou, Y.; Yang, T.; Liu, J.; Liu, K.; Deng, D.; Zhang, C.; Chen, L. Discovery of Potent and Selective Receptor-Interacting Serine/Threonine Protein Kinase 2 (RIPK2) Inhibitors for the Treatment of Inflammatory Bowel Diseases (IBDs). *J Med Chem* **2022**, *65* (13), 9312–9327. https://doi.org/10.1021/acs.jmedchem.2c00604.

(143) Wu, S.; Xu, L.; Wang, X.; Yang, Q.; Wang, J.; He, S.; Zhang, X. Design, Synthesis, and Structure-Activity Relationship of Novel RIPK2 Inhibitors. *Bioorg Med Chem Lett* **2022**, *75*, 128968. https://doi.org/10.1016/j.bmcl.2022.128968.

(144) Fan, T.; Ji, Y.; Chen, D.; Peng, X.; Ai, J.; Xiong, B. Design, Synthesis and Biological Evaluation of 4-Aminoquinoline Derivatives as Receptor-Interacting Protein Kinase 2

(RIPK2) Inhibitors. *J Enzyme Inhib Med Chem* **2023**, *38* (1), 282–293. https://doi.org/10.1080/14756366.2022.2148317.

(145) Kaiser, W. J.; Sridharan, H.; Huang, C.; Mandal, P.; Upton, J. W.; Gough, P. J.; Sehon, C. A.; Marquis, R. W.; Bertin, J.; Mocarski, E. S. Toll-like Receptor 3-Mediated Necrosis via TRIF, RIP3, and MLKL. *J Biol Chem* **2013**, *288* (43), 31268–31279. https://doi.org/10.1074/jbc.M113.462341.

(146) Mandal, P.; Berger, S. B.; Pillay, S.; Moriwaki, K.; Huang, C.; Guo, H.; Lich, J. D.; Finger, J.; Kasparcova, V.; Votta, B.; Ouellette, M.; King, B. W.; Wisnoski, D.; Lakdawala, A. S.; DeMartino, M. P.; Casillas, L. N.; Haile, P. A.; Sehon, C. A.; Marquis, R. W.; Upton, J.; Daley-Bauer, L. P.; Roback, L.; Ramia, N.; Dovey, C. M.; Carette, J. E.; Chan, F. K.-M.; Bertin, J.; Gough, P. J.; Mocarski, E. S.; Kaiser, W. J. RIP3 Induces Apoptosis Independent of Pronecrotic Kinase Activity. *Mol Cell* **2014**, *56* (4), 481–495. https://doi.org/10.1016/j.molcel.2014.10.021.

(147) Rodriguez, D. A.; Weinlich, R.; Brown, S.; Guy, C.; Fitzgerald, P.; Dillon, C. P.; Oberst, A.; Quarato, G.; Low, J.; Cripps, J. G.; Chen, T.; Green, D. R. Characterization of RIPK3-Mediated Phosphorylation of the Activation Loop of MLKL during Necroptosis. *Cell Death Differ* **2016**, *23* (1), 76–88. https://doi.org/10.1038/cdd.2015.70.

(148) Park, H.-H.; Park, S.-Y.; Mah, S.; Park, J.-H.; Hong, S.-S.; Hong, S.; Kim, Y.-S. HS-1371, a Novel Kinase Inhibitor of RIP3-Mediated Necroptosis. *Exp Mol Med* **2018**, *50* (9), 1–15. https://doi.org/10.1038/s12276-018-0152-8.

(149) Xia, K.; Zhu, F.; Yang, C.; Wu, S.; Lin, Y.; Ma, H.; Yu, X.; Zhao, C.; Ji, Y.; Ge, W.; Wang, J.; Du, Y.; Zhang, W.; Yang, T.; Zhang, X.; He, S. Discovery of a Potent RIPK3 Inhibitor for the Amelioration of Necroptosis-Associated Inflammatory Injury. *Front Cell Dev Biol* **2020**, *8*, 606119. https://doi.org/10.3389/fcell.2020.606119.

(150) Wu, S.; Xu, C.; Xia, K.; Lin, Y.; Tian, S.; Ma, H.; Ji, Y.; Zhu, F.; He, S.; Zhang, X. Ring Closure Strategy Leads to Potent RIPK3 Inhibitors. *Eur J Med Chem* **2021**, *217*, 113327. https://doi.org/10.1016/j.ejmech.2021.113327.

(151) Canning, P.; Ruan, Q.; Schwerd, T.; Hrdinka, M.; Maki, J. L.; Saleh, D.; Suebsuwong, C.; Ray, S.; Brennan, P. E.; Cuny, G. D.; Uhlig, H. H.; Gyrd-Hansen, M.; Degterev, A.; Bullock, A. N. Inflammatory Signaling by NOD-RIPK2 Is Inhibited by Clinically Relevant Type II Kinase Inhibitors. *Chem Biol* **2015**, *22* (9), 1174–1184. https://doi.org/10.1016/j.chembiol.2015.07.017.

(152) Zhou, T.; Wang, Q.; Phan, N.; Ren, J.; Yang, H.; Feldman, C. C.; Feltenberger, J. B.; Ye, Z.; Wildman, S. A.; Tang, W.; Liu, B. Identification of a Novel Class of RIP1/RIP3 Dual Inhibitors That Impede Cell Death and Inflammation in Mouse Abdominal Aortic Aneurysm Models. *Cell Death Dis* **2019**, *10* (3), 226. https://doi.org/10.1038/s41419-019-1468-6.

(153) Bullock, A. N.; Degterev, A. Targeting RIPK1,2,3 to Combat Inflammation. *Oncotarget* **2015**, *6* (33), 34057–34058. https://doi.org/10.18632/oncotarget.6106.

(154) Meng, Y.; Davies, K. A.; Fitzgibbon, C.; Young, S. N.; Garnish, S. E.; Horne, C. R.; Luo, C.; Garnier, J.-M.; Liang, L.-Y.; Cowan, A. D.; Samson, A. L.; Lessene, G.; Sandow, J. J.; Czabotar, P. E.; Murphy, J. M. Human RIPK3 Maintains MLKL in an Inactive Conformation Prior to Cell Death by Necroptosis. *Nat Commun* **2021**, *12* (1), 6783. https://doi.org/10.1038/s41467-021-27032-x.

(155) Wang, C.; Xu, S.; Peng, L.; Zhang, B.; Zhang, H.; Hu, Y.; Zheng, P.; Zhu, W. Design, Synthesis and Biological Evaluation of Novel 4-Anlinoquinazoline Derivatives as EGFR Inhibitors with the Potential to Inhibit the Gefitinib-Resistant Nonsmall Cell Lung Cancers. *J Enzyme Inhib Med Chem* **2019**, *34* (1), 203–217. https://doi.org/10.1080/14756366.2018.1518957.

(156) Tsou, H.-R.; Mamuya, N.; Johnson, B. D.; Reich, M. F.; Gruber, B. C.; Ye, F.; Nilakantan, R.; Shen, R.; Discafani, C.; DeBlanc, R.; Davis, R.; Koehn, F. E.; Greenberger, L. M.; Wang, Y.-F.; Wissner, A. 6-Substituted-4-(3-Bromophenylamino)Quinazolines as Putative Irreversible Inhibitors of the Epidermal Growth Factor Receptor (EGFR) and Human Epidermal Growth Factor Receptor (HER-2) Tyrosine Kinases with Enhanced Antitumor Activity. *J Med Chem* **2001**, *44* (17), 2719–2734. https://doi.org/10.1021/jm0005555.

(157) Yoon, D. S.; Han, Y.; Stark, T. M.; Haber, J. C.; Gregg, B. T.; Stankovich, S. B. Efficient Synthesis of 4-Aminoquinazoline and Thieno[3,2-*d*]Pyrimidin-4-Ylamine Derivatives by Microwave Irradiation. *Org Lett* **2004**, *6* (25), 4775–4778. https://doi.org/10.1021/ol047919y.

(158) Chandregowda, V.; Venkateswara Rao, G.; Chandrasekara Reddy, G. Convergent Approach for Commercial Synthesis of Gefitinib and Erlotinib. *Org Process Res Dev* **2007**, *11* (5), 813–816. https://doi.org/10.1021/op700054p.

(159) Krajczyk, A.; Boryski, J. Dimroth Rearrangement-Old but Not Outdated. *Curr Org Chem* **2017**, *21* (25), 2515–2529. https://doi.org/10.2174/1385272821666170427125720.

(160) Stille, J. K. The Palladium-Catalyzed Cross-Coupling Reactions of Organotin Reagents with Organic Electrophiles[New Synthetic Methods(58)]. *Angew Chem Int Ed Engl* **1986**, *25* (6), 508–524. https://doi.org/10.1002/anie.198605081.

(161) Logan, M. E.; Oinen, M. E. Dechlorination of Aryl Chlorides with Sodium Formate Using a Homogeneous Palladium Catalyst. *Organometallics* **2006**, *25* (4), 1052–1054. https://doi.org/10.1021/om0507732.

(162) Chirieleison, S. M.; Kertesy, S. B.; Abbott, D. W. Synthetic Biology Reveals the Uniqueness of the RIP Kinase Domain. *J Immunol* **2016**, *196* (10), 4291–4297. https://doi.org/10.4049/jimmunol.1502631.

(163) Uehara, A.; Fujimoto, Y.; Kawasaki, A.; Kusumoto, S.; Fukase, K.; Takada, H. *Meso* -Diaminopimelic Acid and *Meso* -Lanthionine, Amino Acids Specific to Bacterial Peptidoglycans, Activate Human Epithelial Cells through NOD1. *J Immunol* **2006**, *177* (3), 1796–1804. https://doi.org/10.4049/jimmunol.177.3.1796.

(164) Girardin, S. E.; Boneca, I. G.; Viala, J.; Chamaillard, M.; Labigne, A.; Thomas, G.; Philpott, D. J.; Sansonetti, P. J. Nod2 Is a General Sensor of Peptidoglycan through Muramyl Dipeptide (MDP) Detection. *J Biol Chem* **2003**, *278* (11), 8869–8872. https://doi.org/10.1074/jbc.C200651200.

(165) Kabsch, W. *XDS. Acta Crystallogr D Biol Crystallogr* **2010**, *66* (2), 125–132. https://doi.org/10.1107/S0907444909047337.

(166) Maestro. Schrödinger Release 2021–3. Maestro, Schrödinger, LLC New York, NY; **2021**.

(167) Trott, O.; Olson, A. J. AutoDock Vina: improving the speed and accuracy of docking with a new scoring function, efficient optimization, and multithreading. *J Comput Chem* **2010**, *31* (2), 455–461. https://doi.org/10.1002/jcc.21334.

(168) He, X.; Da Ros, S.; Nelson, J.; Zhu, X.; Jiang, T.; Okram, B.; Jiang, S.; Michellys, P. Y.; Iskandar, M.; Espinola, S.; Jia, Y.; Bursulaya, B.; Kreusch, A.; Gao, M. Y.; Spraggon, G.; Baaten, J.; Clemmer, L.; Meeusen, S.; Huang, D.; Hill, R.; Nguyen-Tran, V.; Fathman, J.; Liu, B.; Tuntland, T.; Gordon, P.; Hollenbeck, T.; Ng, K.; Shi, J.; Bordone, L.; Liu, H. Identification of Potent and Selective RIPK2 Inhibitors for the Treatment of Inflammatory Diseases. *ACS Med Chem Lett* **2017**, *8* (10), 1048–1053. https://doi.org/10.1021/acsmedchemlett.7b00258.